CARDIAC TISSUE DISCRIMINATION USING FIBER-OPTICS CONFOCAL MICROSCOPY

by

Chao Huang

A dissertation submitted to the faculty of
The University of Utah
in partial fulfillment of the requirements for the degree of

Doctor of Philosophy

Department of Bioengineering

The University of Utah

August 2015

Copyright © Chao Huang 2015

All Rights Reserved

The University of Utah Graduate School

STATEMENT OF DISSERTATION APPROVAL

The dissertation of **Chao Huang**

has been approved by the following supervisory committee members:

Robert Hitchcock	, Chair	**5/15/15** Date Approved
Frank Sachse	, Member	**5/15/15** Date Approved
Aditya Kaza	, Member	**5/15/15** Date Approved
Kenneth Spitzer	, Member	**5/15/15** Date Approved
Ross Whitaker	, Member	**5/15/15** Date Approved

and by **Patrick Tresco**, Chair/Dean of the Department/College/School of **Bioengineering**

and by David B. Kieda, Dean of The Graduate School.

ABSTRACT

This body of work aims at establishing an approach for intraoperative discrimination of cardiac tissue types based on fiber-optics confocal microscopy (FCM). An important application of this approach is in pediatric heart surgery. A major risk of these surgeries is surgically-induced trauma to the specialized tissue of the cardiac conduction system. Current clinical practice during pediatric heart surgery is to approximate the disposition of the conduction system and scrupulously avoid it. A method for real-time delineation of the conduction system during pediatric heart surgery is needed.

FCM allows for real-time imaging of cellular and sub-cellular features up to 100 micrometers below a specimen's surface. We hypothesized that an approach based on FCM and fluorescent extracellular dyes would allow for delineation of the conduction system. We investigated this approach in the living arrested heart of rodent. In addition, the approach was validated in fixed tissue preparations from rodent, hearts using immunohistochemistry, three-dimensional conventional confocal microscopy, and image processing. Furthermore, we investigated dye delivery and microdosing approaches for intraoperative FCM discrimination of cardiac tissue types motivated by concerns in regards to consumption and adverse reactions of the dyes used in clinical applications of FCM. Lastly, we assessed the performance of the human and automated

classification systems in identifying cardiac tissue types acquired using this novel approach.

We demonstrated that it was feasible to discriminate cardiac tissue types using FCM and extracellular dyes. In our investigation into dye delivery and microdosing approaches, we showed that the developed novel local dye delivery approach based on a foam agarose dye carrier is particularly suitable for FCM during pediatric heart surgery. Furthermore, both human and automated classification systems achieved similarly high sensitivity and specificity in discriminating cardiac tissue types including tissue of the conduction system.

We suggest that this work constitutes an important step in clinical translation of FCM for cardiac tissue discrimination. The imaging approach as well as the foam agarose carrier for microdosed delivery of dye and the automated methods for tissue classification have the potential to reduce the incidence of trauma to the conduction system during pediatric heart surgery.

TABLE OF CONTENTS

ABSTRACT iii

LIST OF FIGURES vii

LIST OF ABBREVIATIONS viii

ACKNOWLEDGMENTS ix

Chapters

1. INTRODUCTION 1

    1.1 What is CHD? 3
    1.2 Treatment of CHD 6
    1.3 Postoperative Complications 7
    1.4 CCS 8
    1.5 Conduction Disturbances Following Surgical Repair of CHD 11
    1.6 Permanent Pacemaker Implantation 20
    1.7 References 21

2. IDENTIFICATION OF NODAL TISSUE IN THE LIVING HEART USING RAPID SCANNING FIBER-OPTICS CONFOCAL MICROSCOPY AND EXTRACELLULAR FLUOROPHORES 27

    2.1 Methods 30
    2.2 Results 31
    2.3 Discussion 34
    2.4 Acknowledgments 35
    2.5 Sources of Funding 35
    2.6 Disclosures 35
    2.7 References 35

3. LOCAL DELIVERY OF FLUORESCENT DYE FOR FIBER-OPTICS CONFOCAL MICROSCOPY OF THE LIVING HEART 46

    3.1 Introduction 47
    3.2 Materials and Methods 48

3.3 Results 50
3.4 Discussion 53
3.5 Author Contributions 55
3.6 Acknowledgment 55
3.7 Supplementary Material 55
3.8 References 55

4. HIGH SENSITIVITY AND SPECIFICITY OF CARDIAC TISSUE DISCRIMINATION USING FIBER-OPTICS CONFOCAL MICROSCOPY 57

4.1 Introduction 57
4.2 Materials and Methods 59
4.3 Results 67
4.4 Discussion 70
4.5 References 73

5. SUMMARY AND PERSPECTIVES 85

LIST OF FIGURES

Figures

4.1 Three-dimensional confocal images of rodent tissue..... 75

4.2 Three-dimensional confocal images of neonatal ovine and human tissue . 76

4.3 Anatomical overview of the right atrium from fixed rodent heart..... 77

4.4 Fiber-optics confocal microscopy of the living heart 78

4.5 Receiver operating characteristic analysis of indexed image sets..... 79

LIST OF ABBREVIATIONS

CHD	CONGENITAL HEART DEFECTS
SAN	SINOATRIAL NODE
AVN	ATRIOVENTRICULAR NODE
FCM	FIBER-OPTICS CONFOCAL MICROSCOPY
VSD	VENTRICULAR SEPTAL DEFECT
TGA	TRANSPOSITION OF THE GREAT ARTERIES
CCS	CARDIAC CONDUCTION SYSTEM
AWM	ATRIAL WORKING MYOCARDIUM
AV	ATRIOVENTRICULAR
PAPVC	PARTIAL ANOMALOUS PULMONARY VENOUS CONNECTION
ECG	ELECTROCARDIOGRAM

ACKNOWLEDGMENTS

I would like to express deepest gratitude to my advisors Drs. Robert Hitchcock, Frank Sachse, and Aditya Kaza for their expert guidance and support throughout my study and research. If it wasn't for their understanding, wisdom, patience, enthusiasm, and encouragement, I would not be fulfilling my lifelong dream of getting a Ph.D. I thank my other committee members Drs. Spitzer and Whitaker for their helpful suggestions and comments throughout my research. Thank you to Ms. Mitchell and Mr. Tran for their invaluable assistance in our experiments. Thank you to the staff and faculty at the Cardiovascular Research and Training Institute. I am eternally grateful for the assistance and support you have provided. Thank you to all my friends and family for helping me survive the stress of the past five years and not letting me give up. Acknowledgments are also made to Dr. Vercauteren, Dr. Lacombe, and Mr. Tihansky at Mauna Kea Technologies and Dr. Miller, Mr. Erickson, Mrs. Dahl, and Dr. Albertine at the University of Utah. Financial support was provided by the National Heart Lung Blood Institute, Nora Eccles Harrison Foundation for Cardiovascular Research, and Utah Science Technology and Research Initiative.

CHAPTER 1

INTRODUCTION

Congenital heart defects (CHD) are the most common type of birth defect in the United States with an estimated 32,000 new cases in the U.S. per year and 1.5 million new cases worldwide.[1, 2] CHD can oftentimes be lethal if left untreated.[3, 4] The state-of-the art approach for repairing CHD is pediatric heart surgery. Several complications can occur as a result of these complex surgical interventions, in particular, injury to the electrical conduction pathways of the heart such as the sinoatrial and atrioventricular node. The primary therapeutic intervention in treating these complications is permanent artificial pacing using pacemakers.

The sinoatrial node (SAN), atrioventricular node (AVN), and other pathways of the cardiac conduction system are not usually grossly visible as these specialized tissues reside below the surface of the heart wall.[5] In order to avoid damaging the conduction system during pediatric heart surgery, surgeons rely on an empirical approach and guidelines developed from gross anatomical studies carried out on a small population of congenitally malformed hearts to approximate the disposition of the conduction system.[6] However, the distribution of the conduction system can vary individually and with the complexity of the

defect. A forward-looking clinical strategy is needed to prevent damage to the specialized tissue of the conduction system during surgery and preserve cardiac autonomic activity.

A recently introduced endomicroscopy system has emerged as a tool in assisting clinicians in diagnosis of diseases during endocoscopy. This imaging technology combines a confocal laser system with fiber-optic imaging microprobes and is capable of *in vivo* visualization of cellular and sub-cellular features. In addition, the fiber-optics confocal microscopy (FCM) allows for real-time, cross-sectional imaging within approximately 100 microns from the tissue surface. Current clinical applications of FCM include imaging of internal microstructure of tissues in gastrointestinal[7], respiratory[8, 9], and urinary tracts[10] following intravenous injection of a contrast agent.

The aims of this project were to explore the feasibility of clinical translation of FCM for intraoperative microscopic discrimination of cardiac tissue types, in particular, for pediatric heart surgery. In the case of pediatric heart surgery, real-time visualization of nodal tissue with FCM could potentially reduce the risk of injury to the specialized tissue of the conduction system. In this chapter, we will look in detail at the motivation for this project; of interest is incidence of congenital heart defects and prevalence of injury to the specialized tissue of the conduction system in surgical repair of these congenital heart defects. In addition, the author will examine the attributable factors associated with postoperative complications following pediatric heart surgery. In Chapter 2, we will look at experiments performed to show feasibility in identifying these

characteristic microstructural features using both 3D confocal as well as FCM in both fixed and isolated, perfused hearts from rodent. In Chapter 3, we will look at dye delivery approaches that facilitate the translation of FCM for cardiac tissue discrimination. In Chapter 4, the author will describe a study looking at the performance of human and automated discrimination of nodal and working myocardium tissue acquired with FCM. Finally, in Chapter 5, the author will summarize the results of this body of work and how the work has advanced the cardiovascular and imaging field.

1.1 What is CHD?

CHD, also known as congenital heart disease or congenital cardiovascular defects, is a category of heart disease in which the heart or major blood vessels abnormally forms within a fetus during its development in the uterus. The cause of congenital heart disease is unknown and continues to be investigated and researched. However, there are some factors associated with an increased chance of having CHD including genetic or chromosomal abnormalities such as Down syndrome and drug and alcohol abuse by the mother during pregnancy.[11]

1.1.1 Types

CHD are divided into two types: cyanotic (lack of oxygen resulting in a bluish tint to the skin, lips, and fingernails) and acyanotic. In addition, CHD are categorized as mild, moderate, or severe. The severity of CHD depends on the size and complexity of the defect, also referred to as lesion. Furthermore, the

amount of expertise for optimal management of a defect is proportional to its severity. For instance, a hole between the wall of the ventricles known as a ventricular septal defect (VSD) can be categorized as a mild CHD if the size of the lesion is small. In some cases, these mild cases can spontaneously resolve as the infant develops. On the other hand, CHD that results in severely ill infants and requires surgical treatment are categorized as severe. An example of a severe CHD is dextro-TGA. In a normal heart, the right side of the heart pumps oxygen-poor blood into the lungs through the pulmonary arteries while the left side pumps oxygen-rich blood to the rest of the body through the aorta. In dextro-TGA, the aorta and pulmonary artery are transposed, therefore creating two separate circulatory systems and only oxygen-poor blood is ever circulated to the body while oxygen-rich blood is isolated within the pulmonary circulation. Often, infants with dextro-TGA have other heart defects such as a ventricular septal defect (VSD), allowing for at least some oxygen-rich blood to be circulated to the rest of the body. Severe CHD includes all cyanotic lesions such as dextro-TGA, tetralogy of Fallot, single ventricle physiology, and some forms of levo-TGA. Also included are acyanotic types of CHD such as atrioventricular septal defect and sizeable septal defects.[12] Another example of a type of CHD that can vary in terms of severity is levo-TGA. Similar to dextro-TGA, the aorta and pulmonary arteries are transposed. However, in levo-TGA, the morphological left and right ventricles are also transposed. The double transposition of the greater arteries and the ventricles results in a “correction” towards normal cardio-pulmonary circulation. Oftentimes, levo-TGA is referred to as congenitally corrected TGA.

The need for treatment and severity is dependent on whether other types of heart defects accompany the levo-TGA, as well as the ability of the morphological right ventricle to adapt to the increased pressure.

Severe and moderate CHD may be diagnosed during pregnancy using a cardiac ultrasound. However, some CHD are not detected until after birth and can even go unnoticed until adulthood. With the advent of the cardiac ultrasound and pulse oximetry, the detection rates have increased.[3, 11]

1.1.2 Prevalence

In 2000, the prevalence of CHD was 11.89 per 1000 children, 4.09 per 1000 adults, and 5.78 per 1000 in the general population.[13] The prevalence of severe CHD was 1.45 per 1000 children and accounted for 12% of all CHD lesions in children. In addition, the most prevalent lesions among severe CHD were conotruncal anomalies (e.g., tetralogy of Fallot, TGA) and atrioventricular septal defect. In this same study, it was also reported that the prevalence of severe CHD increased 85% in adults and 22% in children from 1985 to 2000.

1.1.3 Mortality

CHD is the leading killer of infants with birth defects. In 2010, CHD-related deaths accounted for 26.6% of all infants who died of a birth defect.[11] However, improved diagnostic capacities, surgical techniques, and patient management have reduced mortality resulting from CHD. A study looking at death certificates filed in the U.S. from 1999 to 2006 reported an overall decline in mortality

resulting from CHD of 24.1%.[14] Among children 1-4 years and 5-17 years of age, mortality caused by CHD decreased 21.0% and 36.1%, respectively. However, infant (<1 year of age) and children (1-17 years) mortality accounted for 48.1% and 12.4%, respectively, of all mortality caused by CHD. This means almost 1 out of 3 deaths caused by CHD from 1999 to 2006 were among infants and children.

When we look at survival of infants with severe CHD, there have been some improvements. One-year survival for these infants has improved from 67.4% to 82.5% for birth eras of 1979-1993 and 1994-2005, respectively.[15] Furthermore, it was noted that the one-year survival was 97.1% for infants with nonsevere CHD born between 1979 and 2005.

A study by [16] estimated the number of infants born with mild, moderate, and severe CHD from 1940 to 2002 based on birth rates and incidence data. They expected about 1 million infants would be born with mild CHD and half that number each for moderate and severe CHD. They estimated that about 75 and 80% of infants born with mild or moderate CHD, respectively, would still be alive in 2002 if treated. If not treated, only 40% would be alive. In addition, only 6% of infants with severe CHD would still be alive in 2002 if not treated compared to 36% if treated.

1.2 Treatment of CHD

Depending on the severity, some defects may not need treatment (a small VSD which may close on its own) while others can be treated with medication.

On the other hand, some defects including severe CHD, if left untreated, may have catastrophic consequences.[3, 4] A state-of-the-art approach for treating CHD is pediatric heart surgery. An estimated 2.4 per 1000 infants born with CHD will require pediatric heart surgery in the first year of life.[11] The estimated number of pediatric heart surgeries performed annually in the U.S. is 20,000-30,000.[16, 17]

The type, complexity, invasiveness, and time of surgical repair are dependent on the CHD. For example, a large VSD that has not closed by age 1 requires open heart surgery in which the septal defect is closed with stitches or a patch. For surgical repair of dextro-TGA in which the aorta and pulmonary artery are connected to the wrong sides of the heart, open heart surgery with an arterial switch operation is performed in order to connect these arteries to their correct locations. This surgical repair is oftentimes performed shortly after birth. Hypothermic or normothermic cardiopulmonary bypass, as well as aortic cross-clamping in which the systemic circulation is separated from the outflow of the heart by clamping of the aorta, may be required depending on the type of surgical repair.

1.3 Postoperative Complications

There are dramatic changes in the hemodynamic and electrophysiologic substrate following surgical repair of CHD. Cellular injury from hypoxia and cardiopulmonary bypass, fibrosis at sites of suture lines, and patches and chamber enlargement from abnormal pressure and volume loads are potentially deleterious consequences of these changes.[18] In some cases, these changes

can lead to serious complications including valvular insufficiency, arrythmias, and pulmonary hypertension. In addition, infective endocarditis and thromboembolic events have been associated with surgical repair of CHD involving patches, valves, and conduits.[19]

A particularly serious postoperative complication of CHD and the focus of this project is the production of conduction disturbances following surgical repair. These disturbances are unequivocally linked to the cardiac conduction system (CCS) of the heart and are the direct result of either developmental abnormalities of the CCS or direct surgical trauma to the specialized tissue of the CCS. If left untreated, conduction disturbances can be lethal. A group of studies found a mortality of 28-100% associated with conduction disturbances if left untreated.[20] In the subsequent sections of this chapter, we will look into the mechanisms that underlie the conduction disturbances and the current therapeutic intervention for treating this particular postoperative complication associated with CHD. But first we must examine in detail the cardiac conduction system and its surgical anatomy in both the structurally normal and abnormal heart.

1.4 CCS

The CCS is a group of specialized cardiac muscle cells that propagate electrical impulses throughout the rest of the heart. The sequential stimulation of the cardiac muscle by way of impulses from the CCS is what allows blood to be efficiently pumped throughout the body. The specialized cells of the CCS that initiate and conduct the impulse consist of three major parts: (1) SAN; (2)

atrioventricular junctional area, including AVN and penetrating bundle of His; and (3) bundle branches and Purkinje fibers.

The initiation of the electrical impulse originates from the SAN. The SAN in the structurally normal heart is located in the upper anterior right atrium within the intercaval region at the junction of the superior vena cava and the right atrial appendage.[21-23] From there, the impulse spreads from the SAN through peripheral nodal cells to surrounding atrial muscle of the right and left atria. Note that there is an interatrial tract known as the Bachmann bundle that is the preferential pathway for propagation of the impulse to the left atria.[24] Within the right atria, there is some controversy as to the existence of isolated internodal tracts that would preferentially propagate the impulse from the SAN to the AVN.[5, 25] At present, the evidence does not support the presence of these tracts and instead, the impulse from the SAN has been suggested to spread through nonspecialized cardiac muscle cells of the right atrium, also known as atrial working myocardium (AWM), towards the AVN.[26-28] The spread of electrical impulse originating from the SAN and propagated through the atria via working myocardium and the Bachmann bundle produces atrial contraction.

During atrial contraction, the electrical impulse through the right AWM is funneled into two preferential routes: one through the interatrial septum and the other through the terminal crest. The two routes through the interatrial septum and the terminal crest connect up to what is known as the fast and slow pathway, respectively, into the AVN. As the names would suggest, the fast and slow pathways describe the fastest and slowest route for the electrical impulse to

propagate into the AVN. The fast pathway is from the interatrial septum through a zone of transitional atrial muscle cells into the compact region of the AVN.[29] In the case of the slow pathway, the route of electrical impulse into the AVN is from the terminal crest into an inferior extension of the AVN.[30]

The AVN as well as the transitional cell zone and inferior extension in the structurally normal heart is contained within the triangle of Koch. The triangle of Koch is bordered posteriorly by a ridge called the tendon of Todaro, anteriorly by the annulus of the tricuspid valve, with the base at the orifice of the coronary sinus and the apex corresponding to the central fibrous body.[22, 31-33] The compact portion of the AVN known as the compact node is located at the apex of the triangle. The electrical impulse enters into compact node of the AVN through the slow and fast pathways. The principle function of the AVN is to delay the electrical impulse and allow time for atrial contraction to completely fill the ventricles with blood. The compact node of the AVN becomes the penetrating bundle of His at the point where the conduction axis becomes insulated from the surrounding atrial myocardium by tissues of the central fibrous body. The penetrating bundle of His provides, in the normal heart, the only pathway for the electrical impulse that was previously delayed in the AVN to propagate into the ventricles. The penetrating bundle of His bifurcates at the crest of the ventricular septum into the left and right bundle branches. The left and right bundle branches rapidly carry the electrical impulse to the apical regions of the left and right ventricles, respectively. The bundle branches are enveloped in a connective tissue sheath that isolates them from the surrounding muscle. At the apex of the

heart, the electrical impulse is broadly conducted from the bundle branches into the ventricles through a vast network of Purkinje fibers residing within the sub-endocardial region of the ventricles. The electrical impulse is conducted in a sequential fashion through ventricular muscle cells and the sub-endocardial Purkinje fibers located at the apical region and progresses upwards to the basal region of the ventricles. The spread of the impulse from the apical to basal region allows for efficient ventricular contraction and ejection of blood from the ventricles into the lungs and throughout the body. In the next section, the author will describe how abnormal conduction can arise in the cardiac conduction system (CCS), in particular how these abnormalities can occur during surgical repair of CHD.

1.5 Conduction Disturbances Following Surgical Repair of CHD

Abnormal conduction of the CCS can be present at birth (congenital) or develop during a patient's life (acquired). The former case is known as congenital heart block and may be associated with neonatal lupus, in which maternal autoantibodies cross the placenta and injure the previously normal fetal heart.[34] In addition, congenital heart block can occur secondary to specific cardiac malformations including atrioventricular septal defect and levo-TGA. Specifically, the AVN in these malformations can be anatomically displaced outside of the triangle of Koch. This abnormal displacement results in a progressive decline in conduction of the CCS over the life of the patient if left untreated.[35, 36] When

diagnosed in utero and during the postnatal period, congenital heart block is associated with CHD in approximately one-third and one-half of all diagnoses, respectively.[37]

Abnormal conduction of the CCS can also be acquired following surgical repair of CHD. These acquired conduction disturbances are commonly associated with surgical trauma to the pathways of the CCS. Depending on the complexity of the CHD and repair, surgical manipulation in and around regions of the CCS may be necessary. In most cases, the CCS cannot by directly visualized with the naked eye as it resides below the surface of the heart.[5, 38] During surgical repair of CHD, surgeons approximate the location of the CCS based on the spatial relationship of the CCS to various anatomical landmarks. For example, the triangle Koch and its defining structures including the ostium of the coronary sinus, the anterior-septal leaflet of the tricuspid valve, and the tendon of todaro serves as the anatomical landmark to the AV. The defining landmarks to the SAN are the superior vena cava and the terminal sulcus, a groove that marks the junction between the right atrial appendage and the systemic venous component of the right atrium. The SAN, a crescent-shaped structure, is located within this groove usually to the right of the crest of the atrial appendage. The anatomical landmarks described can be used with a high degree of confidence to localize the CCS in the structurally normal heart. However, in congenitally malformed hearts, there can be a considerable amount of variation in relation to the course of the CCS.

VSDs are typically classified according to the location of the defect in 1 of 4 ventricular components: the inlet septum, trabecular septum, outlet/infundibular septum, or membraneous septum.[6] Depending on the type of VSD, the course of the bundle of His and its associated regions: the penetrating bundle, nonbranching bundle, and branching bundle, can all vary.[6, 39] The surgical anatomy of the bundle of His in the congenitally malformed heart is well described.[6, 39] In the contemporary era, surgeons should know with a high degree of confidence the proximity of the CCS in relationship to a VSD. However, surgical trauma to the CCS during closure of VSDs still occurs. In a retrospective study by [39] looking at 2079 VSD closures performed from 1976 to 2001, twelve cases of trauma to the CCS was reported. Of these twelve, the authors suggest that in more than half of these cases, damage could have been avoided "had full advantage been taken of the extant anatomical knowledge" and that the "course of the atrioventricular bundle had been respected." In comparison to VSDs, the extent of the anatomical knowledge in more complex CHDs including atrioventricular septal defect, levo-TGA, and single ventricle physiology is inadequate to precisely localize the CCS and to prevent surgical trauma to these tissue regions.[40, 41]

In regards to localization of the SAN, there are also challenges, mainly in regards to the extensive distribution of the SAN, which are just recently coming to light. It is well established from histology that the SAN is a crescent-shaped structure that rests at the junction of the superior vena cava and the right atrium. The "head" of the node extends toward the interatrial groove while the "tail"

extends towards the orifice of the inferior vena cava. There does seem to be some variance in terms of the SAN size. A study by [23] had measured the SAN to be about 10-20 mm in length with a thickness of up to 5 mm. A histological study by [42] reported a mean length of 13.5 mm (range 8-21.5 mm) and a thickness around 8.8 mm. Recently, a combined histological and immunohistochemical analysis of the adult human SAN reported a nodal length and thickness of 29.5 and 6.4 mm, respectively[43]. This latest study also brought to light a "paranodal area" in humans located close to the SAN. The paranodal area was composed of both nodal and atrial myocytes and exhibited a molecular architecture that was intermediate to the one found in SAN and atrial muscle. The paranodal area has been suggested but not confirmed to extend further towards the inferior vena cava than the SAN, which extends about a third of the distance between the superior and inferior caval veins. It is well documented in electrophysiologic studies that the leading pacemaker site can shift between the SAN and the SAN periphery. Leading pacemaker sites have been observed in humans not only near the superior vena cava but also at an inferior site in close proximity to the inferior vena cava.[44, 45] A study by [46] required the entire crista terminalis from the superior to the inferior vena cava to be ablated in order to stop sinus rhythm. Whether or not the paranodal area is capable of pacemaking is still under investigation. However, if pacemaker shift were to be observed between the SA and the paranodal area, it would go a long way in reconciling histological, immunohistochemical, and electrophysiologic findings about this extensive region. The latest findings suggest that the SAN is not just a small nodule at the

junction of the superior vena cava with the right atrium. In terms of localization of the SAN during surgical repair of CHD, the existing textbook picture of the SAN is not sufficient to prevent injury to this extensive structure.

The reliance on these imprecise techniques to localize the CSS, especially in complex malformations, has made surgical trauma to the CCS an underappreciated sequela following surgical repair of CHD. Of particular interest to this project is surgical trauma to the SAN and AVN, which is associated with sinus node dysfunction and postoperative atrioventricular (AV) block, respectively. In the following two sections, the author will detail how conduction disturbances can occur in these two regions of the CCS and their incidence.

1.5.1 Sinus Node Dysfunction

An important risk factor for developing surgically-induced sinus node dysfunction is the surgical technique used in CHD repair.[47-49] For instance, partial anomalous pulmonary venous connection (PAPVC) is a CHD in which one or more of the pulmonary veins fail to connect to the left atrium. Instead, the pulmonary veins end up connecting to the right atrium or superior vena cava. In most cases, the PAPVC is accompanied by an atrial septal defect. The conventional surgical technique for repair of a PAPVC involves redirecting the anomalous pulmonary vein into the left atrium through the defect by baffling these structures with a pericardial or synthetic patch. However, retraction and thickening of the patch material could result in pulmonary venous and superior vena cava obstruction.[50, 51]

An alternative technique was introduced by [52] in which instead of a pericardial or synthetic patch, a J- or U-shaped right atriotomy was performed to form a flap from the right atrial wall. The atrial wall flap was pulled down and sutured to the rim of the septal defect in such a way as to baffle the defect and anomalous pulmonary vein into the left atrium. The reported advantage of this technique over conventional methods was that the preserved atrial contractility from the flap allowed appropriate growth of systemic and pulmonary venous pathways thereby reducing obstructions. However, the use of the J- or U-shaped incision to form the atrial wall flap resulted in an increased incidence of injury to the sinus node, sinus node artery, or crista terminalis. A study by [47] showed that 50% of patients who underwent atrial wall flap technique for repair of PAPVC at the time of hospital discharge were identified with sinus node dysfunction, whereas none of the patients who underwent the more conventional repair via patch experienced sinus node dysfunction.

Recently, the Warden technique has come into favor in repair of PAPVC.[53, 54] This technique requires the division of the superior vena cava, anastomosis of the cephalic superior vena cava to the right atrial appendage, and isolation of the caudal superior vena cava for pulmonary venous drainage. This technique has shown to have a lower incidence of pulmonary venous and superior venous cava obstruction. In addition, the technique requires less manipulation of the right atrium and superior vena cava, thereby avoiding injury to the SAN and has been shown to reduce the incidence of sinus node dysfunction.[53-56]

In the contemporary era, a major risk factor for sinus node dysfunction is the surgical technique used for repair of a CHD. The techniques that have the highest incidence of sinus node dysfunction are those that do not scrupulously avoid manipulation in or around the SAN region.

1.5.2 Postoperative AV Block

Postoperative atrioventricular (AV) block is a recognized sequelae of surgical repair of CHD.[57] AV block is classified as first-, second-, or third-degree (complete) block. The degree of AV block is defined based on measurements of the heart's electrical activity using an electrocardiogram (ECG).[58] First-degree AV block is defined as prolongation of the PR interval on an ECG to more than 200 msec. Second- and third-degree AV block is characterized by partial or complete interruption, respectively, of the electrical impulse between the atria and the ventricles through the AVN. Second-degree AV block is presented electrocardiographically as some P waves that are not followed by a QRS complex. Advanced second-degree AV block refers to 2 or more consecutive P waves without a QRS complex. Third-degree AV block is defined as the absence of QRS complexes following every P wave.

AV block can occur during the immediate period following repair of CHD as a result of swelling or tissue edema around the AVN. If these conduction disturbance do occur, they usually resolve within the first week after surgery without any permanent damage to the conduction system. Guidelines by the American College of Cardiology/American Heart Association/Heart Rhythm

Society list "advanced second- or third-degree AV block that persists for at least 7 days and that is not expected to resolve after cardiac surgery" as a Class I indication for pacemaker implantation for patients with CHD.[59]

A prospective study by [60] observed that out of 2,698 CHD operations, 54 (2%) were complicated by immediate postoperative AV block. From a subset of 51 study patients with AV block, 32 (63%) were observed to have recovered AV conduction within the first month of surgery. Of the patients who showed recovery within the first month of surgery, 42%, 81%, and 97% of the patients regained AV conduction by postoperative day 2, 7, and 9, respectively.

A sizable percentage of patients who exhibited persistent postoperative AV block and in whom pacemakers were placed, showed a return of AV conduction at a later time. Spontaneous recovery of AV conduction has been seen in patients in which pacemakers were placed at median follow up of 5.5 years (0.10 - 20 years).[61] In the study by [60], permanent pacemakers were implanted in 31 (57%) of the 54 patients with immediate postoperative AV block. Of those 31 patients, 11 (39%) had late recovery of AV conduction. A study by [62] reported that out of 72 patients with persistent postoperative AV block who underwent pacemaker implantation, 7 (10%) patients showed recovery of AV conduction at a median of 41 days (18-113 days) after CHD repair.

Patients who have undergone surgical repair of CHD are at risk of developing late-onset or delayed postoperative AV bock. In these cases, no AV block or only transient AV block was exhibited prior to hospital discharge. In the study by [60], 3 (9%) of the 32 patients who recovered from transient AV block and

subsequently discharged were observed to have second-degree AV block on postoperative day 57, year 2, and month 7. The onset of this delayed postoperative AV block has been reported to occur between 2 days and 25 years postoperatively.[57, 63-65] One of the few risk factors shown to be associated with delayed postoperative AV block is transient AV block. A study by [66] observed 2 (15%) of 13 patients who recovered from transient AV block during the immediate postoperative period, having subsequently developed delayed postoperative AV block. In this same study, of the 892 patients with no previous cases of AV block, only 4 (0.4%) developed delayed postoperative AV block.

Based on the above findings, there are several considerations in determining the appropriate timing for permanent pacing therapy.[58] In the case that the AV block is persistent, nonintervention can be potentially fatal. In addition, cost-driven pressures to reduce hospital length of stay and the associated increase in hospital costs would favor early intervention. However, if the AV block turned out to be transient but a permanent pacemaker was implanted early in the postoperative period, the patient would have been subjected to unnecessary surgery as well as the lifelong complications and morbidity associated with pacing therapy. In the next section, we will explore further the complications and morbidity associated with permanent pacemaker implantations.

1.6 Permanent Pacemaker Implantation

Permanent pacemaker implantation is the primary therapeutic intervention for treating conduction disturbances including sinus node dysfunction and postoperative AV block.[59] Permanent pacemaker therapy is associated with device-related complications including issues with the system generator, lead body, or lead electrode. A study involving 497 patients over a 22-year period showed that lead failure occurred in 155 leads (15%) and 115 patients (23%) with a higher incidence of lead failures in pediatric patients.[67]

In addition, permanent pacemaker therapy is associated with patient-related complications including pneumothorax, pericardial effusion/tamponade, hematoma, endocarditis/epericarditis, surgical wound infection, and death.[68] Pacemaker-related infections including superficial cellulitis, deep pocket infection, and endocarditis are serious and life-threatening complications associated with pacemaker implantation in the pediatric population. In a pediatric retrospective study, the overall incidence of pacemaker-related infection was 7.8%.[69]

Evidence is now emerging that long-term pacing may also be detrimental to ventricular function.[70] The conventional site for endocardial pacing in children has been at the right ventricular apex. Recent studies have shown that pacing from this site may induce left ventricular dyssynchrony.[71, 72]

1.7 References

1. Moller JH, Patton C, Varco RL, Lillehei CW. Late results (30 to 35 years) after operative closure of isolated ventricular septal defect from 1954 to 1960. *Am J Cardiol.* 1991;68:1491-7.

2. Hoffman JI. Congenital heart disease: incidence and inheritance. *Pediatr Clin North Am.* 1990;37:25-43.

3. Botto LD, Correa A, Erickson JD. Racial and temporal variations in the prevalence of heart defects. *Pediatrics.* 2001;107:E32.

4. Bonnet D, Coltri A, Butera G, Fermont L, Le Bidois J, Kachaner J, et al. Detection of transposition of the great arteries in fetuses reduces neonatal morbidity and mortality. *Circulation.* 1999;99:916-8.

5. Anderson RH, Ho SY, Becker AE. The surgical anatomy of the conduction tissues. *Thorax.* 1983;38:408-20.

6. Aiello VD. Understanding the morphology of the specialized conduction tissues in congenitally malformed hearts. *World J Pediatr Congenit Heart Surg*. 2015;6:239-49.

7. Sharma P, Meining AR, Coron E, Lightdale CJ, Wolfsen HC, Bansal A, et al. Real-time increased detection of neoplastic tissue in Barrett's esophagus with probe-based confocal laser endomicroscopy: final results of an international multicenter, prospective, randomized, controlled trial. *Gastrointest Endosc.* 2011;74:465-72.

8. Salaun M, Roussel F, Bourg-Heckly G, Vever-Bizet C, Dominique S, Genevois A, et al. In vivo probe-based confocal laser endomicroscopy in amiodarone-related pneumonia. *Eur Respir J.* 2013;42:1646-58.

9. Thiberville L, Salaun M, Lachkar S, Dominique S, Moreno-Swirc S, Vever-Bizet C, et al. Human in vivo fluorescence microimaging of the alveolar ducts and sacs during bronchoscopy. *Eur Respir J.* 2009;33:974-85.

10. Wu K, Liu JJ, Adams W, Sonn GA, Mach KE, Pan Y, et al. Dynamic real-time microscopy of the urinary tract using confocal laser endomicroscopy. *Urology.* 2011;78:225-31.

11. Go AS, Mozaffarian D, Roger VL, Benjamin EJ, Berry JD, Blaha MJ, et al. Heart disease and stroke statistics--2014 update: a report from the American Heart Association. *Circulation.* 2014;129:e28-e292.

12. Hoffman JI, Kaplan S. The incidence of congenital heart disease. *J Am Coll Cardiol.* 2002;39:1890-900.

13. Marelli AJ, Mackie AS, Ionescu-Ittu R, Rahme E, Pilote L. Congenital heart disease in the general population: changing prevalence and age distribution. *Circulation.* 2007;115:163-72.

14. Gilboa SM, Salemi JL, Nembhard WN, Fixler DE, Correa A. Mortality resulting from congenital heart disease among children and adults in the United States, 1999 to 2006. *Circulation.* 2010;122:2254-63.

15. Oster ME, Lee KA, Honein MA, Riehle-Colarusso T, Shin M, Correa A. Temporal trends in survival among infants with critical congenital heart defects. *Pediatrics.* 2013;131:e1502-8.

16. Hoffman JI, Kaplan S, Liberthson RR. Prevalence of congenital heart disease. *Am Heart J.* 2004;147:425-39.

17. Moodie DS. Adult congenital heart disease. *Curr Opin Cardiol.* 1994;9:137-42.

18. Walsh EP. Interventional electrophysiology in patients with congenital heart disease. *Circulation.* 2007;115:3224-34.

19. Perloff JK, Warnes CA. Challenges posed by adults with repaired congenital heart disease. *Circulation.* 2001;103:2637-43.

20. Gross GJ, Chiu CC, Hamilton RM, Kirsh JA, Stephenson EA. Natural history of postoperative heart block in congenital heart disease: implications for pacing intervention. *Heart Rhythm.* 2006;3:601-4.

21. Keith A, Flack M. The Form and Nature of the Muscular Connections between the Primary Divisions of the Vertebrate Heart. *J Anat Physiol.* 1907;41:172-89.

22. Cabrera JA, Sanchez-Quintana D. Cardiac anatomy: what the electrophysiologist needs to know. *Heart.* 2013;99:417-31.

23. Waller BF, Gering LE, Branyas NA, Slack JD. Anatomy, histology, and pathology of the cardiac conduction system: Part I. *Clin Cardiol.* 1993;16:249-52.

24. Bachmann G. The inter-auricular time interval. *Am J Physiol.* 1916;41:309-20.

25. Sherf L, James TN. Fine structure of cells and their histologic organization within internodal pathways of the heart: clinical and electrocardiographic implications. *Am J Cardiol.* 1979;44:345-69.

26. Ayettey AS, Navaratnam V, Yates RD. Ultrastructure of the internodal myocardium in the rat. *J Anat.* 1988;158:77-90.

27. Spach MS, Dolber PC, Sommer JR. Discontinuous propagation: an hypothesis based on known cardiac structural complexities. *Int J Cardiol.* 1985;7:167-74.

28. Anderson RH, Ho SY, Smith A, Becker AE. The internodal atrial myocardium. *Anat Rec.* 1981;201:75-82.

29. Li J, Greener ID, Inada S, Nikolski VP, Yamamoto M, Hancox JC, et al. Computer three-dimensional reconstruction of the atrioventricular node. *Circ Res.* 2008;102:975-85.

30. Inoue S, Becker AE. Posterior extensions of the human compact atrioventricular node: a neglected anatomic feature of potential clinical significance. *Circulation.* 1998;97:188-93.

31. Tawara S. *Das Reizleitungssystem des Saeugetierherzens*. Jena: Fischer; 1906.

32. Temple IP, Inada S, Dobrzynski H, Boyett MR. Connexins and the atrioventricular node. *Heart Rhythm.* 2013;10:297-304.

33. Dobrzynski H, Anderson RH, Atkinson A, Borbas Z, D'Souza A, Fraser JF, et al. Structure, function and clinical relevance of the cardiac conduction system, including the atrioventricular ring and outflow tract tissues. *Pharmacol Ther.* 2013;139:260-88.

34. Friedman D, Duncanson L, Glickstein J, Buyon J. A review of congenital heart block. *Images Paediatr Cardiol*. 2003;5:36-48.

35. Huhta JC, Maloney JD, Ritter DG, Ilstrup DM, Feldt RH. Complete atrioventricular block in patients with atrioventricular discordance. *Circulation.* 1983;67:1374-7.

36. Connelly MS, Liu PP, Williams WG, Webb GD, Robertson P, McLaughlin PR. Congenitally corrected transposition of the great arteries in the adult: functional status and complications. *J Am Coll Cardiol.* 1996;27:1238-43.

37. Kertesz NJ, Fenrich AL, Friedman RA. Congenital complete atrioventricular block. *Tex Heart Inst J.* 1997;24:301-7.

38. Chiu IS, Hung CR, How SW, Chen MR. Is the sinus node visible grossly? A histological study of normal hearts. *Int J Cardiol.* 1989;22:83-7.

39. Andersen HO, de Leval MR, Tsang VT, Elliott MJ, Anderson RH, Cook AC. Is complete heart block after surgical closure of ventricular septum defects still an issue? *Ann Thorac Surg.* 2006;82:948-56.

40. Fischbach PS, Frias PA, Strieper MJ, Campbell RM. Natural history and current therapy for complete heart block in children and patients with congenital heart disease. *Congenit Heart Dis.* 2007;2:224-34.

41. Dick M, 2nd, Norwood WI, Chipman C, Castaneda AR. Intraoperative recording of specialized atrioventricular conduction tissue electrograms in 47 patients. *Circulation.* 1979;59:150-60.

42. Sanchez-Quintana D, Cabrera JA, Farre J, Climent V, Anderson RH, Ho SY. Sinus node revisited in the era of electroanatomical mapping and catheter ablation. *Heart.* 2005;91:189-94.

43. Chandler N, Aslanidi O, Buckley D, Inada S, Birchall S, Atkinson A, et al. Computer Three-Dimensional Anatomical Reconstruction of the Human Sinus Node and a Novel Paranodal Area. *Anat Rec (Hoboken).* 2011:n/a-n/a.

44. Boyett MR, Honjo H, Kodama I. The sinoatrial node, a heterogeneous pacemaker structure. *Cardiovasc Res.* 2000;47:658-87.

45. Monfredi O, Dobrzynski H, Mondal T, Boyett MR, Morris GM. The Anatomy and Physiology of the Sinoatrial Node—A Contemporary Review. *Pacing Clin Electrophysiol.* 2010;33:1392-406.

46. Kalman JM, Lee RJ, Fisher WG, Chin MC, Ursell P, Stillson CA, et al. Radiofrequency catheter modification of sinus pacemaker function guided by intracardiac echocardiography. *Circulation.* 1995;92:3070-81.

47. Takahashi H, Oshima Y, Yoshida M, Yamaguchi M, Okada K, Okita Y. Sinus node dysfunction after repair of partial anomalous pulmonary venous connection. *J Thorac Cardiovasc Surg.* 2008;136:329-34.

48. Bae EJ, Lee JY, Noh CI, Kim WH, Kim YJ. Sinus node dysfunction after Fontan modifications--influence of surgical method. *Int J Cardiol.* 2003;88:285-91.

49. Manning PB, Mayer JE, Jr., Wernovsky G, Fishberger SB, Walsh EP. Staged operation to Fontan increases the incidence of sinoatrial node dysfunction. *J Thorac Cardiovasc Surg.* 1996;111:833-9; discussion 9-40.

50. Whight CM, Barratt-Boyes BG, Calder AL, Neutze JM, Brandt PW. Total anomalous pulmonary venous connection. Long-term results following repair in infancy. *J Thorac Cardiovasc Surg.* 1978;75:52-63.

51. Friedli B, Guerin R, Davignon A, Fouron JC, Stanley P. Surgical treatment of partial anomalous pulmonary venous drainage. A long-term follow-up study. *Circulation.* 1972;45:159-70.

52. Vargas FJ, Kreutzer GO. A surgical technique for correction of total anomalous pulmonary venous drainage. *J Thorac Cardiovasc Surg.* 1985;90:410-3.

53. Shahriari A, Rodefeld MD, Turrentine MW, Brown JW. Caval division technique for sinus venosus atrial septal defect with partial anomalous pulmonary venous connection. *Ann Thorac Surg.* 2006;81:224-9; discussion 9-30.

54. Kottayil BP, Dharan BS, Menon S, Bijulal S, Neema PK, Gopalakrishnan SK, et al. Anomalous pulmonary venous connection to superior vena cava: Warden technique. *Eur J Cardiothorac Surg.* 2011;39:388-91.

55. DiBardino DJ, McKenzie ED, Heinle JS, Su JT, Fraser CD, Jr. The Warden procedure for partially anomalous pulmonary venous connection to the superior caval vein. *Cardiol Young.* 2004;14:64-7.

56. Okumura S, Yamagishi M, Kanki Y, Ikeda N. Intraatrial rerouting by atrial flaps for partial anomalous pulmonary venous return. *Ann Thorac Surg.* 2003;76:1726-8.

57. Lillehei CW, Sellers RD, Bonnabeau RC, Eliot RS. Chronic Postsurgical Complete Heart Block. With Particular Reference to Prognosis, Management, and a New P-Wave Pacemaker. *J Thorac Cardiovasc Surg.* 1963;46:436-56.

58. Floris EAUtC, Narayanswami S. *Pacing Therapy in Infants and Children with Congenital and Acquired Complete Atrioventricular Block: Optimal Pacing Strategies, Management, and Follow-up*. INTECH Open Access Publisher; 2011.

59. Epstein AE, DiMarco JP, Ellenbogen KA, Estes NA, 3rd, Freedman RA, Gettes LS, et al. ACC/AHA/HRS 2008 Guidelines for Device-Based Therapy of Cardiac Rhythm Abnormalities: a report of the American College of Cardiology/American Heart Association Task Force on Practice Guidelines (Writing Committee to Revise the ACC/AHA/NASPE 2002 Guideline Update for Implantation of Cardiac Pacemakers and Antiarrhythmia Devices): developed in collaboration with the American Association for Thoracic Surgery and Society of Thoracic Surgeons. *Circulation.* 2008;117:e350-408.

60. Weindling SN, Saul JP, Gamble WJ, MayerJr JE, Wessel D, Walsh EP. Duration of complete atrioventricular block after congenital heart disease surgery. *Am J Cardiol.* 1998;82:525-7.

61. Bruckheimer E, Berul CI, Kopf GS, Hill SL, Warner KA, Kleinman CS, et al. Late recovery of surgically-induced atrioventricular block in patients with congenital heart disease. *J Interv Card Electrophysiol.* 2002;6:191-5.

62. Batra AS, Wells WJ, Hinoki KW, Stanton RA, Silka MJ. Late recovery of atrioventricular conduction after pacemaker implantation for complete heart block associated with surgery for congenital heart disease. *J Thorac Cardiovasc Surg.* 2003;125:1291-3.

63. Goldman BS, Williams WG, Hill T, Hesslein PS, McLaughlin PR, Trusler GA, et al. Permanent cardiac pacing after open heart surgery: congenital heart disease. *Pacing Clin Electrophysiol.* 1985;8:732-9.

64. Liberman L, Pass RH, Hordof AJ, Spotnitz HM. Late onset of heart block after open heart surgery for congenital heart disease. *Pediatr Cardiol.* 2008;29:56-9.

65. Siehr SL, Hanley FL, Reddy VM, Miyake CY, Dubin AM. Incidence and risk factors of complete atrioventricular block after operative ventricular septal defect repair. *Congenit Heart Dis.* 2014;9:211-5.

66. Lin A, Mahle WT, Frias PA, Fischbach PS, Kogon BE, Kanter KR, et al. Early and delayed atrioventricular conduction block after routine surgery for congenital heart disease. *J Thorac Cardiovasc Surg.* 2010;140:158-60.

67. Fortescue EB, Berul CI, Cecchin F, Walsh EP, Triedman JK, Alexander ME. Patient, procedural, and hardware factors associated with pacemaker lead failures in pediatrics and congenital heart disease. *Heart Rhythm.* 2004;1:150-9.

68. Czosek RJ, Meganathan K, Anderson JB, Knilans TK, Marino BS, Heaton PC. Cardiac rhythm devices in the pediatric population: utilization and complications. *Heart Rhythm.* 2012;9:199-208.

69. Cohen MI, Bush DM, Gaynor JW, Vetter VL, Tanel RE, Rhodes LA. Pediatric pacemaker infections: twenty years of experience. *J Thorac Cardiovasc Surg.* 2002;124:821-7.

70. Tantengco MV, Thomas RL, Karpawich PP. Left ventricular dysfunction after long-term right ventricular apical pacing in the young. *J Am Coll Cardiol.* 2001;37:2093-100.

71. Thambo JB, Bordachar P, Garrigue S, Lafitte S, Sanders P, Reuter S, et al. Detrimental ventricular remodeling in patients with congenital complete heart block and chronic right ventricular apical pacing. *Circulation.* 2004;110:3766-72.

72. Tops LF, Schalij MJ, Holman ER, van Erven L, van der Wall EE, Bax JJ. Right ventricular pacing can induce ventricular dyssynchrony in patients with atrial fibrillation after atrioventricular node ablation. *J Am Coll Cardiol.* 2006;48:1642-8.

CHAPTER 2

IDENTIFICATION OF NODAL TISSUE IN THE LIVING HEART USING RAPID SCANNING FIBER-OPTICS CONFOCAL MICROSCOPY AND EXTRACELLULAR FLUOROPHORES

Huang C, Kaza AK, Hitchcock RW, Sachse FB. Identification of nodal tissue in the living heart using rapid scanning fiber-optics confocal microscopy and extracellular fluorophores. *Circ Cardiovasc Imaging.* 2013;6:739-46. Reprinted with permission from Wolters Kluwer Health Lippincott Williams & Wilkins©. No modifications will be permitted.

Circulation
Cardiovascular Imaging

American Heart Association.

Identification of Nodal Tissue in the Living Heart Using Rapid Scanning Fiber-Optics Confocal Microscopy and Extracellular Fluorophores

Chao Huang, Aditya K. Kaza, Robert W. Hitchcock and Frank B. Sachse

Circ Cardiovasc Imaging. 2013;6:739-746; originally published online June 27, 2013;
doi: 10.1161/CIRCIMAGING.112.000121
Circulation: Cardiovascular Imaging is published by the American Heart Association, 7272 Greenville Avenue, Dallas, TX 75231
Copyright © 2013 American Heart Association, Inc. All rights reserved.
Print ISSN: 1941-9651. Online ISSN: 1942-0080

The online version of this article, along with updated information and services, is located on the World Wide Web at:
http://circimaging.ahajournals.org/content/6/5/739

Data Supplement (unedited) at:
http://circimaging.ahajournals.org/content/suppl/2013/06/27/CIRCIMAGING.112.000121.DC1.html

Permissions: Requests for permissions to reproduce figures, tables, or portions of articles originally published in *Circulation: Cardiovascular Imaging* can be obtained via RightsLink, a service of the Copyright Clearance Center, not the Editorial Office. Once the online version of the published article for which permission is being requested is located, click Request Permissions in the middle column of the Web page under Services. Further information about this process is available in the Permissions and Rights Question and Answer document.

Reprints: Information about reprints can be found online at:
http://www.lww.com/reprints

Subscriptions: Information about subscribing to *Circulation: Cardiovascular Imaging* is online at:
http://circimaging.ahajournals.org//subscriptions/

Original Article

Identification of Nodal Tissue in the Living Heart Using Rapid Scanning Fiber-Optics Confocal Microscopy and Extracellular Fluorophores

Chao Huang, BS; Aditya K. Kaza, MD; Robert W. Hitchcock, PhD; Frank B. Sachse, PhD

Background—Risks associated with pediatric reconstructive heart surgery include injury of the sinoatrial node (SAN) and atrioventricular node (AVN), requiring cardiac rhythm management using implantable pacemakers. These injuries are the result of difficulties in identifying nodal tissues intraoperatively. Here we describe an approach based on confocal microscopy and extracellular fluorophores to quantify tissue microstructure and identify nodal tissue.

Methods and Results—Using conventional 3-dimensional confocal microscopy we investigated the microstructural arrangement of SAN, AVN, and atrial working myocardium (AWM) in fixed rat heart. AWM exhibited a regular striated arrangement of the extracellular space. In contrast, SAN and AVN had an irregular, reticulated arrangement. AWM, SAN, and AVN tissues were beneath a thin surface layer of tissue that did not obstruct confocal microscopic imaging. Subsequently, we imaged tissues in living rat hearts with real-time fiber-optics confocal microscopy. Fiber-optics confocal microscopy images resembled images acquired with conventional confocal microscopy. We investigated spatial regularity of tissue microstructure from Fourier analysis and second-order image moments. Fourier analysis of fiber-optics confocal microscopy images showed that the spatial regularity of AWM was greater than that of nodal tissues (37.5±5.0% versus 24.3±3.9% for SAN and 23.8±3.7% for AVN; $P<0.05$). Similar differences of spatial regularities were revealed from second-order image moments (50.0±7.3% for AWM versus 29.3±6.7% for SAN and 27.3±5.5% for AVN; $P<0.05$).

Conclusions—The study demonstrates feasibility of identifying nodal tissue in living heart using extracellular fluorophores and fiber-optics confocal microscopy. Application of the approach in pediatric reconstructive heart surgery may reduce risks of injuring nodal tissues. **(*Circ Cardiovasc Imaging*. 2013;6:739-746.)**

Key Words: atrioventricular node ■ confocal imaging ■ congenital cardiac defect ■ sinoatrial node ■ 2-dimensional

Of all birth defects, congenital heart defects are the most frequent cause of death among infants in the US.[1] The state-of-the-art approach to repair congenital heart defects is open heart reconstructive surgery in the neonatal period. Complications that can occur as a result of these complex surgeries are sinus node dysfunction or atrioventricular block arising from trauma to the sinoatrial node (SAN) and atrioventricular node (AVN), respectively. These complications are associated with significant morbidity and mortality.[2] Patients with persistent complications require short-term or chronic cardiac rhythm management using implantable pacemakers. The need for permanent pacemakers after repair for congenital cardiac defects ranges from 1% to 3% for ventricular septal defect to as high as 27% to 45% for congenitally corrected transposition of the great arteries.[3–6]

Clinical Perspective on p 746

The SAN, AVN, and other tissues of the conduction pathways are not visible using surgical loupes or microscopes. These instruments are based on reflection of light from the tissue surface and do not provide visual information from within the tissue, where nodal tissue resides. The localization of SAN and AVN tissue during surgery is based on their relative proximity to anatomic landmarks. The SAN is usually located proximal to the crista terminalis in the right atrium. The AVN is adjacent to the atrioventricular septum of the heart. Commonly, the AVN is identified from the triangle of Koch, which is defined as the space between the septal leaflet of the tricuspid valve, coronary sinus, and the tendon of Todaro. In hearts with congenital defects this localization is made more difficult by individual variations in the spatial relationship of landmarks to nodal structures.[7,8] The aforementioned postoperative complications can arise as a result of this imprecise methodology for localization of nodal tissue. Thus, imaging

Received December 21, 2012; accepted June 12, 2013.

From the Department of Bioengineering (C.H., R.W.H., F.B.S.) and Nora Eccles Harrison Cardiovascular Research and Training Institute (F.B.S.), University of Utah, Salt Lake City, Utah; and Division of Pediatric Cardiothoracic Surgery, Department of Surgery, University of Utah School of Medicine, Salt Lake City, Utah (A.K.K.).

The online-only Data Supplement is available at http://circimaging.ahajournals.org/lookup/suppl/doi:10.1161/CIRCIMAGING.112.000121/-/DC1.

Correspondence to Frank B. Sachse, PhD, Department of Bioengineering, Nora Eccles Harrison Cardiovascular Research and Training Institute, University of Utah, 95 S 2000 E, Salt Lake City, UT 84112. E-mail fs@cvrti.utah.edu

© 2013 American Heart Association, Inc.

DOI: 10.1161/CIRCIMAGING.112.000121

approaches for real-time visualization of nodal tissue in the intraoperative setting could reduce the incidence of nodal dysfunction and conduction block.

In this study, we establish a novel intraoperative imaging modality to discriminate cardiac tissue types using methodology based on fluorescent labeling, confocal microscopy, and image analysis. To achieve this aim, we investigated the microstructure of atrial working myocardium (AWM), the SAN, and the AVN in a rodent model. Using fluorescent markers for nodal cells and extracellular space and 3-dimensional (3D) conventional confocal microscopy, we created reconstructions at submicrometer resolution from fixed tissue. From these reconstructions we developed methods for characterization of tissue microstructure based on texture analysis. Subsequently, we evaluated our approach for tissue discrimination in the isolated perfused heart using a recently introduced fiber-optics confocal microscopy (FCM) system, a fluorescent marker of the extracellular space, and specialized imaging microprobes. Using the acquired image data, we characterized the tissue microstructure with previously developed methods for texture analysis. We performed statistical analyses of conventional confocal microscopy and FCM image data to investigate the proposed approach for discrimination of cardiac tissue types. Furthermore, we explored fetal and infant tissue microstructure in human using conventional confocal microscopy to provide further insights into clinical translation of the developed approach.

Methods

Rodent Heart Preparations

All procedures were approved by the University of Utah Institutional Animal Care and Use Committee and followed the guidelines of the National Institutes of Health Guide for the Care and Use of Laboratory Animals.

Sprague–Dawley male rats of ≈300 g body weight were anesthetized with pentobarbital (40 mg/kg) and anticoagulated with heparin (500 IU/kg). Following intraperitoneal administration, hearts were rapidly excised and Langendorff-perfused with cold zero calcium Tyrode solution (in mmol/L: 92 NaCl, 11 dextrose, 4.4 KCl, 5 $MgCl_2$, 24 HEPES, 20 taurine, 5 creatine, 5 $C_3H_3NaO_3$, 1 NaH_2PO_4, 12.5 NaOH; pH 7.2; ≈10°C) at a flow rate of 10 to 15 mL/min.

For preparations of living hearts, these were continuously Langendorff-perfused with cold zero calcium Tyrode solution. Before imaging, 5 µL of fluorescent dye was applied to the epicardial or endocardial surface of the heart to label the extracellular space within regions of interest. The fluorescent dye was Alexa Fluor 488 conjugated to dextran with a molecular weight of 3 or 10 kDA (Invitrogen, Carlsbad, CA) dissolved in phosphate buffered saline (PBS) solution to a final concentration of 125 µg/mL.

For fixed tissue preparations, perfusion with Tyrode solution ceased after 5 minutes. Afterward, hearts were either perfused for 5 minutes with a zero calcium Tyrode solution containing wheat germ agglutinin (WGA) conjugated to CF488A (29022-1; Biotium, Hayward, CA; 1:100), followed by a 10-minute perfusion with Tyrode solution containing 4% paraformaldehyde (pH 7.2), or the hearts were immediately perfused with fixative. The hearts were then immersed in PBS containing 4% paraformaldehyde for 24 hours at 4°C. Tissue from the AWM, SAN, and AVN was dissected from the fixed hearts (Figure 1; Figures I and IIA in the online-only Data Supplement).

Immunofluorescent Labeling of Fixed Tissue

Preparations of fixed tissue were washed 3× in PBS and then permeabilized and blocked with PBS solution containing 0.5% Triton X-100 and 4% normal goat serum (16210-064; Gibco, Grand Island, NY) for 1 hour. After washing with PBS, preparations were bathed in Image-iT FX Signal Enhancer (I36933; Invitrogen) for 1 hour. Next, preparations were washed in PBS and incubated overnight with primary antibodies (antihyperpolarization-activated cyclic nucleotide-gated potassium channel 4 [HCN4, APC-052, Alomone Labs, Jerusalem, Israel; 1:800]; antisarcomeric α-actinin [ab9465, Abcam, Cambridge, MA; 1:400]; 4′,6-diamidino-2-phenylindole [DAPI, D1306, Invitrogen; 1:400]) in PBS incubation solution containing 0.5% Triton X-100 and 4% normal goat serum. The following day, preparations were washed 3× in PBS and incubated overnight with secondary goat antirabbit IgG (H+L) conjugated to either Alexa Fluor 488 or Alexa Fluor 555 (Invitrogen; 1:400) and goat antimouse IgG1 conjugated to Alexa Fluor 633 (Invitrogen; 1:200) in PBS incubation solution. The next day, preparations were washed 3× in PBS and stored in PBS solution until imaging. All labeling was performed on a laboratory platform rocker (S-2035-D; Labnet International Inc, Woodbridge, NJ) at room temperature.

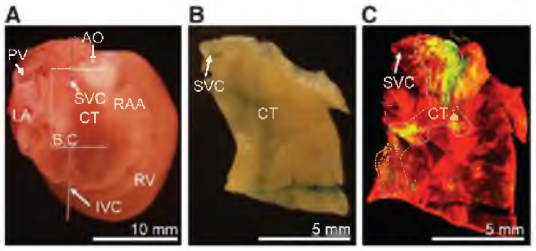

Figure 1. Preparation for localization and characterization of sinoatrial node tissue. **A**, Fixed rat heart shown from posterior-lateral. **B**, Tissue section from region marked in (**A**). **C**, Conventional confocal microscopic image of tissue preparation (**B**) labeled with antihyperpolarization-activated cyclic nucleotide-gated potassium channel 4 (green) and antisarcomeric α-actinin (red). AO indicates aorta; CT, crista terminalis; IVC, inferior vena cava; LA, left atrium; PV, pulmonary vein; RAA, right atrial appendage; RV, right ventricle; and SVC, superior vena cava.

Imaging of Fixed Tissue

Fixed atrial tissue preparations were imaged using a confocal microscope (Zeiss LSM 5 Duo; Zeiss, Jena, Germany) equipped with a 40× oil immersion lens with a numeric aperture of 1.3. Tissue samples were placed on a glass slide and a coverslip was placed on top of the tissue (Figure IIB in the online-only Data Supplement). The coverslip was gently pressed on the tissue, bringing its surface close to the glass slide. Fluorophores within the labeled preparations were individually excited for each image slice, alternating between 364, 488, 543, and 633 nm laser lines. The emitted light was collected through a longpass filter at 385 nm, bandpass filter for 505 to 555 nm, longpass filter at 560 nm, and longpass at 650 nm. This multi-track imaging protocol reduced cross-talk of the applied fluorophores. 3D image stacks were acquired at a spatial resolution of 0.2×0.2×0.2 µm in x-, y- and z-direction, respectively, a field of view of (x) 204.8 µm by (y) 204.8 µm, and depth (z) up to 50 µm. Details on the processing and visualization of images are provided in online-only Data Supplement.

Fourier Analysis of Tissue Microstructure

The spatial distributions of the extracellular space in images from AWM and nodal tissue were characterized from their Fourier spectra.[9] A discrete 2-dimensional (2D) Fourier transform was applied on xy images after multiplying them with a Gaussian window function. Intensities in circular sectors with an angle of 10° at spatial frequencies from 0.07 to 0.2 μm^{-1} were integrated from the image spectra. A measure of spatial regularity was determined from a ratio of summed intensities within 15° of the peak of the angular spectra to the overall sum of intensities in angular spectra.

Image Moment Analysis of Tissue Microstructure

Higher-order image moments were determined to characterize the spatial distributions of the extracellular space. Images were decomposed in subregions with a dimension of 64×64 pixels. A circular mask was applied to each subregion and the central second-order moment calculated.[10] Local orientation and scaling of the moment were derived from singular value decompositions. A histogram of local orientation angles was determined. A measure of spatial regularity was determined from the ratio of occurrence of an orientation angle within 15° of the peak of the occurrences to the overall occurrences.

FCM Imaging of Tissue in Living Hearts

2D image sequences of AWM, SAN, and AVN regions labeled with dextran-conjugated Alexa Fluor 488 were acquired using a fiber-optics confocal microscope (FCM1000; Leica Microsystems GmbH, Wetzlar, Germany) equipped with a custom fiber-optics microprobe (UltraMiniO; Mauna Kea Technologies, Paris, France). A schematic diagram of the FCM imaging setup is shown in Figure III in the online-only Data Supplement. Excitation of the fluorophore was at a wavelength of 488 nm and emitted light was collected at wavelengths 505 to 700 nm. 2D image sequences were acquired with a lateral resolution of 1.8×1.8 μm in x- and y-direction, an optical sectioning (z) of 10 μm, a field of view (xy) of 169 by 120 μm, depth (z) ≤50 μm, and frame rate of 12 Hz. The microprobe tip diameter was 2.6 mm, which simplified maneuvering of the microprobe. It was attached to a manual micromanipulator (M3301L; World Precision Instruments, Inc, Sarasota, FL) allowing for fine-precision 3D movement of the microprobe in proximity to the heart surface.

Processing and Visualization of FCM Images

The brightness and contrast of images acquired with the FCM1000 were auto-adjusted using the imadjust function in MATLAB (The Mathworks Inc, Natick, MA).

Statistical Analysis

Statistical data are presented as mean±SD. Statistical significance was assessed by 1-way ANOVA followed by post hoc Tukey–Kramer ($P<0.05$). A summary intensity (I_{15}) was determined from the averaged angle spectra that resulted from the image moment and Fourier analyses for conventional confocal microscopic and FCM images of AWM, SAN, and AVN tissue samples. I_{15} was defined as the sum of intensities along grouped orientation angles between −15° and +15° from the Fourier analyses. From the image moment analyses, I_{15} was determined from the sum of occurrences of local orientation along grouped orientation angles between −15° and +15°. A comparative intensity based on SD of intensities or occurrence of local orientation along grouped orientation angles between −89° and +90° was also determined (I_{std}). Differences in I_{15} of conventional confocal microscopic and FCM images of AWM, SAN, and AVN tissue samples were assessed. A similar analysis was done to determine significance based on I_{std}.

Human Heart Preparations, Immunofluorescent Labeling, and Imaging

Studies were designated as nonhuman subjects research and granted Institutional Review Board exemption by the University of Utah. We obtained deidentified, formalin-fixed sections from AWM, SAN, and AVN regions of 2 autopsy hearts. The autopsy hearts were from a 4-month-old infant and a 38-week-old fetus. Both did not have congenital heart disease. Preparations of fixed sections were washed 3× in PBS and incubated overnight with WGA conjugated to CF488A (Biotium; 1:25). The following day, preparations were washed 3× and stored in PBS solution until imaging. We applied conventional confocal microscopy and texture analyses as described above.

Results

Imaging of Cardiac Tissue Using Conventional Confocal Microscopy

We hypothesized that fluorescent labeling of extracellular space and imaging with conventional confocal microscopy allows for identification of nodal tissue. We tested this hypothesis on tissue preparations from adult Sprague–Dawley rat hearts. Locations of SAN and AVN in this species are grossly similar as in other mammals including human, rabbit, and pig.

Cardiac tissue preparations were dissected from SAN and AVN regions using anatomic landmarks as described above (Figure 1; Figure I in the online-only Data Supplement). Briefly, SAN tissue was dissected from the junction of the superior vena cava and right atrium, and AVN tissue was dissected from the region of the membranous septum, which is bordered by the septal leaflet of the tricuspid valve, coronary sinus, and the tendon of Todaro. Tissue dissections were labeled with DAPI to mark nuclei and WGA conjugated to a fluorophore to label constituents of the extracellular space. WGA binds to glycoconjugates of the extracellular space, including those associated with collagen strands and the glycocalyx on the surface and periphery of cell membranes.[11,12] Additionally, tissues were labeled with antibodies for both HCN4 and sarcomeric α-actinin. HCN4 labeling has been previously established as a positive marker of nodal cells.[13–16] Sarcomeric α-actinin served to identify cardiomyocytes. Conventional confocal microscopic imaging of the tissue preparations yielded 3D distributions of the 4 labels at submicrometer resolution. Image stacks from a preparation of AWM are presented in Figure 2A through 2H. A hallmark of this tissue is the dense and aligned arrangement of myocytes, which is reflected in the striated distribution of WGA (Figure 2B). Fluorescence associated with anti-HCN4 was absent (Figure 2C). The myocytes labeled positive for α-actinin (Figure 2D). The myocytes were covered by an epicardial layer with a thickness of 3.6 μm. Figure 2I through 2P shows image stacks from SAN tissue. The stacks comprised 3 distinct layers (ie, epicardium, nodal cells, and subnodal layer of AWM myocytes). In this stack, the epicardial and nodal layer had a thickness of 2.4 and 11.2 μm, respectively. The microstructural arrangement in the nodal layer was in various aspects different from the arrangement in the subnodal layer of AWM myocytes in this stack (Figure 2N versus Figure 2M). It was also very different from the arrangement of myocytes in the stack from AWM tissue (Figure 2E). SAN cells formed a highly irregular reticulum and had notably smaller diameters than myocytes of the AWM. However, SAN cells also exhibited similar features of striated myocytes (ie, the regular transversal striations of the α-actinin signal with a longitudinal spacing of ≈2 μm). The extracellular space in the SAN layer was more prominent than in AWM and comprised oval-shaped clearings with variable sizes. Figure IV in the online-only Data Supplement illustrates image stacks from the compact region of the AVN, which presented a microstructural arrangement similar to SAN tissue. Here, the epicardial layer had a thickness of 0.8 μm. The orientation of AVN cells was diverse, and they formed a reticulum with ample extracellular space. Figure V in the online-only Data Supplement presents unprocessed image stacks corresponding to Figure 2 and Figure IV in the online-only Data Supplement.

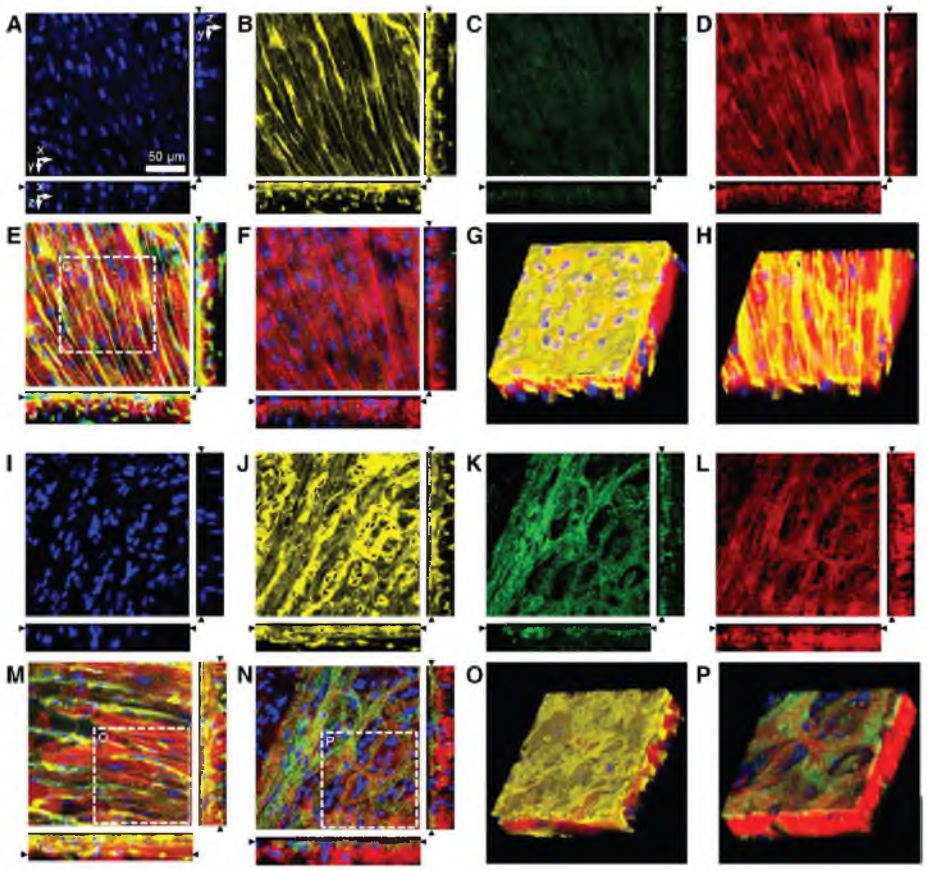

Figure 2. Conventional confocal microscopy of atrial working myocardium (AWM) and sinoatrial node (SAN). Image stacks were acquired from the epicardial surface into subepicardial (**A–F**) AWM and (**I–N**) SAN tissue labeled with (**A**, **I**) 4′,6-diamidino-2-phenylindole (DAPI), (**B**, **J**) wheat germ agglutinin (WGA), (**C**, **K**) antihyperpolarization-activated cyclic nucleotide-gated potassium channel 4, and (**D**, **L**) antisarcomeric α-actinin. **E**, Overlaid DAPI, WGA, and antisarcomeric α-actinin images illustrate the regular, dense arrangement of myocytes in AWM. **F**, Overlaid DAPI, antiHCN4, and antisarcomeric α-actinin images. **G**, 3-dimensional reconstruction of region marked in (**E**) displaying AWM beneath an epicardial layer with a thickness of 3.6 µm. **H**, 3-dimensional reconstruction of AWM after cropping of epicardial layer. SAN tissue exhibits a layer of HCN4-positive, reticular-arranged myocytes and oval-shaped clearings of variable sizes beneath an epicardial layer. Below this layer were regular-arranged HCN4-negative myocytes. **M**, Overlaid DAPI, WGA, and antisarcomeric α-actinin images illustrate the regular, subnodal myocyte arrangement at a depth of 26.6 µm. **N**, Overlaid DAPI, anti-HCN4, and antisarcomeric α-actinin images illustrate the irregular arrangement of HCN4-positive myocytes at a depth of 5.6 µm. **O**, 3-dimensional reconstruction of region marked in (**M**) reveal the 3-layered arrangement of SAN tissue. **P**, Reconstruction of region marked in **N** presents the SAN and AWM layer after cropping of epicardial layer. Scale bar in **A** applies to **B** through **F** and **I** through **N**.

Statistical analyses were performed on acquired images from a group of animals (Table). Image analysis from the AWM and SAN tissue showed that the epicardial layer had a thickness of 7.5±3.5 and 5.5±2.9 µm, respectively. In the compact AVN the thickness of the endocardial layer was 3.2±2.4 µm. In SAN and AVN tissue, the thickness of the nodal layer was 10.3±3.2 and 17.2±8.7 µm, respectively. Analysis of HCN4 signal intensities showed that these were significantly (P<0.005) higher in the nodal layer of the SAN and AVN preparations than in the AWM (Figure VI in the online-only Data Supplement). Also, intensities in the nodal layers were significantly higher than in their respective subnodal layers. We did not find significant differences between HCN4 intensities in the AWM and in subnodal SAN and AVN layers.

Quantitative Characterization of Tissue Microstructure

We evaluated the ability of 2 methods of 2D texture analysis to discriminate between AWM and nodal tissue using WGA images. The first method measured the texture orientation from Fourier transformed images. The second method characterized texture orientation from second-order image moments of image regions. Figure 3A through 3C presents exemplary images and results from these analyses applied to the WGA images presented in Figures 2B and 2J and Figure IVB in the online-only Data Supplement. These images were overlaid with glyphs characterizing local orientation and anisotropy ratio of second-order image moments. It is apparent that the microstructural arrangement of AWM (Figure 3A) differs from that of nodal tissue (Figure 3B and 3C).

Table. Numbers of Images and Animals Used for Image Analysis

Tissue Type	Images/Animals		
	Imaging of Fixed Tissue	Imaging of Living Hearts	Depth and Thickness Profiles
AWM	16/6	37/7	13/6
SAN	13/6	40/6	11/6
AVN	10/6	29/6	9/6

AVN indicates atrioventricular node; AWM, atrial working myocardium; and SAN, sinoatrial node.

In this example, both methods of texture analysis indicated a larger degree of orientation in AWM than in SAN and AVN tissue (Figure 3D and 3E).

Imaging of Living Hearts Using FCM

We hypothesized that imaging with FCM using a fluorescent marker of the extracellular space will allow discrimination of tissue types in living hearts. In these studies, we used dextran-conjugated fluorophores with a molecular weight of 10 kDa and a FCM microprobe with a working distance of 50 µm. Previous studies demonstrated that dextran conjugates of 3 to 10 kDa molecular weight penetrate endothelial endocardium, endothelial epicardium, and myocardial capillary endothelium in rat,[17] and through the epicardium into ventricular myocardium in rabbit.[18] However, dextran conjugates of this molecular weight do not penetrate intact cell membranes[19] and thus label specifically the extracellular space. FCM image sequences were acquired at a rate of 12 images/s from the AWM and nodal regions following topical application of extracellular fluorophore (Figure IIIB in the online-only Data Supplement). The image sequences of nodal tissue were acquired from an intact living heart from similar regions that were excised for the aforementioned conventional confocal microscopy study (Figure 1; Figure I in the online-only Data Supplement). Examples of FCM image sequence are shown in Movie I in the online-only Data Supplement for AWM and Movie II in the online-only Data Supplement for SAN. In these images bright and dark regions correspond to fluorescence in the extracellular spaces and the absence of fluorescence in the intracellular spaces, respectively. The average SNR in 17 image sequences was 12.1±3.3 (see online-only Data Supplement for details). Images from the dextran-labeled AWM and nodal regions using FCM bear resemblance to WGA images using conventional confocal microscopy. FCM images of the AWM exhibited regular striations (Figure 3F) as found previously in WGA images using conventional confocal microscopy (Figure 2B). In contrast, images from nodal regions revealed irregular microstructural arrangements (Figure 3G and 3H) similar as in WGA images (Figure 2J; Figure IVB in the online-only Data Supplement).

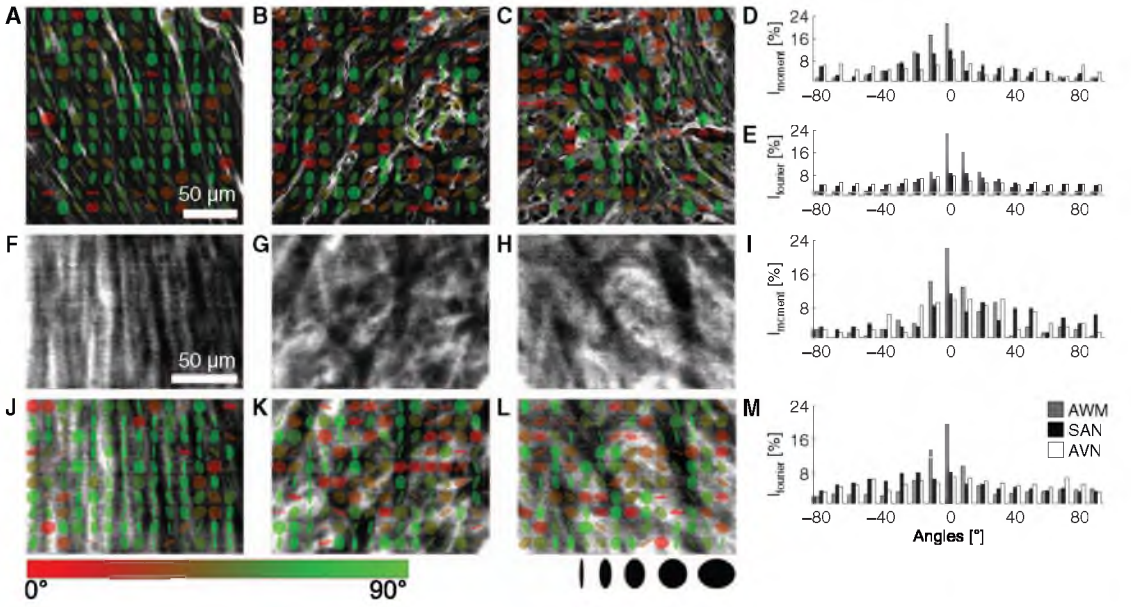

Figure 3. Quantitative characterization of microstructure in fixed and living tissue. Wheat germ agglutinin (WGA) images of fixed tissue preparations from atrial working myocardium (AWM; Figure 2B), sinoatrial node (SAN; Figure 2J), and atrioventricular node (AVN) regions (Figure IVB in the online-only Data Supplement) were analyzed using second-order moments. (**A**) AWM, (**B**) SAN, and (**C**) AVN images overlaid with glyphs visualize orientation of the minor eigen-axis (color-coded, bar) and anisotropy ratio of eigen-values (shape-coded) of local image moments. Histogram of orientations based on (**D**) second-order moments and (**E**) Fourier transform. Kurtosis of histograms from second-order moment and Fourier analysis is a marker of myocyte alignment. Fiber-optics confocal microscopy images of living tissue from (**F**) AWM, (**G**) SAN, and (**H**) AVN regions labeled with a dextran–fluorophore conjugate. Living tissues exhibited similar microstructural features as in fixed tissues (**A–C**). (**J**) AWM, (**K**) SAN, and (**L**) AVN images overlaid with glyphs. Quantitative analysis of (**I**) second-order moments and (**M**) Fourier transforms suggest larger myocyte alignment in AWM regions versus SAN or AVN. Scale bar in **A** applies to **B** and **C**. Scale bar in **F** applies to **G** and **H** and **J** through **L**.

Characterization of FCM Images

We investigated if tissue types can be discriminated in images from FCM using our 2 methods of texture analysis. Examples of this evaluation are presented in Figure 3J through 3L. The FCM images shown in Figure 3F through 3H were overlaid with glyphs characterizing local orientation and anisotropy ratio of second-order image moments. Fourier and second-order image moment analysis of the image from the AWM demonstrated a prominent texture orientation (Figure 3I and 3M). Nodal tissue did not feature a similar degree of orientation and the intensities were approximately uniform over the range of angles.

Statistical Evaluation of Approach for Tissue Discrimination

Texture orientation from second-order image moments and Fourier transforms of sets of WGA (Figure 4A and 4E) and dextran-labeled images (Figure 4B and 4F) were obtained using conventional confocal microscopy and FCM, respectively. The resulting intensity and local orientation profiles from these sets of images were similar to those presented for exemplary images (Figure 3D and 3E versus Figure 4A and 4E and Figure 3I and 3M versus Figure 4B and Figure 4F). We used the sum of intensities and occurrence of local orientation for angles between −15° and +15° as a measure of spatial regularity. The summary intensity ($I_{\pm 15}$) was found to be significantly different in images of AWM and nodal tissue from both conventional confocal microscopy and FCM (Figure 4C and 4G). Similarly, the SD (I_{std}) of intensity profiles allowed discrimination of nodal and AWM tissue acquired with conventional confocal microscopy or FCM (Figure 4D and 4H).

Imaging and Characterization of Human Tissue Microstructure

We investigated fetal and infant tissue microstructure in human. We observed similar microstructural features in human AWM tissue as described above for our rodent model (Figure 5A and 5B versus Figure 2B). The thickness of the epicardial layer in the fetal and infant AWM tissues was 11.2 and 14.6 μm, respectively. Features of AVN regions were similar in rodent and human (Figure 5C versus Figure IVB in the online-only Data Supplement). The thickness of the endocardial layer in the fetal AVN tissue was 3.6 μm. In addition, texture analysis based on second-order image moments and Fourier transforms indicated a larger degree of orientation in AWM than in AVN tissue (Figure 5D and 5E; Figure VII in the online-only Data Supplement).

Discussion

The microstructure of the SAN and AVN has been used for identification since their discovery by Keith and Flack in 1907[20] and Tawara in 1906,[21] respectively. These studies were based on thin sections of nodal tissues, which revealed the characteristic microstructure using light microscopy. Here, we demonstrate that nodal tissue types can be identified in living hearts based on confocal microscopy and fluorescent labeling of the extracellular space. Our approach demonstrated that confocal microscopy can acquire image data at the appropriate specific depth within the intact heart. We found that AWM, SAN, and AVN tissue is beneath a thin surface layer of tissue that does not obstruct confocal microscopic imaging in the rodent model (Movies III-VIII in the online-only Data Supplement). In our exemplary study on human tissue we found AWM and AVN tissue at similar small depths. We also introduced methods for texture analysis, which provided us with a quantitative tool for automated tissue identification. We suggest that the presented approach has the potential to identify nodal tissue in the in situ heart and complement other methods for tissue identification in a clinical setting. An obvious clinical application is related to pediatric reconstructive heart surgery. The described approach allows surgeons to map out the location of nodal tissue and thus avoid tissue damage, such as what might occur by suture injury. Suture injury is a common clinical cause for SAN and AVN dysfunction.[22,23] In

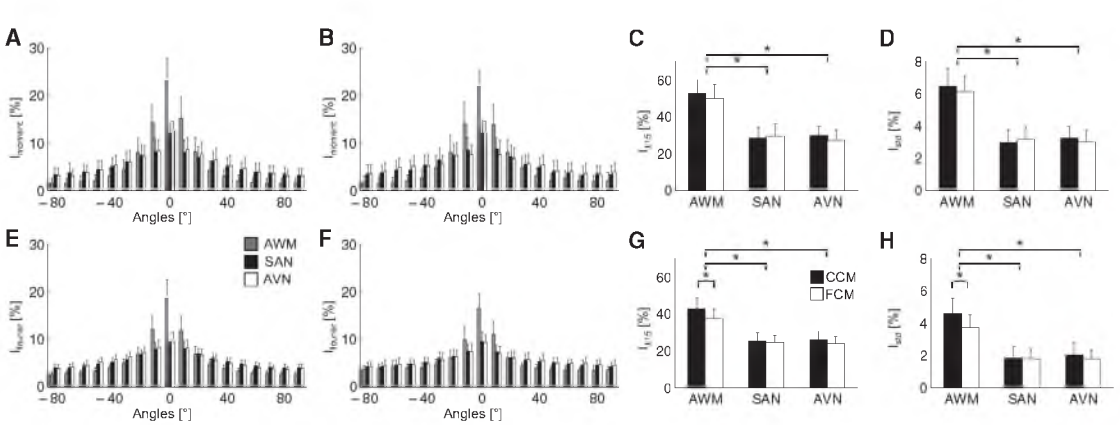

Figure 4. Statistical characterization of images from atrial working myocardium (AWM), sinoatrial node (SAN), and atrioventricular node (AVN) regions. Histograms of orientations calculated from (**A**) second-order moments and (**B**) Fourier transforms of images from fixed, wheat germ agglutinin–labeled tissue acquired with conventional confocal microscopy (CCM). Histograms of orientations from (**E**) second-order moments and (**F**) Fourier transforms of FCM images from tissue labeled with a dextran–fluorophore conjugate. $I_{\pm 15}$ of AWM and nodal tissues were significantly different using the (**C**) second-order image moment and (**G**) Fourier analyses. **D** and **H**, I_{std} showed similar significant differences. *P<0.05, compared with nodal tissue (1-way ANOVA with post hoc Tukey–Kramer).

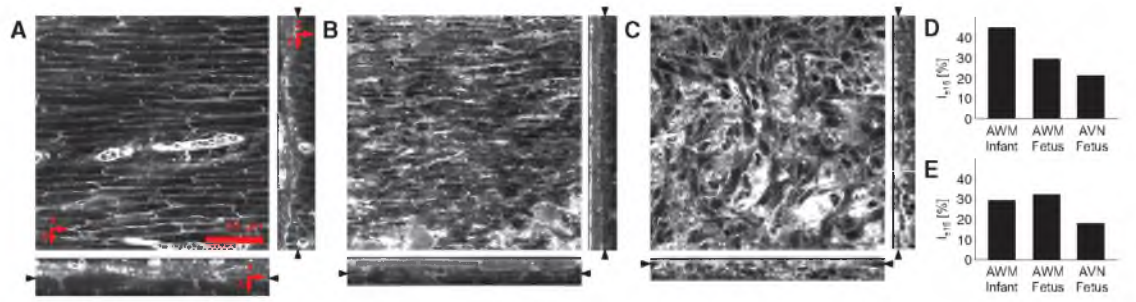

Figure 5. Conventional confocal microscopic images from human cardiac tissue. Image stacks were acquired from the epicardial surface into subepicardial atrial working myocardium (AWM) from (**A**) infant and (**B**) fetal heart. **C**, Image stack from endocardial surface into subendocardial atrioventricular node (AVN) tissue from fetal heart. Analysis of (**D**) second-order moments and (**E**) Fourier transforms of (**A–C**) indicate higher myocyte alignment in AWM versus AVN region, but a similar myocyte alignment in AWM regions in the infant and fetal heart.

instances where repair must be made relatively close to nodal regions, surgeon could place sutures or incision lines with a higher level of confidence using the FCM. We suggest that our approach for tissue identification can help to reduce the incidence of complications caused by injury of nodal tissues.

FCM imaging complements other emerging technologies suggested for in vivo tissue imaging, such as micro-optical coherence tomography,[24] conventional fluorescence imaging with miniaturized microscopes,[25] and fluorescence spectroscopy.[26] All these technologies have the potential to provide clinicians with real-time visual information beyond reflected visible light. In contrast to the other emerging imaging technologies, FCM systems are already available commercially and Food and Drug Administration approved for applications in the gastrointestinal[27] and pulmonary tracts.[28] However, the application of FCM in other clinical fields is hampered, in part, because of the lack of reliable fluorescent labeling strategies. Commonly, fluorescent labels consist of fluorophores conjugated to a ligand. The ligand typically targets a specific site of interest. Here, we investigated dextran conjugated to Alexa Fluor 488 to target the extracellular space. We demonstrated that the dextran conjugate was able to label the extracellular space in the living perfused heart with a high SNR. The labeling allowed for visualization of tissue microstructure and subsequent image processing and quantitative analysis.

A limitation of the presented approach for clinical translation is the potential toxicity of fluorophores. The toxicity of many fluorophores has been recently reviewed,[29] and several fluorophores are routinely used for human applications. The quantity of dextran–Alexa conjugate used in this study was ≈50 pg per imaging trial. While no toxicity-related information is available for this conjugate and Alexa Fluor 488, other hydrophilic conjugates of dextran and Food and Drug Administration–approved fluorophores are available. A promising fluorophore for labeling of the extracellular space is Fluorescite,® which is an Food and Drug Administration class IIa drug and already approved for use in ophthalmic angiography.[30] A study exploring the use of intravenously injected Fluorescite® in FCM imaging of the gastrointestinal tract in vivo produced a SNR from acquired images that was comparable to the value obtained in our living heart studies.[31]

We developed our approach based on a microstructural characterization of cardiac tissue using conventional 3D confocal microscopy. The thicknesses of endocardial and epicardial layers determined from WGA images indicated that these layers do not constitute obstacles to confocal imaging of underlying tissue layers, for instance by depth-dependent attenuation of the excitation and emitted light. We used labeling for HCN4 to confirm the presence of nodal tissue and measured the thickness of nodal layers. The measured thickness of the nodal layers is sufficiently large versus the thickness of optical sections acquired with FCM (≈10 μm). We suggest that this type of microstructural analysis can provide important input for the development of imaging microprobes that are specialized for imaging applications. This analysis can assist in the development of microprobes tailored to age groups, disease states, and anatomic regions for FCM imaging of cardiac and other tissues.

Acknowledgments

We are grateful to Dr F. Lacombe (Mauna Kea Technologies, Paris, France) for providing us with microprobes and L.K. Erickson, PA(ASCP) (Department of Anatomic Pathology, Primary Children's Medical Center, Salt Lake City, Utah) for his help with human heart specimens.

Sources of Funding

This research was supported by the US National Institutes of Health (R21 HL108099), the Nora Eccles Treadwell Foundation, and the Utah Science Technology and Research initiative.

Disclosures

None.

References

1. Parker SE, Mai CT, Canfield MA, Rickard R, Wang Y, Meyer RE, Anderson P, Mason CA, Collins JS, Kirby RS, Correa A; National Birth Defects Prevention Network. Updated National Birth Prevalence estimates for selected birth defects in the United States, 2004-2006. *Birth Defects Res A Clin Mol Teratol*. 2010;88:1008–1016.
2. Wolff GS, Rowland TW, Ellison RC. Surgically induced right bundle-branch block with left anterior hemiblock. An ominous sign in postoperative tetralogy of Fallot. *Circulation*. 1972;46:587–594.
3. Gross GJ, Chiu CC, Hamilton RM, Kirsh JA, Stephenson EA. Natural history of postoperative heart block in congenital heart disease: implications for pacing intervention. *Heart Rhythm*. 2006;3:601–604.
4. Merin O, Ilan M, Oren A, Fink D, Deeb M, Bitran D, Silberman S. Permanent pacemaker implantation following cardiac surgery: indications and long-term follow-up. *Pacing Clin Electrophysiol*. 2009;32:7–12.
5. Bogers AJ, Head SJ, de Jong PL, Witsenburg M, Kappetein AP. Long term follow up after surgery in congenitally corrected transposition of the great

arteries with a right ventricle in the systemic circulation. *J Cardiothorac Surg*. 2010;5:74.
6. Graham TP Jr, Bernard YD, Mellen BG, Celermajer D, Baumgartner H, Cetta F, Connolly HM, Davidson WR, Dellborg M, Foster E, Gersony WM, Gessner IH, Hurwitz RA, Kaemmerer H, Kugler JD, Murphy DJ, Noonan JA, Morris C, Perloff JK, Sanders SP, Sutherland JL. Long-term outcome in congenitally corrected transposition of the great arteries: a multi-institutional study. *J Am Coll Cardiol*. 2000;36:255–261.
7. Anderson RH, Ho SY, Becker AE. The surgical anatomy of the conduction tissues. *Thorax*. 1983;38:408–420.
8. Smith A, Ho SY, Anderson RH, Connell MG, Arnold R, Wilkinson JL, Cook AC. The diverse cardiac morphology seen in hearts with isomerism of the atrial appendages with reference to the disposition of the specialised conduction system. *Cardiol Young*. 2006;16:437–454.
9. Brigham EO. *The Fast Fourier Transform and Its Applications*. Englewood Cliffs: Prentice Hall; 1988.
10. Gonzalez RC, Woods RE. *Digital Image Processing*. Reading, MA: Addison-Wesley; 1992.
11. Bhavanandan VP, Katlic AW. The interaction of wheat germ agglutinin with sialoglycoproteins. The role of sialic acid. *J Biol Chem*. 1979;254:4000–4008.
12. Söderström KO. Lectin binding to collagen strands in histologic tissue sections. *Histochemistry*. 1987;87:557–560.
13. Chandler NJ, Greener ID, Tellez JO, Inada S, Musa H, Molenaar P, Difrancesco D, Baruscotti M, Longhi R, Anderson RH, Billeter R, Sharma V, Sigg DC, Boyett MR, Dobrzynski H. Molecular architecture of the human sinus node: insights into the function of the cardiac pacemaker. *Circulation*. 2009;119:1562–1575.
14. Yoo S, Dobrzynski H, Fedorov VV, Xu SZ, Yamanushi TT, Jones SA, Yamamoto M, Nikolski VP, Efimov IR, Boyett MR. Localization of Na+ channel isoforms at the atrioventricular junction and atrioventricular node in the rat. *Circulation*. 2006;114:1360–1371.
15. Yamamoto M, Dobrzynski H, Tellez J, Niwa R, Billeter R, Honjo H, Kodama I, Boyett MR. Extended atrial conduction system characterised by the expression of the HCN4 channel and connexin45. *Cardiovasc Res*. 2006;72:271–281.
16. Brioschi C, Micheloni S, Tellez JO, Pisoni G, Longhi R, Moroni P, Billeter R, Barbuti A, Dobrzynski H, Boyett MR, DiFrancesco D, Baruscotti M. Distribution of the pacemaker HCN4 channel mRNA and protein in the rabbit sinoatrial node. *J Mol Cell Cardiol*. 2009;47:221–227.
17. Andries LJ, Brutsaert DL. Endocardial endothelium in the rat: junctional organization and permeability. *Cell Tissue Res*. 1994;277:391–400.
18. Lasher RA, Hitchcock RW, Sachse FB. Towards modeling of cardiac micro-structure with catheter-based confocal microscopy: a novel approach for dye delivery and tissue characterization. *IEEE Trans Med Imaging*. 2009;28:1156–1164.
19. Savio-Galimberti E, Frank J, Inoue M, Goldhaber JI, Cannell MB, Bridge JH, Sachse FB. Novel features of the rabbit transverse tubular system revealed by quantitative analysis of three-dimensional reconstructions from confocal images. *Biophys J*. 2008;95:2053–2062.
20. Keith A, Flack M. The form and nature of the muscular connections between the primary divisions of the vertebrate heart. *J Anat Physiol*. 1907;41(Pt 3):172–189.
21. Tawara S. *Das Reizleitungssystem des Saeugetierherzens*. Jena: Fischer; 1906.
22. Takahashi H, Oshima Y, Yoshida M, Yamaguchi M, Okada K, Okita Y. Sinus node dysfunction after repair of partial anomalous pulmonary venous connection. *J Thorac Cardiovasc Surg*. 2008;136:329–334.
23. Mongeon FP, Burkhart HM, Ammash NM, Dearani JA, Li Z, Warnes CA, Connolly HM. Indications and outcomes of surgical closure of ventricular septal defect in adults. *JACC Cardiovasc Interv*. 2010;3:290–297.
24. Liu L, Gardecki JA, Nadkarni SK, Toussaint JD, Yagi Y, Bouma BE, Tearney GJ. Imaging the subcellular structure of human coronary atherosclerosis using micro-optical coherence tomography. *Nat Med*. 2011;17:1010–1014.
25. Ghosh KK, Burns LD, Cocker ED, Nimmerjahn A, Ziv Y, Gamal AE, Schnitzer MJ. Miniaturized integration of a fluorescence microscope. *Nat Methods*. 2011;8:871–878.
26. Venius J, Bagdonas S, Zurauskas E, Rotomskis R. Visualization of human heart conduction system by means of fluorescence spectroscopy. *J Biomed Opt*. 2011;16:107001.
27. Buchner AM, Shahid MW, Heckman MG, Krishna M, Ghabril M, Hasan M, Crook JE, Gomez V, Raimondo M, Woodward T, Wolfsen HC, Wallace MB. Comparison of probe-based confocal laser endomicroscopy with virtual chromoendoscopy for classification of colon polyps. *Gastroenterology*. 2010;138:834–842.
28. Salaun M, Roussel F, Bourg-Heckly G, Vever-Bizet C, Dominique S, Genevois A, Jounieaux V, Zalcman G, Bergot E, Jean-Michel V, Thiberville L. In vivo probe-based confocal laser endomicroscopy in amiodarone-related pneumonia. *Eur Respir J*. September 27, 2012. doi: 10.1183/09031936.00191911. http://erj.ersjournals.com/content/early/2012/09/27/09031936.00191911.long. July 25, 2013.
29. Alford R, Simpson HM, Duberman J, Hill GC, Ogawa M, Regino C, Kobayashi H, Choyke PL. Toxicity of organic fluorophores used in molecular imaging: literature review. *Mol Imaging*. 2009;8:341–354.
30. Blauth CI, Arnold JV, Schulenberg WE, McCartney AC, Taylor KM. Cerebral microembolism during cardiopulmonary bypass. Retinal microvascular studies ***in vivo*** with fluorescein angiography. *J Thorac Cardiovasc Surg*. 1988;95:668–676.
31. Shahid MW, Crook JE, Meining A, Perchant A, Buchner A, Gomez V, Wallace MB. Exploring the optimal fluorescein dose in probe-based confocal laser endomicroscopy for colonic imaging. *J Interv Gastroenterol*. 2011;1:166–171.

CLINICAL PERSPECTIVE

Open heart reconstructive surgery is the state-of-the-art approach to repair congenital heart defects in neonates. Complications of these surgeries are trauma to the sinoatrial and atrioventricular node. Patients with persistent complications after surgery require cardiac rhythm management using implantable pacemakers. The need for implantation of permanent pacemakers after these surgeries ranges from 1% to 45%. A cause for these complications is that nodal tissues are not visible using surgical loupes or microscopes. Nodal tissues are commonly identified from anatomic landmarks. However, identification in hearts with congenital defects can be hindered by individual anatomic variations. In this study, we introduce an approach for identification of cardiac tissue in cardioplegic hearts based on fiber-optics confocal microscopy and fluorescent labeling. A particular clinical application is in pediatric reconstructive heart surgery. Our investigations on cardiac tissues in a rodent model and human autopsy hearts indicate that surgeons can apply the developed approach to map locations of nodal tissues. An important application of fiber-optics confocal microscopy is the repair of defects in proximity to nodal regions. Further development of the presented approach may help to reduce the incidence of complications caused by injury of nodal tissues.

SUPPLEMENTAL MATERIAL

Supplemental Methods

Processing and Visualization of Images from Fixed Tissue. The three-dimensional image stacks were corrected for background signals and depth-dependent attenuation.[1, 2] We applied the Richardson-Lucy algorithm based on measured point spread functions (PSFs) to deconvolve the image stacks. 3D volume visualizations of exemplary image stacks of AWM, SAN, and AVN were produced using VolView (Kitware, Inc. Clifton Park, New York). The depth of the epicardial tissue layer was detected from the WGA associated signal. WGA signal intensity from XY images was averaged along the z-direction for samples of AWM, SAN and AVN tissue. The maximal increase and decrease of averaged WGA signal served as a marker of the start and end of an epicardial layer. The depth of nodal tissue was detected from the HCN4 associated signal using a similar approach. The maximal increase and decrease of averaged HCN4 signal served as a marker of the start and end of a nodal tissue layer.

Signal-To-Noise Ratio (SNR). The SNR was calculated from image sequences of SAN regions labeled with dextran conjugated Alexa Fluor 488 and acquired with a fiber-optics confocal microscope. SNR is defined as the ratio between the mean of the signal and the standard deviation of the signal. In our case, regions of interest (ROI) of approximately 700 pixels were selected that represented an area of high signal intensity and an area of low signal intensity for each image sequence. These high and low intensity areas corresponded to regions with both signal and noise-only regions, respectively. An average SNR was determined based on background corrected image sequences. Image sequences with an SNR below two deviations of the average SNR were excluded from Fourier and image moment analyses

Quantitative Analysis of HCN4 Signal Intensity. Signal and background intensities were measured from acquired images of fluorescent dye solutions excited with the 543 nm laser line. We sampled those intensities in a range of laser powers, gains, and pixel dwell times. A three-dimensional calibration curve was calculated based on the measured mean intensities for the imaged solution with respect to the sampled laser powers, gains, and pixel dwell times. The AWM, nodal and subnodal layers were determined based on WGA and HCN4 depth profiles generated from image stacks of rat AWM (n = 7/4), SAN (n = 5/4), and AVN (n = 6/3). Sample size n is denoted as $n = I/A$ with I = images and A = animals. The HCN4 mean intensities from these layers were corrected based on the established calibration curve in a similar manner as used to correct depth dependent attenuation.

References

1. Lackey DP, Carruth ED, Lasher RA, Boenisch J, Sachse FB, Hitchcock RW. Three-dimensional modeling and quantitative analysis of gap junction distributions in cardiac tissue. *Ann. Biomed. Eng.* 2011;39:2683-2694
2. Lasher RA, Hitchcock RW, Sachse FB. Towards modeling of cardiac micro-structure with catheter-based confocal microscopy: A novel approach for dye delivery and tissue characterization. *IEEE Trans Med Imaging*. 2009;28:1156-1164

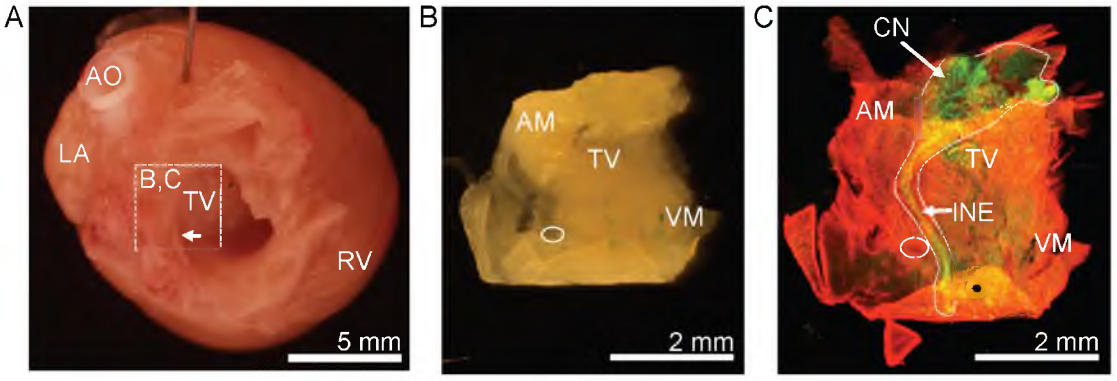

Supplemental Figure I. Preparation for localization and characterization of AVN tissue. (**A**) Fixed rat heart with right atrial lateral wall and right atrial appendage removed shown from cranial. Arrow indicates location of coronary sinus. (**B**) Tissue section from region marked in (**A**). (**C**) Conventional confocal microscopic image of tissue preparation in (**B**) labeled for anti-HCN4 (**green**) and anti-sarcomeric α-actinin (**red**). HCN4-positive regions were outlined region. Circle in (**B,C**) marks location of coronary sinus. AM, atrial muscle; AO, aorta; CN, compact node; INE, inferior nodal extension; LA, left atrium, RV, right ventricle; TV, tricuspid valve; VM, ventricular muscle.

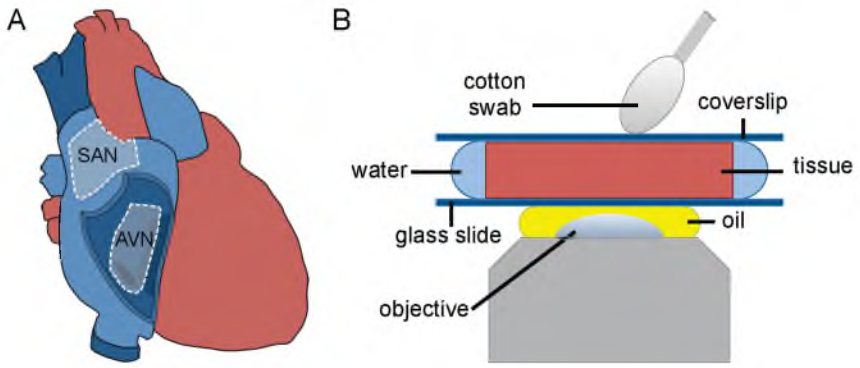

Supplemental Figure II. Preparation and imaging of fixed cardiac tissue with conventional confocal microscopy. (**A**) Sketch of heart with SAN and AVN regions. Tissue preparations were excised from those regions after fixation of the heart. (**B**) Schematic of the imaging setup. Fluorescently labeled tissue was brought in close proximity to the glass slide for imaging.

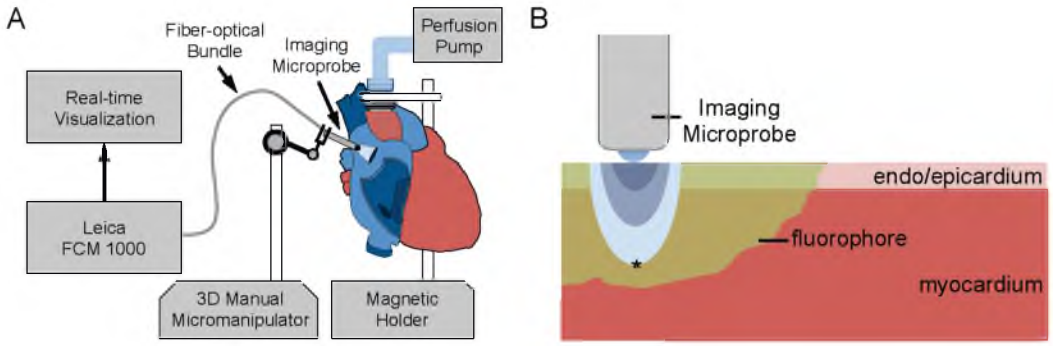

Supplemental Figure III. Preparation and imaging of living cardiac tissue with FCM. (**A**) Setup for FCM imaging of living heart. The 3D manual micromanipulator is used to maneuver the imaging microprobe in close proximity to the epicardial or endocardial surface. (**B**) Illustration of imaging of 2-layered tissue. The fluorophore diffuses into the tissues after superficial application. The imaged region (*) is beneath a thin epicardial or endocardial tissue layer.

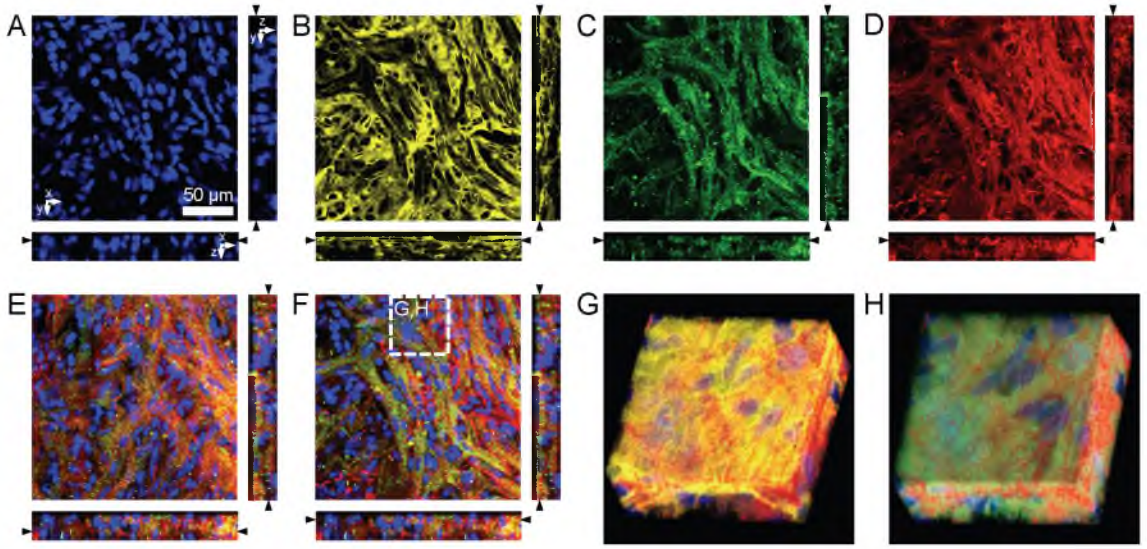

Supplemental Figure IV. Confocal microscopic images of AVN tissue. The tissue was labeled with (**A**) DAPI, (**B**) WGA, (**C**) anti-HCN4, and (**D**) anti-sarcomeric α-actinin. Irregular shaped, HCN-4 positive myocytes were located beneath the epicardial layer. An overlay of DAPI, anti-HCN4, anti-sarcomeric α-actinin images illustrates the irregular arrangement of myocytes located (**E**) at a depth of 16.2 µm and (**F**) beneath the epicardial layer. (**G**) Three-dimensional reconstruction of the region marked in (**F**) labeled with DAPI, WGA, and anti-sarcomeric α-actinin. (**H**) Three-dimensional reconstruction of the region marked in (**F**) after removal of the endocardial layer reveal the complex arrangement of AVN tissue. Scale bar in (**A**) applies to (**B-F**).

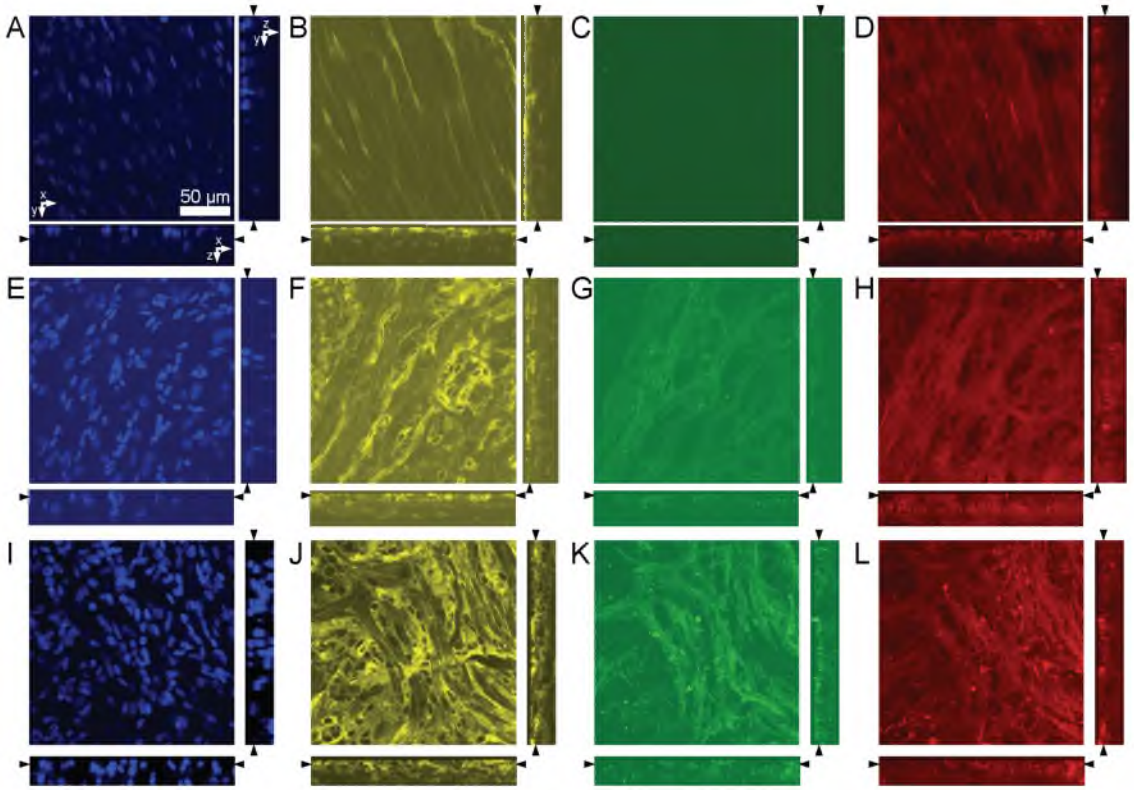

Supplemental Figure V. Unprocessed images acquired with conventional confocal microscopy. Cross-sections through unprocessed image stacks corresponding to those presented in (**A-D**) Figure 2, (**E-H**) Figure 3, and (**I-L**) Supplemental Figure 3.

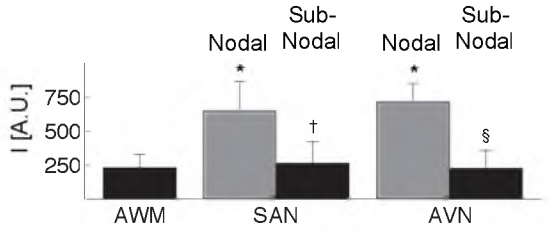

Supplemental Figure VI. Quantitative analysis of HCN4 signal intensity in AWM (n = 7/4), SAN (n = 5/4), and AVN (n = 6/3) tissue. The HCN4 signal in the SAN region was approximately 2.5 times higher in the nodal layer as compared to its subnodal layer. We found that the HCN4 intensity in the nodal layer of the AVN region was 3.1 times higher than its subnodal layer. The HCN4 level in the nodal layers of the SAN and AVN regions were 2.8 and 3.1 times higher respectively as compared to the HCN4 level in the AWM region. *P < 0.005, compared with AWM. †P < 0.005, compared with SAN nodal layer. §P < 0.005, compared with AVN nodal layer. Sample size n is denoted as n = I/A where I = images and A = animals.

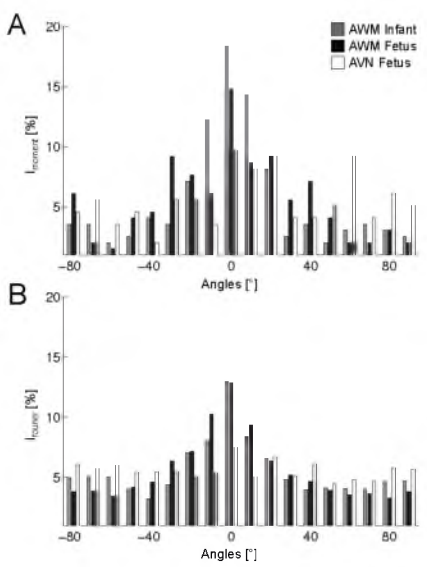

Supplemental Figure VII. Histogram of orientations based on (**A**) 2nd order image moments and (**B**) Fourier transforms of human AWM and AVN images shown in Figure 5.

Legends for Movies

Movie I. Real-time live imaging of rat AWM. The AWM tissue was labeled with dextran conjugated Alexa Fluor 488 and imaged using FCM. The dark regions shown are of muscle cells and the bright regions are of the fluorophore. The image sequence was taken at a rate of 20 images/s using a manual micromanipulator to maneuver the imaging microprobe in the region of interest.

Movie II. Real-time live imaging of rat SAN. The same imaging protocol used to acquire recordings in Movie I was followed.

Movie III. Three-dimensional reconstruction of AWM. The tissue was imaged using conventional confocal microscopy. The 3D section has a field of view of (x) 118.9 μm, (y) 118.9 μm, and depth (z) 26.8 μm. Signals associated with DAPI, WGA, and sarcomeric α-actinin labeling are shown in blue, yellow, and red respectively.

Movie IV. Three-dimensional reconstruction of AWM with epicardial layer removed. Signals associated with DAPI, WGA, and sarcomeric α-actinin labeling are shown in blue, yellow, and red respectively.

Movie V. Three-dimensional reconstruction of SAN. Reconstruction was performed from image stack acquired using conventional confocal microscopy with a field of view of (x) 118.9 μm, (y) 118.9 μm, and depth (z) 35.0 μm. Signals associated with DAPI, WGA, and sarcomeric α-actinin labeling are shown in blue, yellow, and red respectively.

Movie VI. Three-dimensional reconstruction of SAN with endocardial layer removed. Signals associated with DAPI, HCN4, and sarcomeric α-actinin labeling are shown in blue, green, and red respectively.

Movie VII. Three-dimensional reconstruction of AVN. Reconstruction was performed from image stack acquired using conventional confocal microscopy with a field of view of (x) 57.9 μm, (y) 57.9 μm, and depth (z) 28.4 μm. Signals associated with DAPI, WGA, and sarcomeric α-actinin labeling are shown in blue, yellow, and red respectively.

Movie VIII. Three-dimensional reconstruction of AVN with epicardial layer removed. Signals associated with DAPI, HCN4, and sarcomeric α-actinin labeling are shown in blue, green, and red respectively.

CHAPTER 3

LOCAL DYE DELIVERY OF FLUORESCENT DYE FOR FIBER-OPTICS CONFOCAL MICROSCOPY OF THE LIVING HEART

Huang C, Kaza AK, Hitchcock RW, Sachse FB. Local delivery of fluorescent dye for fiber-optics confocal microscopy of the living heart. *Front Physiol.* 2014;5:367. doi: 10.3389/fphys.2014.00367 © Owned by the authors, published by Frontiers, 2014.

frontiers in PHYSIOLOGY

ORIGINAL RESEARCH ARTICLE
published 25 September 2014
doi 10.3389/fphys.2014.00367

Local delivery of fluorescent dye for fiber-optics confocal microscopy of the living heart

*Chao Huang[1], Aditya K. Kaza[2], Robert W. Hitchcock[1] and Frank B. Sachse[1,3]**

[1] Department of Bioengineering, University of Utah, Salt Lake City, UT, USA
[2] Department of Cardiac Surgery, Boston Children's Hospital and Harvard Medical School, Boston, MA, USA
[3] Nora Eccles Harrison Cardiovascular Research and Training Institute, University of Utah, Salt Lake City, UT, USA

Edited by:
Gil Bub, University of Oxford, UK

Reviewed by:
Teun P. De Boer, University Medical Center Utrecht, Netherlands
Todd Joseph Herron, University of Michigan-Ann Arbor, USA

***Correspondence:**
Frank B. Sachse, Department of Bioengineering, Nora Eccles Harrison Cardiovascular Research and Training Institute, University of Utah, 95 S 2000 E, Salt Lake City, UT 84112, USA
e-mail: frank.sachse@utah.edu

Fiber-optics confocal microscopy (FCM) is an emerging imaging technology with various applications in basic research and clinical diagnosis. FCM allows for real-time *in situ* microscopy of tissue at sub-cellular scale. Recently FCM has been investigated for cardiac imaging, in particular, for discrimination of cardiac tissue during pediatric open-heart surgery. FCM relies on fluorescent dyes. The current clinical approach of dye delivery is based on systemic injection, which is associated with high dye consumption, and adverse clinical events. In this study, we investigated approaches for local dye delivery during FCM imaging based on dye carriers attached to the imaging probe. Using three-dimensional confocal microscopy, automated bench tests, and FCM imaging we quantitatively characterized dye release of carriers composed of open-pore foam only and foam loaded with agarose hydrogel. In addition, we compared local dye delivery with a model of systemic dye delivery in the isolated perfused rodent heart. We measured the signal-to-noise ratio (SNR) of images acquired in various regions of the heart. Our evaluations showed that foam-agarose dye carriers exhibited a prolonged dye release vs. foam-only carriers. Foam-agarose dye carriers allowed reliable imaging of 5–9 lines, which is comparable to 4–8 min of continuous dye release. Our study in the living heart revealed that the SNR of FCM images using local and systemic dye delivery is not different. However, we observed differences in the imaged tissue microstructure with the two approaches. Structural features characteristic of microvasculature were solely observed for systemic dye delivery. Our findings suggest that local dye delivery approach for FCM imaging constitutes an important alternative to systemic dye delivery. We suggest that the approach for local dye delivery will facilitate clinical translation of FCM, for instance, for FCM imaging during pediatric heart surgery.

Keywords: fiber-optics confocal microscopy, cardiac microscopy, fluorescent dyes, dye carrier, cardiac surgery

INTRODUCTION

Fiber-optics confocal microscopy (FCM) is based on confocal microscopy, which was invented and patented in the 1950s by Minsky (1961). Similarly to conventional confocal microscopy, FCM allows for high-resolution optical imaging at various depths within a specimen. With FCM, it is possible to visualize cellular and sub-cellular features within approximately 100 μm from a specimen's surface. In contrast to conventional confocal microscopic systems FCM systems comprise a coherent fiber-optic bundle with a length of up to several meters. In many implementations, an imaging microprobe including a lens is located at the tip of the fiber-optic bundle. The detachment of the imaging microprobe from other components of the imaging system allows *in situ* imaging of organs and tissues within a body, which cannot be performed with conventional microscopy. In the last years, the unique capability of real-time, *in situ* microscopic imaging has led to development of FCM-based approaches for clinical diagnosis in gastrointestinology (Inoue et al., 2005; Kiesslich and Neurath, 2005; Goetz et al., 2006; Anandasabapathy, 2008), pulmonology (Thiberville et al., 2009; Salaun et al., 2013), and urology (Wu et al., 2011).

Recently, we introduced FCM for imaging of the living heart and developed approaches for tissue discrimination during cardiac interventions (Lasher et al., 2009; Huang et al., 2013). In particular, we proposed application of FCM during pediatric open-heart surgery for repair of congenital heart defects. Injury to specialized tissue of the conduction system is a major risk in surgical repair of congenital heart defects. In order to avoid damaging the conduction system, surgeons rely on an empirical approach and guidelines developed from gross anatomical studies to approximate the disposition of the conduction system. However, the distribution of the conduction system can vary individually and with the complexity of the heart defect (Anderson et al., 1983; Andersen et al., 2006). Our previous studies indicate feasibility of intraoperative discrimination of cardiac tissue using FCM, which will reduce the risk of injury to the specialized tissue of the conduction system (Huang et al., 2013). In these studies we investigated sinoatrial and atrioventricular node tissue as well

as atrial working myocardium. Tissue discrimination was performed based on microstructural features characteristic of these tissue types and immunohistochemical markers.

A major challenge in applying FCM for intraoperative microscopic imaging is the reliance of the technology on fluorescent labeling. FCM illuminates fluorescent molecules within the imaged specimen using a light source, commonly at a wavelength 488 or 633 nm. The light is absorbed by fluorescent molecules, which in turn emit light at a longer wavelength. This emitted light is collected through the fiber-optic bundle and visualized by the FCM system. Generally, intrinsic fluorescence in biological specimens is low and labeling of specimens with fluorescent dyes is required for imaging. The common approach for dye delivery in clinical applications of FCM is systemic injection of fluorescent dye at high concentrations. In addition to high dye consumption, there have been also some concerns of patient safety. For example, the incidence of adverse reactions following intravenous administration of fluorescein is 1.1–4.8% (Kwiterovich et al., 1991; Kwan et al., 2006) for retinal fluorescein angiography and 1.4% for gastrointestinal endoscopic imaging (Wallace et al., 2010). In these studies, adverse reactions including dizziness, nausea, vomiting, and transient hypotension have been reported. However, there were no serious adverse reactions or deaths. We suggest that a more localized dye delivery approach may serve as an alternative (Lasher et al., 2009) and be well suited for intraoperative imaging applications such as in pediatric open-heart surgery or various other surgical disciplines (Sachse et al., 2011, 2013).

In this study, we implemented and evaluated approaches for delivery of fluorescent dye during FCM imaging in the living heart. In particular, we compared approaches of local dye delivery with a model of systemic dye delivery. For this purpose, we investigated dye release characteristics and quality of images produced using several local dye delivery methods and fluorescent dyes. These local dye delivery methods were based on dye carriers assembled from medical grade foam and agarose hydrogel. The dye carriers were attached to the tip of the FCM imaging microprobe in such a manner that placement of the assembly onto the surface of a specimen resulted in continuous release of fluorescent dye from the carrier to the specimen throughout the image acquisition. Using three-dimensional confocal microscopy, automated bench tests, and FCM, we quantitatively identified carriers with release characteristics suitable for intraoperative imaging. Local dye delivery using dye carriers was subsequently compared with a model of systemic dye delivery in isolated perfused heart of a small mammal based on FCM imaging and different fluorescent dyes. The isolated hearts were arrested to reproduce cardioplegia in open-heart surgery. Two-dimensional image sequences were acquired with FCM from the ventricular and atrial subepicardial myocardium as well as the sinoatrial node region. We assessed image quality based on analysis of signal-to-noise ratio from FCM images acquired in these regions of the heart using both dye delivery approaches.

MATERIALS AND METHODS

DYE CARRIER MATERIAL AND FABRICATION

Several types of dye carriers were fabricated from polyester polyurethane foam with a density of 27.7–33.0 kg/m^3 and 31.5–39.4 pores/cm (FLTZ90D; Foamex Innovations Inc., Ft. Wayne, IN, US). The foam material was reticulated so that pores within the material are open and interconnected. The fabrication of the dye carrier involved boring the inner channel and main body of foam cylinders using biopsy punches with 2 and 6 mm diameter (BP99; HealthLink, Jacksonville, FL, US), respectively, from stock 15 by 15 by 1.2 cm foam sheets. For some dye carriers the foam cylinders were loaded with agarose gel. The gel was made by mixing agarose powder (GeneMate LE Agarose; BioExpress, Kaysville, UT) in distilled water to concentrations of 1, 3, or 5%. The agarose powder in solution was dissolved for 15 min at 75–80°C with continuous magnetic stirring. Immediately following dissolution, the agarose solution was filled into Eppendorff tubes (1.5 ml). Foam cylinders were immersed in the gel and compressed with forceps for 1 min to remove air bubbles. The gel was cured at room temperature for 15 min followed by overnight incubation at 4°C. The following day, excess agarose gel within the inner channel and encapsulating the foam-agarose cylinders were removed. Foam-only and foam-agarose carriers containing 1, 3, and 5% agarose gel were cut from the cylinders with a razor blade to a height of 4 mm.

DYE CARRIER AND DYE PREPARATION

Foam-only carriers were repetitively compressed for 1 min in distilled water containing 10 kDa dextran conjugated Alexa Fluor 488 (Invitrogen, Carlsbad, CA, US) at a 125 μg/ml concentration followed by immersion in the dye solution for at least 15 min prior to imaging. Foam-agarose carriers were similarly immersed for 15 min, but without compression, in distilled water containing dextran or fluorescein sodium [Fluorescite® (fluorescein injection, USP) 10%; Alcon, Fort Worth, TX, US; 1:1000]. For living arrested heart preparations, foam-agarose carriers were immersed for 15 min in oxygenated, high-K/low-Ca Tyrode's solution (in mmol/L: 92 NaCl, 11 dextrose, 13.2 KCl, 5 $MgCl_2$, 24 HEPES, 20 taurine, 5 creatine, 5 $C_3H_3NaO_3$, 1 NaH_2PO4, 0.25 $CaCl_2$; pH 7.4; ≈10°C) containing fluorescein sodium (1:1000). For experiments involving dye perfusion in the living arrested heart, a perfusate of oxygenated, high-K/low-Ca Tyrode's solution containing fluorescein sodium (1:50000) was prepared.

FCM IMAGING

Two-dimensional image sequences of synthetic tissue and preparations of living cardiac tissue were acquired with a FCM system (FCM 1000; Leica Microsystems GmbH, Wetzlar, Germany) equipped with a custom fiber-optics microprobe (UltraMiniOWD30; Mauna Kea Technologies, Paris, France). The resolution was 1.9–2.4 μm in x- and y-direction and approximately 10 μm in z-direction. The field of view (xy) was 186 by 130 μm at a depth (z) of approximately 26 μm. The frame rate was 12 Hz.

EVALUATION OF DYE RELEASE

In a first set of experiments, we performed weight measurements on foam-only carriers ($n = 3$) and foam-agarose carriers with 1, 3, and 5% agarose concentrations ($n = 3$ for each concentration). Carriers of these types were weighed (BP211D, Sartorius, Elk Grove, IL, USA) before and after loading with dextran-Alexa 488. In another set of experiments, the same types of carriers

were loaded with dextran-Alexa 488 or fluorescein sodium solution and subjected to cyclic line tests to evaluate dye release. In short, loaded dye carriers were assembled on the fiber-optics microprobe so that the probe tip was flush with the carrier (**Figures 1A,B**). The assembled probe with dye carrier was then attached to a motorized micro-manipulator (MP285; Sutter Instrument, Novato, CA, US) allowing for programmed movements in three-dimensional space at high resolution. A testbed attached to a manual manipulator (World Precision Instruments, Inc., Sarasota, FL, US) was placed underneath the microprobe. Samples of moisturized synthetic tissue analog (VWR, West Chester, PA, US) composed of 100% virgin wood fiber were affixed to the testbed and brought into focus underneath the imaging probe at the correct focal depth using the manual manipulator. Immediately following, programmed movement of probe across the surface of the sample was initiated. Specifically, the micro-manipulator was programmed to contact the microprobe with attached dye carrier to the surface of the sample, move the probe 5 mm across the surface along a linear path at a speed of 100 μm/s, remove the probe from the sample, and return the probe to the original starting position. A schematic of the cyclic line test is shown in **Figure 1C**. Loaded dye carriers were subjected to a continuous cycle of line tests with a fresh synthetic tissue sample being presented after each line. 2D image sequences of each line were recorded until image quality became severely reduced.

Microscopic imaging of dye carriers

In some experiments, carriers loaded with fluorescent dye and subjected to a cyclic line test were imaged using a laser scanning confocal microscope (Zeiss LSM 5 Duo; Zeiss, Jena, Germany) equipped with a 2.5× lens with a numerical aperture of 0.12. Fluorophores within the carriers were excited with a 488 nm wavelength laser and 3D image stacks were acquired at a spatial resolution of 10 × 10 × 20 μm in x-, y-, and z-direction, field of view (xy) of 5.1 by 5.1 mm, and depth (z) up to 500 μm. Cross-sections through the surface of different carriers were compared.

Quantitative analysis of dye release in bench tests

The dye release characteristic of different dye carriers was analyzed using the 2D image sequences of synthetic tissues. For this purpose, the image sequences were converted using MATLAB (MathWorks, Natick, MA, US). The average and standard deviation of the intensity for each image within a line was determined and averaged across the whole line. The average intensities for each line in a cyclic line test are denoted as $I_{lines} = \{I_1, I_2, \ldots, I_n\}$ with the last line of a given cyclic line test n. I_{lines} was then smoothed using a central moving average of 1 line. In addition, the sample mode I_{mode} and standard deviation I_{std} of the background were calculated for each cyclic line test based on an image acquired in air at the end of each test. I_{mode} was determined from the maximum in the image histogram. The threshold intensity, I_{thresh}, for each cyclic line test was then calculated:

$$I_{thresh} = I_{mode} + \gamma I_{std}.$$

We chose $\gamma = 10$ based on visual inspection of a subset of image sequences. We found that images with γ greater than 10 exhibited clearly identifiable microstructures that were not identifiable in images with γ below this value. I_{thresh} was used to quantitatively assess image quality. The number of lines L_{thresh} that were drawn before I_{lines} of a cyclic line test reached I_{thresh} was used to evaluate dye release of various dye carriers and solutions. **Table 1** shows sample sizes for the dye carriers and solutions evaluated.

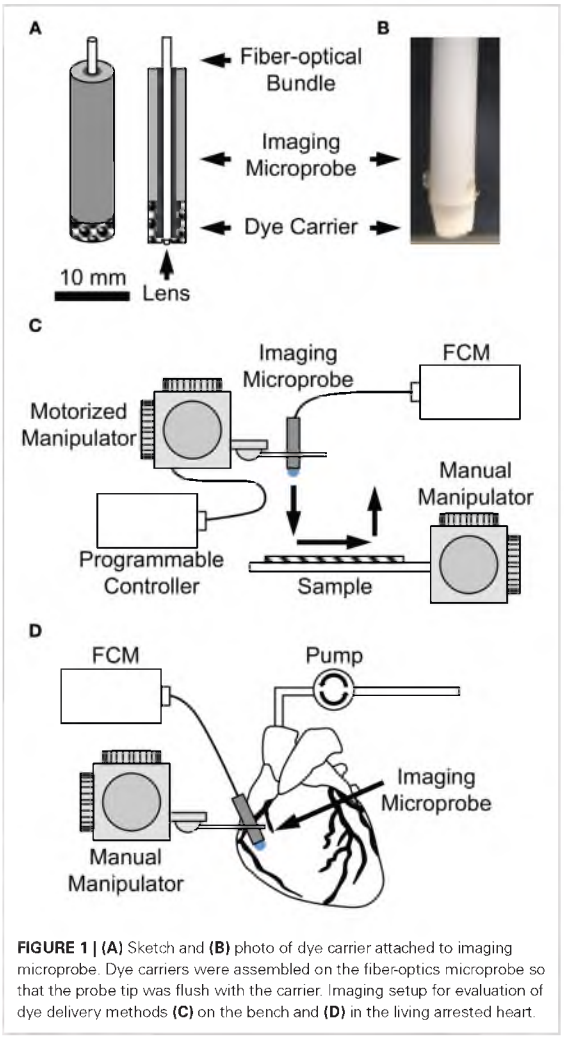

FIGURE 1 | (A) Sketch and **(B)** photo of dye carrier attached to imaging microprobe. Dye carriers were assembled on the fiber-optics microprobe so that the probe tip was flush with the carrier. Imaging setup for evaluation of dye delivery methods **(C)** on the bench and **(D)** in the living arrested heart.

EVALUATION OF DYE DELIVERY APPROACHES IN THE LIVING HEART

All procedures were approved by the University of Utah Institutional Animal Care and Use Committee and followed the guidelines of the National Institutes of Health Guide for the Care and Use of Laboratory Animals. Sprague-Dawley rats of approximately 300 g body weight were anesthetized with pentobarbital (40 mg/kg) and anticoagulated with heparin (500 IU/kg). Following anesthesia, the hearts were rapidly excised and continuously Langendorff-perfused (Langendorff,

1895) with oxygenated, high-K/low-Ca Tyrode's solution at a flow rate of 10–15 mL/min.

Two methods of dye delivery were subsequently evaluated. The first method was based on delivery of dye via perfusion of the Langendorff heart preparation as a model of systemic dye delivery. In short, perfusion was switched after 5 min to Tyrode's solution containing fluorescein sodium. Immediately following, 2D image sequences of ventricular and atrial subepicardial myocardium and of the sinoatrial node region were acquired. The second method was based on the dye carriers described above. The heart was continuously Langendorff-perfused with Tyrode's solution. Image sequences of the above-mentioned regions were acquired using an imaging microprobe with attached foam-agarose carrier of 1% agarose concentration loaded with fluorescein sodium (**Figure 1D**).

Processing and visualization of images

2D images sequences were converted using MATLAB. Images auto-adjusted for brightness and contrast using the imadjust function in MATLAB.

Quantitative analysis of dye delivery approaches

The signal-to-noise ratio (SNR) was calculated from image sequences acquired of various tissue regions using both dye delivery approaches: dye carrier and perfusion. In general, SNR is defined as μ/σ where μ is the mean of the signal and σ is an estimate of the standard deviation of the noise. In this study, a region of high and low signal was selected from each image. Each region comprised approximately 1000 pixels and corresponded to an area of signal or background. The mean intensity within these areas of signal and background was calculated and denoted as I_{sig} and I_{bg}, respectively. In addition, the standard deviation within the background region I_{std} was determined. The SNR for each image was calculated as:

$$SNR = (I_{sig} - I_{bg})/I_{std}$$

The SNR was used to evaluate dye delivery based on dye carrier and perfusion approaches in various tissue regions.

IMAGING OF MICROVASCULATURE IN THE LIVING HEART

Two-dimensional image sequences in an arrested Langendorff-perfused rat heart labeled with high molecular weight dextran conjugate in perfusate were acquired using FCM. In short, a perfusate of oxygenated, high-K/low-Ca Tyrode's solution containing 2 MDa dextran conjugated to fluorescein (Invitrogen) at a concentration of 40 μg/mL was prepared. For full dissolution of the dextran-conjugate, the perfusate was vortexed for 5 min followed by sonication (Model 150V/T Ultrasonic Homogenizer; Biologics Inc., Cary, NC, US) at 50% power with a pulse width and pulse duration of 1 s and 2 s respectively for 5 min. Immediately following, the perfusate was centrifuged (Allegra X-22; Beckman Coulter, Indianapolis, IN, US) for 5 min at 6000 *g* and then passed through a 0.22 μm syringe filter (Millex-GP; Millipore, Billerica, MA, US). Images from the right ventricular and atrial regions in the living heart were acquired using the perfusion method of dye delivery as previously described.

Table 1 | Number of Cyclic Line Tests Performed for Evaluation of Dye Release.

Fluorescent dye	Carrier		
	1%	3%	5%
Dextran-Alexa 488	11	8	9
Fluorescein sodium	10	8	9

STATISTICAL ANALYSIS

Statistical data are presented as mean ± s.e.m. Statistical significance was assessed by One-Way analysis of variance (ANOVA) followed by *post-hoc* Tukey–Kramer considering a significance level of 0.01.

RESULTS

EVALUATION OF DYE RELEASE IN BENCH TESTS

In a first set of experiments, we explored structural and functional properties of foam-only and foam-agarose carriers using weight measurements laser scanning confocal microscopy, and cyclic line tests. Our aim was to identify dye carriers, which maintain a high volume of dye retention and prolonged rate of dye release during cyclic line tests.

We weighed foam-only and foam-agarose carriers of 1, 3, and 5% agarose concentration before and after immersion in dextran-Alexa 488. Statistical analysis of the measured weights is presented in **Figure 2**. The weight of the foam-only carrier increased from 2.52 ± 0.03 to 89.00 ± 0.79 mg after loading of dextran, an approximately 34-fold increase in weight. In general, the variation in the weight of the foam-only and foam-agarose carriers after loading of dextran-Alexa 488 was small with weights ranging from approximately 87–103 mg.

We then acquired 3D image stacks of the distal end of foam-only and foam-agarose carriers with 1% agarose concentration loaded with dextran-Alexa 488. Cross-sections through those stacks are shown in **Figures 3A,B**, respectively. The cross-sections

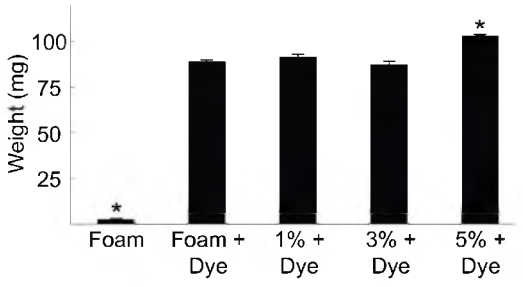

FIGURE 2 | Weights of various foam-only and foam-agarose carriers before and after loading of dextran-Alexa 488. Foam-only carriers exhibited a 34-fold increase in weight after dextran-Alexa 488 was loaded. We observed only small differences in the weight of various foam-only and foam-agarose carriers after loading of dextran-Alexa 488. (* $P < 0.01$, significant difference vs. all other groups, One-Way ANOVA with *post-hoc* Tukey–Kramer).

illustrate the porous and reticulated microstructure of the foam material, which has highly variable pore sizes in the sub-millimeter scale. Dye distribution was homogeneous in the interior of the foam. The agarose gel did not appear to affect the structural properties of the carriers as both the foam-only and 1% foam-agarose carrier exhibited similar microstructural characteristics and fluorescence intensities.

We further subjected the foam-only and 1% foam-agarose carrier to cyclic line tests to characterize dye release. The fluorescent signal was greatly reduced in the foam-only carrier after only one line (**Figures 3C** vs. **3A**). Only small regions with dye remained, strongly suggesting that most of the dye was transferred to the synthetic tissue. The fluorescent intensity within the 1% foam-agarose carrier, however, was partially maintained even after seven lines of a cyclic line test (**Figures 3D** vs. **3B**). Clearly, the foam-only and 1% foam-agarose carrier exhibited different release properties. The dye release was dramatically slowed for the foam-agarose carrier as compared to the foam-only carrier after cyclic line test. Foam-only carriers exhibited a severe intensity decrease after the first line of a cyclic line test, which makes them unsuitable for applications such as cardiac surgery requiring several minutes of dye release. Based on this finding we excluded foam-only carriers from further assessment.

We further characterized the functional properties of foam-agarose carriers and fluorescent dyes with the cyclic line tests. We acquired FCM image sequences of synthetic tissue using foam-agarose carriers with 1, 3, and 5% agarose concentrations loaded with either dextran-Alexa 488 or fluorescein sodium (**Table 1**). **Figure 4A** presents FCM images from an example cyclic line test of a 1% agarose carrier loaded with dextran-Alexa 488. **Figure 4B** shows the average and standard deviation of intensities for each line of the example test in **Figure 4A**. In this example, the average intensity of each line gradually decreased from 862.4 ± 95.9 arbitrary units (AU) to 49.9 ± 16.3 AU from line 1 to line 8, respectively. The decrease of average intensity was approximately exponential. An L_{thresh} of 5 lines was determined from an I_{thresh} of 207.3 AU. Features of the imaged sample were still discernable at line 5 with a measured average intensity and standard deviation of 257.3 ± 67.3 AU (**Figure 4A**).

Statistical analyses of L_{thresh} from cyclic line tests are presented in **Figure 4C**. In general, the foam-agarose carriers exhibited similar dye release properties allowing for 5–9 lines before a decrease of signal intensity beyond I_{thresh}. An exception was the 3% carrier loaded with fluorescein sodium, which allowed for 17.9 ±

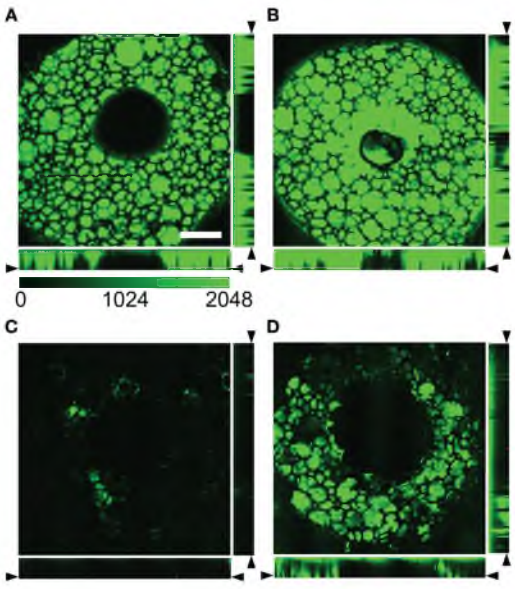

FIGURE 3 | Cross-sections through image stacks acquired with laser scanning confocal microscopy of (A,B) foam-only and (C,D) 1% foam-agarose carrier loaded with dextran-Alexa 488. Foam-only and 1% foam-agarose carrier **(A,C)** before and after **(B)** one and **(D)** seven lines, respectively. Dye is almost completely released after a single line in the foam-only carrier. Scale: 1 mm. (Images modified from Sachse et al., 2013).

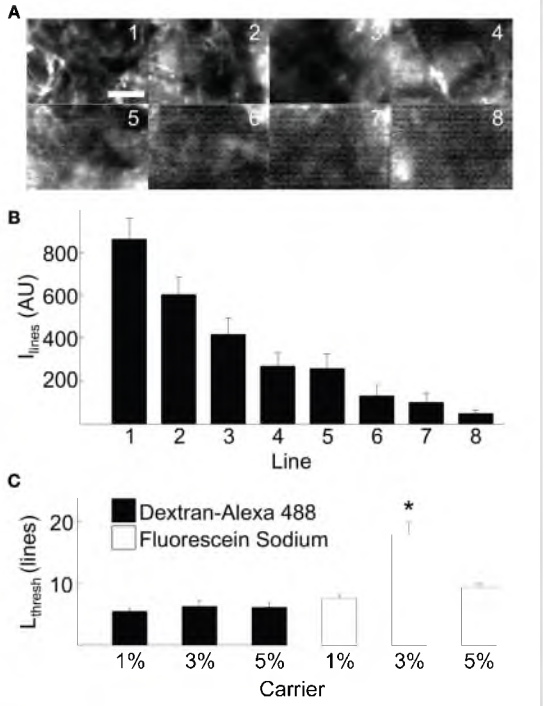

FIGURE 4 | Experimental evaluation of dye release from carrier on the bench. (A) Example FCM images from cyclic line test on a 1% foam-agarose carrier loaded with dextran-Alexa 488 showing decreasing SNR. Scale: 50 μm. **(B)** Mean and standard deviation of intensities for lines 1–8 in **(A)**. An $L_{thresh} = 5$ was determined from $I_{thresh} = 207.3$ AU for the cyclic line test. **(C)** Statistical analysis of dye release of various foam-agarose carriers and fluorescent dyes. The 3% carrier loaded with fluorescein sodium was observed to produce 2–3 times higher L_{thresh} than any other combination of carrier or dye. (* $P < 0.01$, significant difference vs. all other groups, One-Way ANOVA with *post-hoc* Tukey–Kramer).

2.0 lines before signal decrease. In all but this case, differences in L_{thresh} were not significant between any other combination of foam-agarose carriers and fluorescent dye.

EVALUATION OF DYE DELIVERY APPROACHES IN THE LIVING HEART

In further experiments, we evaluated two methods of dye delivery in the living arrested heart. **Figure 5** presents exemplary images acquired with the FCM from different regions in the heart after administration of fluorescein sodium via perfusion (**Figures 5A–C**) and 1% foam-agarose carrier (**Figures 5D–F**). Dark regions in these images suggest absence of fluorescence in intracellular spaces while the bright regions indicate presence of fluorescence within the extracellular space. A regular arrangement of intensities in the FCM images was visible in the right ventricular (**Figures 5A,D**) and right atrial (**Figures 5B,E**) regions. These images indicate working myocardium comprised of aligned myocytes. An irregular arrangement as seen in the sinoatrial node (**Figures 5C,F**) is a hallmark of reticular-arranged nodal cells (Huang et al., 2013). The microstructural arrangement in the working myocardium and in the sinoatrial node did not differ with respect to the method of dye delivery. However, images acquired using the perfusion method of dye delivery presented structural features of the microvascular bed in the working myocardium, including branching and transverse components (**Figures 5A,B**). These features were a frequent occurrence in the acquired movie sequences of the working myocardium following this delivery method (Videos 1, 2 in Supplementary Material). The microvascular components were not present in images acquired of the working myocardium using dye delivery via carrier (**Figures 5D,E**; Videos 4, 5 in Supplementary Material). Furthermore, microvascular features were not apparent in the images acquired from the sinoatrial node respective of the dye delivery approach (**Figures 5C** vs. **5F**; Videos 3, 6 in Supplementary Material).

We further explored imaging of the microvasculature in living heart experiments involving perfusion of 2 MDa dextran conjugated to fluorescein. Previous studies demonstrated that dextran conjugates greater than 40 KDa do not diffuse through either the endocardial endothelium or capillary endothelium in rat (Andries and Brutsaert, 1994) suggesting that this label provides reliable visualization of the microvasculature. **Figure 6** presents exemplary FCM images of the microvasculature bed labeled with 2 MDa dextran-conjugate. The images present branching and transversal components similarly as observed in images of right ventricular (**Figures 6A** vs. **5A**; Video 7 in Supplementary Material) and atrial working myocardium (**Figures 6B** vs. **5B**; Video 8 in Supplementary Material) perfused with fluorescein sodium.

We quantitatively characterized the dye release of the evaluated dye delivery methods based on SNR (**Table 2**). **Figure 7** presents statistical analysis of SNR from the previously acquired images

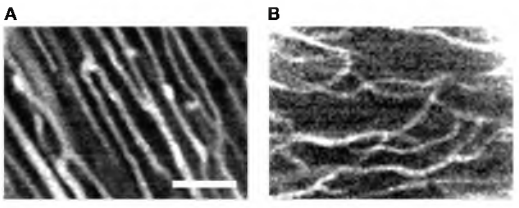

FIGURE 6 | Exemplary FCM images acquired of the living arrested heart after administration of high molecular weight dextran-conjugated fluorescein via perfusion. The high molecular weight dextran-conjugate allowed for direct visualization of vasculature within the **(A)** right ventricular and **(B)** right atrial subepicardial myocardium. Microvasculature features of transverse and branching components are apparent. Scale: 50 μm.

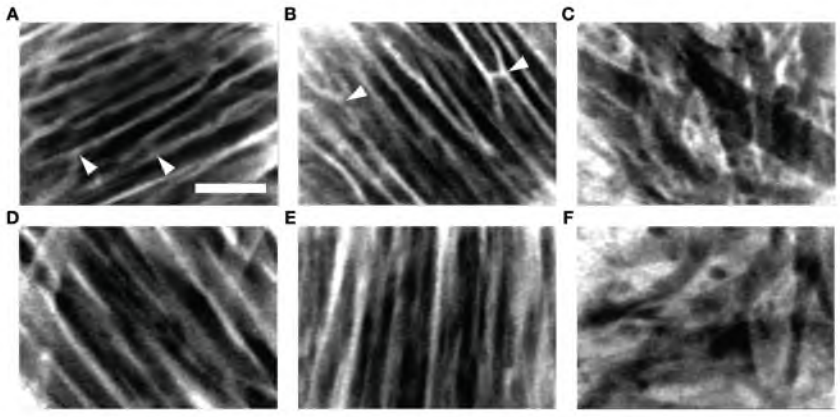

FIGURE 5 | Exemplary FCM image sequences acquired of the living arrested heart after administration of fluorescein sodium via (A–C) perfusion and (D–F) 1% foam-agarose dye carrier. Images acquired following perfusion of fluorescein sodium in the **(A)** right ventricular and **(B)** right atrial subepicardial working myocardium displayed branching and transverse structures (arrowheads) characteristic of the microvascular bed. Structures of the microvascular bed were absent in images acquired of the **(D)** right ventricular and **(E)** right atrial subepicardial working myocardium following topical administration of fluorescein sodium via dye carrier. **(C,F)** Images acquired from the sinoatrial node region were also absent of microvascular structures respective of the dye delivery method. Scale: 50 μm.

Table 2 | Number of Images and Animals Used for Signal-to-Noise Ratio Analysis.

Dye delivery	Images/animals		
	RV	RA	SN
Perfusion	151/7	165/8	100/6
Carrier	74/6	53/5	55/6

RV, indicates right ventricle; RA, right atrium; SN, sinoatrial node.

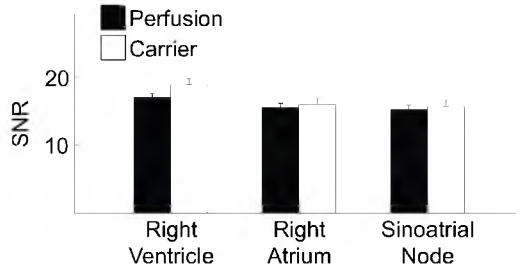

FIGURE 7 | Statistical characterization of FCM images from right ventricle, right atrium and sinoatrial node regions. Differences in the SNR were not significant, respective of the dye delivery method (perfusion vs. carrier) or tissue region. (* $P < 0.01$, One-Way ANOVA with *post-hoc* Tukey–Kramer).

in the living heart following dye carrier or perfusion dye delivery. The measured SNRs were in the range of 15–19. Differences in the SNR were not significant, respective of the dye delivery method or tissue region.

DISCUSSION

FCM has emerged as a tool for basic biomedical research (Bharali et al., 2005; Vincent et al., 2006; Lewandowski et al., 2010) and clinical applications. Current clinical applications of FCM include imaging and diagnosis of the microstructure of tissues in gastrointestinal, respiratory, and urinary tracts. We recently proposed FCM for intraoperative tissue discrimination during cardiac interventions (Huang et al., 2013), in particular, for pediatric open-heart surgery. In these cardiac interventions and many other clinical applications FCM imaging relies on intravenous injection of high-dose fluorescein sodium as a fluorescent marker. While concerns for patient safety associated with this approach for delivery of fluorescent dye are minor, we believe that alternative reliable methods for dye delivery can be introduced.

Here we developed and evaluated local dye delivery as an approach for FCM imaging in the living heart. We demonstrated that a foam-agarose dye carrier comprised of porous foam and agarose hydrogel reliably delivers fluorescent dye in sufficient concentration for FCM. Our evaluations showed that foam-agarose dye carriers exhibit a prolonged dye release compared to foam-only carriers. A probable cause is the dense cross-linked network of agar strands within the foam pores, which impede diffusion of dye inside and out of the carrier.

Diffusion of molecules, solutes, and particles in agarose gels has been extensively studied (Johnson et al., 1996; Pluen et al., 1999; Fatin-Rouge et al., 2004). Based on those studies, we expected differences of diffusion and dye release due to differences in the Stokes radius of fluorophores. We also expected differences of dye release due to differences in the agarose concentration. However, dye release was in general not affected by agarose concentration between 1 and 5% and the type of dye. We found only a single combination of agarose concentration and dye exhibiting prolonged dye release (**Figure 4C**). While we cannot explain this prolonged release, our finding suggests that dye release properties can be optimized for specific dyes.

Cyclic line tests on synthetic tissue analogs demonstrated that foam-agarose dye carriers allowed for reliable imaging of at least 5–9 lines and in the case of the 3% carrier loaded with fluorescein sodium up to 18 lines. Based on the fact that scan times for each line of a cyclic line test was 50 s, we estimate that the foam-agarose carriers allows for continuous dye release of up to 15 min for the 3% carrier loaded with fluorescein sodium and between 4 and 8 min for the other foam-agarose carriers. We expect that dye release over these durations will be sufficient for many clinical applications, when one considers practical limitations of the length of surgical interventions. For applications of FCM in cardiac interventions, we expect that the imaging window can be up to minutes in order to reduce burden on patients where time on cardiopulmonary bypass is of crucial importance.

Becker et al. investigated the optimal time window for FCM imaging of the upper gastrointestinal tract in a porcine model following intravenous injection of fluorescein sodium (Becker et al., 2008). The study revealed that contrast and image quality was high between 1 and 8 min after injection of fluorescein sodium. The results of our cyclic line tests suggest that local dye delivery based on foam-agarose carriers produces imaging windows of similar duration. An advantage of the dye carrier over systemic injection is that the FCM imaging can start instantaneously without delays. In contrast, the transit times of fluorescein sodium from initial injection to detectable fluorescence was reported to be 10–20 s for retinal fluorescein angiography (Duane et al., 1991; Eskridge et al., 1991) and 30 s for gastrointestinal endoscopic imaging (Becker et al., 2008).

Our study revealed that the SNR of images acquired from the living heart following both local and perfusion delivery of fluorescent dyes are not different. In addition, the observed SNRs were comparable to the SNRs of 10–20 reported in studies involving FCM imaging of the human gastrointestinal tract with intravenous fluorescein sodium (Shahid et al., 2011). This further suggests that local dye delivery approaches for FCM produce images of similar quality to that of systemic delivery. However, an important difference between local and systemic dye delivery was related to the imaged tissue microstructure. We observed that the perfusion method of dye delivery presented structural features characteristic of microvasculature in images acquired from working myocardium (Brown, 1965; Chilingaryan et al., 2014). These features were not observed in images acquired following local dye delivery. Also, these structures were not visible within the sinoatrial node region for both methods of dye delivery. We hypothesize that the differences in the images of tissue

microstructure are explained by differences of dye transport to the imaged region. In the perfusion method of delivery dye is transported through coronary vessels and microcirculation of the Langendorff-perfused heart. Therefore, we expect a diffusion gradient with the highest and lowest concentrations of dye within the microvasculature and intracellular space, respectively. In addition, fluorescein predominantly stays in the vessels as 70–80% of it is bound to plasma albumin. Only a small portion of fluorescein, i.e., unbound fluorescein, eventually leaks into the tissue interstitium and allows for visualization of cellular morphology (Becker et al., 2008). Our imaging studies using a high molecular weight dextran-conjugated fluorophore as perfusate supported this hypothesis. The high molecular weight dextran-conjugate selectively labeled the microcirculation identified by branching and transversal components within the tissue (**Figure 6**). Thus, images of working myocardium following systemic application of fluorescein sodium appear to be a superposition of fluorescent signal from the microcirculation and extravascular space. In contrast to the perfusion method of dye delivery, local dye delivery in the heart relies on diffusion of dye through the epicardium or endocardium into the sub-epicardial or sub-endocardial myocardium. The highest concentration of dye in the tissue is within the interstitial space. Dye that diffuses into the vasculature is quickly removed from the labeled region, which leads to absence of vascular signals. Our findings suggest that the type of microstructural features to be visualized with FCM should determine the approach for dye delivery. For instance, discrimination of cardiac tissue types during open-heart surgery requires visualization of the microstructural arrangement of cellular features. In this case, the local dye delivery approach appears more appropriate, because images are less affected by the distribution of microvasculature. If the application is characterization of microvascular features then systemic application of the appropriate fluorescent dye is preferred. Our findings also suggest that the degree of vascularization within the imaged region may limit systemic delivery approaches for FCM. For instance, scarred regions in infarcted or fibrotic hearts are known to be poorly perfused (Kim et al., 1996; Saeed et al., 2006). Thus, a local dye application may be more suitable for visualization of myocardial scars.

Our studies revealed major differences in the dose of fluorescein sodium required for reliable FCM imaging in the living heart using the two dye delivery approaches. The typical dose for intravenous administration of fluorescein sodium is either 200 or 500 mg at a concentration of 100 mg/mL. In recent years, it has been reported that the 500 mg dose produces superior images to that of the 200 mg dose in both retinal fluorescein angiography (Moosbrugger and Sheidow, 2008) and gastrointestinal endoscopic imaging (Shahid et al., 2011) studies. Based on weight measurements we estimate that a fully loaded dye carrier can hold approximately 4.1 μg of fluorescein sodium. In contrast, our model of systemic delivery required perfusion of the heart with approximately 30 μg/min. The comparison indicates that local dye delivery requires significantly less dye than systemic delivery. We suggest that local dye delivery is in particular suitable for clinical applications such as pediatric open-heart surgery where microdosing will mitigate potential safety concerns.

In a previous study, we introduced a dye carrier based on hydrogel indicating feasibly of local dye delivery (Lasher et al., 2009; Sachse et al., 2011). This dye carrier comprised a hollow hydrogel cylinder serving as dye reservoir and a thin layer of transparent hydrogel directly in front of the microprobe allowing for diffusion of dye into the tissue. The dye carrier necessitated an imaging microprobe with a large focal depth to accommodate for the addition of hydrogel in front of the lens. Also, this carrier required precise fabrication of the hydrogel layer at micro-meter scale. Furthermore, the precise attachment of the hydrogel at the microprobe tip and the overall fragility of hydrogel complicated handling. In comparison, fabricating the presented foam-agarose dye carrier is simple and does not require precision at micrometer scale. The foam-agarose dye carrier was designed for lateral attachment to the imaging probe and does not occupy space in front of the microprobe. The combination of foam with hydrogel also improved the mechanical stability of the dye carrier.

Many limitations of FCM are related to technological and physical barriers of conventional confocal microscopy. An overview of limitations of confocal microscopy can be found, for instance, in Bolte and Cordelieres (2006). One limitation of confocal microscopy is that only regions close to the surface of the tissue can be imaged. This is an inherent problem of optical microscopy related to absorption and scatter of light by biological tissue. Using current FCM systems we expect that imaging of tissue will be possible to a depth of 100 μm, which appears sufficient to gain important research and diagnostic information. The spatial resolution of current FCM systems is smaller than the resolution of high-end conventional confocal microscopes, having for instance, oil immersion lenses with a high numerical aperture. The low resolution of current FCM systems makes it difficult to identify cell ends or the subcellular micro-structure mentioned above. However, the presented image data (**Figure 5**) suggest that important features of cardiac tissue can be identified, for instance, related to the regularity of the distribution of the labeled extracellular and vascular space.

Certain limitations are associated with using Langendorff perfusion of fluorescent dye in Tyrode's solution as a model of systemic dye delivery. Intravenous injection applies a bolus for fluorescent dye into the systemic circulation. The dose that each organ or tissue receives and how long the dye remains in the different regions varies. Our simple model of systemic dye delivery was based on observed fluorescent intensities. We chose a concentration and flow rate necessary to reconstruct intensities from previous studies (Huang et al., 2013). An option for future studies is to perform those in the anesthetized animal after thoracotomy. While we expect that higher dye concentrations for systemic delivery will be required due the binding of fluorescein to plasma albumin (Becker et al., 2008), we do not anticipate that changes in the concentration of dye in the foam-agarose carrier are necessary for imaging of cardiac tissues.

In our study we were not able to identify vasculature within the sinoatrial node region, which is in contrast to previous reports that the sinoatrial node has a rich intramural network of anastomosing blood vessels and that the density of the microvasculature in the node is greater than in adjacent atrial tissue (Ovcina and Cemerlic, 1997). A possible explanation is the focal depth of the

applied probe (approximately 26 μm). It is possible that vasculature in the sinoatrial node resides in the depth of the atrial wall that is not accessible with this imaging probe. It is also possible that visualization of the dense and complex network of the microvasculature is difficult in context of the dense and irregular cellular arrangement found within this nodal region.

In conclusion, our studies demonstrate that the introduced local dye delivery approach for FCM imaging constitutes an important alternative to commonly applied systemic approaches of dye delivery. We suggest that the approach for local dye delivery will facilitate clinical translation, for instance, for FCM imaging during pediatric heart surgery. Furthermore, we believe that the foam-agarose dye carrier and methodology for evaluation of dye release have significant applications in local delivery of other fluorophores and development of further types of dye carriers.

AUTHOR CONTRIBUTIONS

Substantial contributions to the conception or design of the work; or the acquisition, analysis, or interpretation of data for the work: Robert W. Hitchcock, Chao Huang, Aditya K. Kaza, Frank B. Sachse. Drafting the work or revising it critically for important intellectual content: Robert W. Hitchcock, Chao Huang, Aditya K. Kaza, Frank B. Sachse. Final approval: Robert W. Hitchcock, Chao Huang, Aditya K. Kaza, Frank B. Sachse. Agreement to be accountable for all aspects of the work in ensuring that questions related to the accuracy or integrity of any part of the work are appropriately investigated and resolved: Robert W. Hitchcock, Chao Huang, Aditya K. Kaza, Frank B. Sachse.

ACKNOWLEDGMENT

This research was supported by the US National Institutes of Health (R21 HL108099), the Nora Eccles Treadwell Foundation, and the Utah Science Technology and Research initiative. The authors are thankful for constructive discussions with Dr. F. Lacombe, Dr. T. Vercauteren, and C. Tihansky (Mauna Kea Technologies, Paris, France). We acknowledge valuable contributions of Mr. Nghi T. Tran and Ms. Chelsea M. Mitchell to data acquisition.

SUPPLEMENTARY MATERIAL

The Supplementary Material for this article can be found online at: http://www.frontiersin.org/journal/10.3389/fphys.2014.00367/abstract

REFERENCES

Anandasabapathy, S. (2008). Endoscopic imaging: emerging optical techniques for the detection of colorectal neoplasia. *Curr. Opin. Gastroenterol.* 24, 64–69. doi: 10.1097/MOG.0b013e3282f2df8d

Andersen, H. O., De Leval, M. R., Tsang, V. T., Elliott, M. J., Anderson, R. H., and Cook, A. C. (2006). Is complete heart block after surgical closure of ventricular septum defects still an issue? *Ann. Thorac. Surg.* 82, 948–956. doi: 10.1016/j.athoracsur.2006.04.030

Anderson, R. H., Ho, S. Y., and Becker, A. E. (1983). The surgical anatomy of the conduction tissues. *Thorax* 38, 408–420. doi: 10.1136/thx.38.6.408

Andries, L. J., and Brutsaert, D. L. (1994). Endocardial endothelium in the rat: junctional organization and permeability. *Cell Tissue Res.* 277, 391–400. doi: 10.1007/BF00300211

Becker, V., Von Delius, S., Bajbouj, M., Karagianni, A., Schmid, R. M., and Meining, A. (2008). Intravenous application of fluorescein for confocal laser scanning microscopy: evaluation of contrast dynamics and image quality with increasing injection-to-imaging time. *Gastrointest. Endosc.* 68, 319–323. doi: 10.1016/j.gie.2008.01.033

Bharali, D. J., Klejbor, I., Stachowiak, E. K., Dutta, P., Roy, I., Kaur, N., et al. (2005). Organically modified silica nanoparticles: a nonviral vector for *in vivo* gene delivery and expression in the brain. *Proc. Natl. Acad. Sci. U.S.A.* 102, 11539–11544. doi: 10.1073/pnas.0504926102

Bolte, S., and Cordelières, F. P. (2006). A guided tour into subcellular colocalization analysis in light microscopy. *J. Microsc.* 224, 213–232. doi: 10.1111/j.1365-2818.2006.01706.x

Brown, R. E. (1965). The pattern of the microcirculatory bed in the ventricular myocardium of domestic mammals. *Am. J. Anat.* 116, 355–374. doi: 10.1002/aja.1001160203

Chilingaryan, A., Chilingaryan, A. M., Chilingaryan, M., and Martin, G. G. (2014). Three-dimensional microvasculature in rat and human hearts using a non-injection Ca2+-ATPase method on thick and ultra-thick sections. *Microsc. Microanal.* 20, 895–902. doi: 10.1017/S1431927614000816

Duane, T. D., Tasman, W., and Jaeger, E. A. (1991). *Duane's Clinical Ophthalmology.* Philadelphia, PA: Lippincott.

Eskridge, J. B., Amos, J. F., and Bartlett, J. D. (1991). *Clinical Procedures in Optometry.* Philadelphia, PA: Lippincott.

Fatin-Rouge, N., Starchev, K., and Buffle, J. (2004). Size effects on diffusion processes within agarose gels. *Biophys. J.* 86, 2710–2719. doi: 10.1016/S0006-3495(04)74325-8

Goetz, M., Hoffman, A., Galle, P. R., Neurath, M. F., and Kiesslich, R. (2006). Confocal laser endoscopy: new approach to the early diagnosis of tumors of the esophagus and stomach. *Future Oncol.* 2, 469–476. doi: 10.2217/14796694.2.4.469

Huang, C., Kaza, A. K., Hitchcock, R. W., and Sachse, F. B. (2013). Identification of nodal tissue in the living heart using rapid scanning fiber-optics confocal microscopy and extracellular fluorophores. *Circ. Cardiovasc. Imaging* 6, 739–746. doi: 10.1161/CIRCIMAGING.112.000121

Inoue, H., Kudo, S. E., and Shiokawa, A. (2005). Novel endoscopic imaging techniques toward *in vivo* observation of living cancer cells in the gastrointestinal tract. *Clin. Gastroenterol. Hepatol.* 3, S61–S63. doi: 10.1016/S1542-3565(05)00282-X

Johnson, E. M., Berk, D. A., Jain, R. K., and Deen, W. M. (1996). Hindered diffusion in agarose gels: test of effective medium model. *Biophys. J.* 70, 1017–1023. doi: 10.1016/S0006-3495(96)79645-5

Kiesslich, R., and Neurath, M. F. (2005). Endoscopic confocal imaging. *Clin. Gastroenterol. Hepatol.* 3, S58–S60. doi: 10.1016/S1542-3565(05)00252-1

Kim, R. J., Chen, E. L., Lima, J. A., and Judd, R. M. (1996). Myocardial Gd-DTPA kinetics determine MRI contrast enhancement and reflect the extent and severity of myocardial injury after acute reperfused infarction. *Circulation* 94, 3318–3326. doi: 10.1161/01.CIR.94.12.3318

Kwan, A. S., Barry, C., McAllister, I. L., and Constable, I. (2006). Fluorescein angiography and adverse drug reactions revisited: the Lions Eye experience. *Clin. Experiment. Ophthalmol.* 34, 33–38. doi: 10.1111/j.1442-9071.2006.01136.x

Kwiterovich, K. A., Maguire, M. G., Murphy, R. P., Schachat, A. P., Bressler, N. M., Bressler, S. B., et al. (1991). Frequency of adverse systemic reactions after fluorescein angiography. Results of a prospective study. *Ophthalmology* 98, 1139–1142. doi: 10.1016/S0161-6420(91)32165-1

Langendorff, O. (1895). Untersuchungen am uberlebenden Saugetierherzen. *Pflugers Arch.* 61, 291–332. doi: 10.1007/BF01812150

Lasher, R. A., Hitchcock, R. W., and Sachse, F. B. (2009). Towards modeling of cardiac micro-structure with catheter-based confocal microscopy: a novel approach for dye delivery and tissue characterization. *IEEE Trans. Med. Imaging* 28, 1156–1164. doi: 10.1109/TMI.2009.2017376

Lewandowski, D., Barroca, V., Duconge, F., Bayer, J., Van Nhieu, J. T., Pestourie, C., et al. (2010). *In vivo* cellular imaging pinpoints the role of reactive oxygen species in the early steps of adult hematopoietic reconstitution. *Blood* 115, 443–452. doi: 10.1182/blood-2009-05-222711

Minsky, M. (1961). *Microscopy apparatus. US*3013467 A.

Moosbrugger, K. A., and Sheidow, T. G. (2008). Evaluation of the side effects and image quality during fluorescein angiography comparing 2 mL and 5 mL sodium fluorescein. *Can. J. Ophthalmol.* 43, 571–575. doi: 10.3129/i08-122

Ovcina, F., and Cemerlic, D. (1997). Clinical importance of intramural blood vessels in the sino-atrial segment of the conducting system of the heart. *Surg. Radiol. Anat.* 19, 359–363. doi: 10.1007/BF01628501

Pluen, A., Netti, P. A., Jain, R. K., and Berk, D. A. (1999). Diffusion of macromolecules in agarose gels: comparison of linear and globular configurations. *Biophys. J.* 77, 542–552. doi: 10.1016/S0006-3495(99)76911-0

Sachse, F. B., Bridge, J. H., and Hitchcock, R. (2011). *Dye application for confocal imaging of cellular microstructure*. US2013/057419.

Sachse, F. B., Hitchcock, R., Huang, C., and Kaza, A. K. (2013). *Devices and systems for fluorescence imaging of tissue*. US2013/022247.

Saeed, M., Weber, O., Lee, R., Do, L., Martin, A., Saloner, D., et al. (2006). Discrimination of myocardial acute and chronic (scar) infarctions on delayed contrast enhanced magnetic resonance imaging with intravascular magnetic resonance contrast media. *J. Am. Coll. Cardiol.* 48, 1961–1968. doi: 10.1016/j.jacc.2006.03.071

Salaun, M., Roussel, F., Bourg-Heckly, G., Vever-Bizet, C., Dominique, S., Genevois, A., et al. (2013). *In vivo* probe-based confocal laser endomicroscopy in amiodarone-related pneumonia. *Eur. Respir. J.* 42, 1646–1658. doi: 10.1183/09031936.00191911

Shahid, M. W., Crook, J. E., Meining, A., Perchant, A., Buchner, A., Gomez, V., et al. (2011). Exploring the optimal fluorescein dose in probe-based confocal laser endomicroscopy for colonic imaging. *J. Interv. Gastroenterol.* 1, 166–171. doi: 10.4161/jig.19953

Thiberville, L., Salaun, M., Lachkar, S., Dominique, S., Moreno-Swirc, S., Vever-Bizet, C., et al. (2009). Human *in vivo* fluorescence microimaging of the alveolar ducts and sacs during bronchoscopy. *Eur. Respir. J.* 33, 974–985. doi: 10.1183/09031936.00083708

Vincent, P., Maskos, U., Charvet, I., Bourgeais, L., Stoppini, L., Leresche, N., et al. (2006). Live imaging of neural structure and function by fibred fluorescence microscopy. *EMBO Rep.* 7, 1154–1161. doi: 10.1038/sj.embor.7400801

Wallace, M. B., Meining, A., Canto, M. I., Fockens, P., Miehlke, S., Roesch, T., et al. (2010). The safety of intravenous fluorescein for confocal laser endomicroscopy in the gastrointestinal tract. *Aliment. Pharmacol. Ther.* 31, 548–552. doi: 10.1111/j.1365-2036.2009.04207.x

Wu, K., Liu, J. J., Adams, W., Sonn, G. A., Mach, K. E., Pan, Y., et al. (2011). Dynamic real-time microscopy of the urinary tract using confocal laser endomicroscopy. *Urology* 78, 225–231. doi: 10.1016/j.urology.2011.02.057

Conflict of Interest Statement: A patent related to FCM imaging of tissues and dye application has been issued (Dye application for confocal imaging of cellular microstructure, US2013/057419, University of Utah Research Foundation). A patent application related to fluorescence imaging of tissue is pending (Devices and systems for fluorescence imaging of tissue, US2013/022247, University of Utah Research Foundation). The authors declare that the research was conducted in the absence of any commercial or financial relationships that could be construed as a potential conflict of interest.

Received: 31 July 2014; accepted: 07 September 2014; published online: 25 September 2014.

Citation: Huang C, Kaza AK, Hitchcock RW and Sachse FB (2014) Local delivery of fluorescent dye for fiber-optics confocal microscopy of the living heart. Front. Physiol. 5:367. doi: 10.3389/fphys.2014.00367

This article was submitted to Cardiac Electrophysiology, a section of the journal Frontiers in Physiology.

Copyright © 2014 Huang, Kaza, Hitchcock and Sachse. This is an open-access article distributed under the terms of the Creative Commons Attribution License (CC BY). The use, distribution or reproduction in other forums is permitted, provided the original author(s) or licensor are credited and that the original publication in this journal is cited, in accordance with accepted academic practice. No use, distribution or reproduction is permitted which does not comply with these terms.

CHAPTER 4

HIGH SENSITIVITY AND SPECIFICITY OF CARDIAC TISSUE DISCRIMINATION USING FIBER-OPTICS CONFOCAL MICROSCOPY

4.1 Introduction

Congenital heart disease is the most common birth defect, which affects approximately 1% of all live births.[1] The main treatment modality is surgical repair. Tremendous progress was made over the past half century to lower the incidence of conduction disturbances following surgical repair of congenital heart defects. The primary therapeutic intervention in treating persistent conduction disturbances is permanent pacemaker implantation. Improved understanding of the anatomy of the conduction system and advances in surgical techniques have reduced the incidence of disturbances after repair of some common congenital lesions such as ventricular septal defect from greater than 10% to 1 – 3%.[2-4] However, repair of complex cardiac malformations including abnormally related great arteries, AV discordance, and single ventricle physiology are still associated with high incidence of permanent pacemaker implantation. For instance, the incidence is 41 – 48% after repair of congenitally corrected transposition of the great arteries.[5-7]

Currently, in order to prevent conduction disturbances, surgeons rely on anatomical landmarks to approximate the location of the cardiac conduction system. In complex cardiac malformations where the location of these specialized tissues is distorted, the established approach may not be able to localize the conduction tissue.[8-10] With an increasing prevalence of complex cardiac malformations,[11, 12] and therefore increasing occurrence of surgical correction for these less common malformations, a more reliable and accurate intraoperative method for localizing the conduction system is indicated. There have been previous attempts at electrophysiological identification of the conduction system during open heart surgery.[9, 13, 14] However, the reliance on atrial pacing to achieve reliable recordings without arrhythmias limited the application of these electrophysiology-based localization techniques.

Fiber-optics confocal microscopy (FCM) allows for real-time imaging of cellular and sub-cellular features up to 100 μm below the specimen's surface. Current clinical applications of FCM include imaging of tissues in the gastrointestinal[15], respiratory[16, 17], and urinary[18] system. We recently introduced FCM for imaging in the living heart.[19, 20] In these studies, we demonstrated feasibility of cardiac tissue discrimination using FCM and local delivery of extracellular fluorophores. In particular, we were able to discriminate the specialized tissue of the conduction system in the sinoatrial node (SAN) and atrioventricular node (AVN) from atrial working myocardium (AWM) in the living heart of a rodent model.

In this study, we investigated the performance of blinded human examiners in discriminating images of AWM and specialized tissue of the conduction system acquired using FCM. In addition, we evaluated automated classification systems for cardiac tissue discrimination. Our hypothesis is that human and automated tissue classification can discriminate FCM images of AWM and specialized tissue of the conduction system with high sensitivity and specificity. For this purpose, we used conventional three-dimensional confocal microscopy, FCM, and two methods for local delivery of extracellular fluorophores to acquire images from AWM and nodal tissue from the SAN and AVN. Spatial regularity of the extracellular space in the images of AWM and nodal tissue was measured using texture analysis. Optimal cutoff values for automated tissue classification were extrapolated based on receiver operating characteristic (ROC) analysis of the spatial regularity distributions. Subsequently, we evaluated the sensitivity and specificity of human and automated classification in discriminating a set of randomly selected images of AWM and nodal tissue.

4.2 Materials and Methods

4.2.1 Heart Tissue Preparations

Animal procedures were approved by the University of Utah Institutional Care and Use Committee and followed the guidelines of the National Institutes of Health Guide for the Care and Use of Laboratory Animals. Human studies were reviewed and approved for exemption by the institutional review board at the

University of Utah. Details on the preparation and fluorescent labeling of fixed tissue samples from rodent, neonatal ovine, and human hearts are provided in the Online Data Supplement.

4.2.1.1 Rodent

Young adult Sprague-Dawley rats (≈300 g) were anesthetized with intraperitoneal injections of sodium pentobarbital (40 mg/kg) containing heparin (500 IU/kg). Following anesthesia, the hearts were rapidly excised and mounted on a Langendorff perfusion system.[21] Isolated hearts were then continuously perfused with oxygenated, high-K/low-Ca Tyrode's solution (in mmol/L: 92 NaCl, 11 dextrose, 13.2 KCl, 5 $MgCl_2$, 24 HEPES, 20 taurine, 5 creatine, 5 $C_3H_3NaO_3$, 1 NaH_2PO_4, 0.25 $CaCl_2$; pH 7.2; ≈10°C) at a flow rate of 10-15 mL/min. For fixed tissue preparations, perfusion was switched after 5 min to a perfusate of Tyrode's solution containing 4% paraformaldehyde (pH 7.4). Following a 10-min perfusion of fixative solution, the hearts were immersed in phosphate buffered saline (PBS) containing 4% paraformaldehyde for 24 h at 4°C. Tissue from the AWM, SAN, and AVN were dissected from the fixed hearts and stored in PBS at 4°C prior to immunofluorescent labeling.

4.2.1.2 Ovine

Hearts were obtained from a study on a preterm model of neonatal chronic lung disease.[22] Hearts and fixed tissue were prepared in a similar manner based on the previously described rodent model.

4.2.1.3 Human

Studies were reviewed and approved for exemption by the institutional review board at the University of Utah. We obtained fixed tissue samples from the AWM and AVN regions of an autopsy heart from a 38-week-old fetus.

4.2.2 Fluorescent Labeling of Fixed Tissue

Fixed tissue preparations from rat, neonatal ovine, and human were washed 3x in PBS and incubated overnight with wheat germ agglutinin (WGA) conjugated to CF488A (29022-1; Biotium, Hayward, CA; 1:25). The next day, ovine and human tissue preparations were rinsed and stored in PBS until imaging. Rat tissue preparations were further labeled using established methods.[19] In short, the preparations were rinsed 3x in PBS then permeabilized and blocked for 1 h in PBS solution containing 0.5% Triton X-100 and 4% normal goat serum (16210-064; Gibco, Grand Island, NY). Immediately following, the preparations were bathed for 1 h in Image-iT Signal Enhancer (I36933; Invitrogen, Carlsbad, CA). Preparations were then rinsed in PBS and incubated overnight on a laboratory platform rocker at room temperature with primary antibody solution. The primary antibody solution consisted of PBS, 4% normal goat serum, and antihyperpolarization-actived cyclic nucleotide-gated potassium channel 4 (HCN4; ab69054; Abcam, Cambridge, MA; 1:100). The following day, the preparations were washed 3x in PBS then incubated overnight on a rocker at room temperature in PBS solution containing secondary IgG (goat anti-rabbit IgG

H+L) conjugated to Alexa Fluor 555 (A-21429; Invitrogen; 1:40). The next day, preparations were given a final rinse and stored in PBS until imaging.

4.2.3 Imaging of Fluorescently Labeled Fixed Tissue

Fluorescently labeled tissue preparations from rodent, neonatal ovine, and human were imaged using a conventional laser-scanning confocal microscope (Zeiss LSM5 Duo; Zeiss, Jena, Germany) based on established methods.[19, 23] Fluorescently labeled tissue preparations from rodent, neonatal ovine, and human were imaged using a conventional laser-scanning confocal microscope (Zeiss LSM5 Duo; Zeiss, Jena, Germany) based on established methods.[19, 23] Images of WGA-CF488A associated fluorescence were acquired using an Argon/2 ion laser for excitation at 488 nm and bandpass filter for 505 to 555 nm emissions. Images of anti-HCN4-Alexa 555 associated fluorescence were acquired using a HeNe laser for excitation at 543 nm and a long pass filter for >560 nm emissions. High magnification image stacks were captured using a 40x oil immersion lens having a numeric aperture of 1.3. These 3D image stacks were acquired at a 0.2x0.2x0.2 µm spatial resolution (*xyz* dimensions) with a *xy* field of view of 204.8x204.8 µm and a *z*-scan range of 50 µm. Anatomical overview images were acquired with the conventional confocal microscope using a 2.5x and 10x air objective with numeric apertures of 0.12 and 0.30, respectively.

Representative cross-sections through image stacks from fixed rodent tissue preparations are presented in Figure 4.1. These image stacks were

acquired from the epicardial surface into the subepicardial AWM. AWM (Figure 4.1, *A* and *B*) and SAN (Figure 4.1, *C* and *D*) tissue were labeled with WGA (Figure 4.1, *A* and *C*) and anti-HCN4 (Figure 4.1, *B* and *D*). WGA was used to visualize constituents of the extracellular space, the outer membrane of cells, and the tissue microstructure.[24, 25] We used anti-HCN4 to detect cells of the conduction system.[26-29] We also present example cross-sections through image stacks of fixed neonatal ovine (Figure 4.2, *A* and *B*) and human tissue preparations (Figure 4.2, *C* and *D*). The AWM (Figure 4.2, *A* and *C*) and AVN (Figure 4.2, *B* and *D*) were labeled with WGA only. All acquired high magnification image stacks were indexed based on anatomical origin of the imaged tissue region, i.e., AWM or nodal tissue. Indexed images, in particular a set of image stacks acquired from WGA-labeled rodent tissues (referred to as CCM images), were stored for subsequent image analysis. Additionally, we acquired anatomical overviews of the right atrium from fixed rodent hearts labeled with WGA and anti-HCN4. A representative anatomical overview of the HCN4 distribution in the partial right atrium of rodent is presented in Figure 4.3.

4.2.4 FCM Imaging of the Living Heart

In addition to conventional confocal microscopy of fixed tissue preparations, we performed FCM on Langendorff-perfused arrested hearts from rodent and neonatal ovine. Two-dimensional image sequences were acquired using a FCM system (FCM 1000; Leica Microsystems GmbH, Wetzlar, Germany) and two methods for local delivery of fluorescent dye.[19, 20]

The first method was based on topical application of fluorescent dye via pipette to AWM, SAN, and AVN tissue regions of perfused rodent and neonatal ovine hearts. The fluorescent dye solution consisted of 3 or 10 kDa dextran conjugated to Alexa Fluor 488 (Invitrogen, Carlsbad, CA, 1:8) dissolved in Tyrode's solution to a final concentration of 125 μg/mL. Following dye delivery, tissue regions were imaged using the FCM system equipped with a custom fiber-optics microprobe (UltraMiniO; Mauna Kea Technologies, Paris, France). Two-dimensional image sequences were acquired at a lateral resolution (*xy* dimensions) of 1.8 μm, optical sectioning (*z*) of 10 μm, *xy* field of view of 169 by 120 μm, frame rate of 12 Hz, and z-scan range of 50 μm. Images from rodent acquired with this topical method of dye delivery are subsequently referred to as $FCM_{topical}$ images. We acquired images from rodent (Figure 4.4, *A* and *B*) and neonatal ovine (Figure 4.4, *C* and *D*) of AWM (Figure 4.4, *A* and *C*) and AVN (Figure 4.4, *B* and *D*) following topical application of dextran-Alexa Fluor 488.

Rodent hearts were also imaged using FCM and a method of local dye delivery based on a dye carrier affixed to the tip of the FCM imaging microprobe. Dye carriers were fabricated according to a recently described method[20] and loaded for 15 min with fluorescent dye, sodium fluorescein [Fluorescite® (fluorescein injection, USP) 10%; Alcon, Fort Worth, TX, US; 1:1000]. Images from AWM, SAN, and AVN regions of perfused rodent hearts were acquired using this method with a custom fiber-optics microprobe (UltraMiniOWD30; Mauna Kea Technologies) at a lateral resolution (*xy*) of 1.4 μm, optical sectioning (*z*) of 7 μm, *xy* field of view of 186 by 130 μm, frame rate of 12 Hz, and a z-scan

range of 26 μm. Images from rodent acquired with the dye carrier method are subsequently referred to as $FCM_{carrier}$ images. $FCM_{topical}$ and $FCM_{carrier}$ images were indexed based on anatomical origin, i.e., AWM or nodal, and stored for subsequent image analysis.

4.2.5 Image Analysis

We characterized the spatial regularity of the extracellular space in CCM, $FCM_{topical}$, and $FCM_{carrier}$ images using two methods of image texture analysis. The spatial regularity of the extracellular space in CCM, $FCM_{topical}$, and $FCM_{carrier}$ images was analyzed using two previously described methods of image texture analysis.[19] The first method involved transforming images into the Fourier domain and sampling intensities within circular sectors bounded by spatial frequencies between 0.07 to 0.2 μm^{-1}. The intensities within the circular sectors were binned along central angles of 10° and normalized across all bins. The distribution of the binned intensities along the angular spectra provides an indication of the spatial regularity of the extracellular space. Broad and narrow distributions of intensities indicate low and high spatial regularity, respectively. The second method of texture analysis was based on second-order image moments calculated from subregions in decomposed images. The local orientation and scaling of the second-order image moments were derived from singular value decomposition. The relative frequency distribution of the local orientations within all subregions of an image was used to characterize the image's spatial regularity. For both methods of texture analysis, a quantitative measure of spatial regularity, I_{15}, was

calculated based on the sum of frequencies within 15° of the peak of the angular spectra. The I_{15} value was determined using both methods of texture analysis for all CCM, $FCM_{topical}$, and $FCM_{carrier}$ images. We subsequently developed automated classification systems based on the I_{15} distribution of these image sets. In our classification scheme, we defined true positive and true negative outcomes as AWM correctly classified as AWM and nodal images correctly classified as nodal, respectively.

4.2.6 Automated Classification of Tissue Images

We evaluated automated methods for classification of AWM and nodal images based on texture analysis. We mapped I_{15} values calculated from both Fourier and second-order moment analyses of CCM, $FCM_{topical}$, and $FCM_{carrier}$ images to ROC curves. ROC curves were obtained using the "perfcurve" function of the MATLAB (The Mathworks Inc, Natick, MA) Statistics Toolbox. In addition, for each ROC curve, we calculated an optimal cutoff value, which maximizes the product of sensitivity times specificity and therefore minimizes both the false-positives and false-negative cases. In calculation of the optimal cutoff values, additional weight was given for the misclassification of negative results. We defined false positives (i.e., nodal misclassified as AWM) two times as costly as false negatives (i.e., AWM misclassified as nodal). Eighty-one images from CCM, $FCM_{topical}$, and $FCM_{carrier}$ were randomly selected and classified as either AWM or nodal images using automated methods based on these optimal cutoff values.

The sensitivity and specificity of these automated methods in discriminating these cardiac tissue types was determined from these classifications.

4.2.7 Human Examiner Classification of Tissue Images

Eight human examiners reviewed the set of CCM, $FCM_{topical}$, and $FCM_{carrier}$ images previously classified by automated methods. The examiners were asked to classify the images as AWM or nodal following a 5-minute training phase. Training consisted of a slide presentation of previously indexed images of AWM and nodal tissue that illustrated microstructural features indicative of each tissue type. Examiners were blinded to the classification of the images. Sensitivity and specificity of these examiners in discriminating AWM and nodal images was determined from these classifications. The previously defined classification scheme for a true positive and true negative outcome was used in determining the sensitivity and specificity.

4.3 Results

Image stacks and sequences of AWM, SAN, and AVN regions were acquired using conventional confocal microscopy, FCM, and two methods for fluorescent dye delivery. The resulting images, CCM, $FCM_{topical}$, and $FCM_{carrier}$, were indexed based on anatomical origin of imaged region and analyzed using texture analysis. In our analysis, we extracted features of the microstructural arrangement from the extracellular space within these images, in particular the spatial regularity. We then mapped the spatial regularity to a simple score

denoted as I_{15}. Analysis of ROC curves generated from these I_{15} values allowed us to determine optimal cutoff values for automated classification. Histograms and ROC curves of I_{15} for CCM (Figure 4.5, *A-C*), $FCM_{topical}$ (Figure 4.5, *D-F*), and $FCM_{carrier}$ (Figure 4.5, *G-I*) images are presented for both Fourier and image moment-based texture analysis. We observed a characteristic bimodal distribution of I_{15} regardless of the method of texture analysis or imaging approach. The distributions coincided distinctively with indexed anatomical regions. I_{15} values derived from nodal and AWM images were distributed around the lower and higher maxima, respectively. The ROC curves were obtained by varying the decision threshold between the minimum and the maximum I_{15} of CCM (Figure 4.5, *C*), $FCM_{topical}$ (Figure 4.5, *F*), and $FCM_{carrier}$ (Figure 4.5, *I*) images calculated from Fourier (green dotted line) and image moment (solid red line) analysis. The inset within the ROC curves shows a magnified view of the curve closest to the region of perfect classification. The inset also shows optimal cutoff values for CCM, $FCM_{topical}$, and $FCM_{carrier}$ images based on Fourier and image moment analysis. The optimal cutoff value was calculated based on minimizing the distance between the ROC curve and the upper left corner of the plot with the addition of a weighting factor based on the misclassification cost of AWM and nodal images. Details on the ROC analysis are presented in Table 4.1, including sample sizes as well as the sensitivity and specificity for each optimal cutoff value.

In a last set of experiments, we evaluated the performance of human and automated classification systems in discriminating AWM and nodal images. A

random set of 81 AWM and 81 nodal images from each of the CCM, $FCM_{topical}$, and $FCM_{carrier}$ image sets were evaluated by 8 human examiners. Preceding the evaluation, the examiners were trained to identify hallmark features in the microstructural arrangement of the extracellular space that allowed for AWM and nodal identification. In addition, the same set of images was evaluated by automated classification systems based on optimal cutoff values from ROC curves and two methods of image texture analysis described above. The sensitivity and specificity of human and automated classification systems in discriminating AWM and nodal images are shown in Table 4.2. Human examiner results are presented as mean ± standard error. We achieved a sensitivity of 99.2% ± 0.3 and specificity of 98.0% ± 0.7 in human examiner evaluation of $FCM_{carrier}$ images. $FCM_{carrier}$ images were acquired using the dye carrier method of fluorescent dye delivery. Approximately 1 AWM image was misclassified as nodal (false negative) and approximately 2 nodal images were misclassified as AWM (false positive) from the 81 AWM and 81 nodal images classified. In comparison, human examiners misclassified approximately 1 AWM (99.2% ± 0.3 sensitivity) and 5 nodal (94.0% ± 2.4 specificity) images in evaluating images acquired using dye application via pipette ($FCM_{topical}$). A comprehensive summary of the sensitivity and specificity for each human examiner and each image set evaluated is presented in Table 4.3. Sensitivity and specificity for the automated method of classification based on Fourier analysis was 97.5% and 95.1%, respectively, for the $FCM_{carrier}$ images. In this case, approximately 2 AWM and 4 nodal images were misclassified from the total 162 $FCM_{carrier}$ images. In

comparison, sensitivity and specificity of automated classification based on image moments was 100% (0 AWM images misclassified) and 92.6% (6 nodal images misclassified), respectively.

4.4 Discussion

Our studies provide evidence that human examiners can discriminate images of AWM and nodal tissue acquired using FCM with extremely high sensitivity and specificity. We also found that automated classification systems were similarly effective at discriminating these cardiac tissue types as human examiners. These results suggest that automated classification has potential to support intraoperative FCM discrimination of AWM and nodal tissue. Furthermore, the sensitivity and specificity of both human and automated classification were similar in discriminating CCM, $FCM_{topical}$, and $FCM_{carrier}$ (Table 4.2). This suggests that differences in the imaging approach such as method of fluorescent dye delivery, imaging modality, and type of fluorescent or optical properties of the imaging probe have only marginal effects on the reliability of human and automated tissue discrimination. However, human examiners achieved the highest specificity in discriminating $FCM_{carrier}$ images resulting in only approximately 2 misclassifications of nodal images as AWM images compared to approximately 4-11 nodal misclassifications by the other classifications performed (Table 4.2). This result is important in the context of pediatric open heart surgery as we are biased towards reducing the number of nodal rather than AWM misclassifications.

We showed previously that the dye carrier approach applied in acquiring $FCM_{carrier}$ images is more appropriate for clinical applications of FCM, in particular for translation of FCM for pediatric open heart surgery.[20] The local dye delivery approach was as effective as established systemic dye delivery in visualization of the microstructural arrangement of tissue. However, local dye delivery using a dye carrier required a lower amount of dye than systemic delivery. To obtain FCM images of sufficient quality over an 8-minute imaging session required approximately 4.1 and 240 μg of fluorescent dye using local or systemic dye delivery methods, respectively. The lower amount of dye required would make local dye delivery more preferable than systemic methods in the clinical environment.

Our study revealed that the microstructural features of AWM and nodal tissue in neonatal ovine resemble that of rodent and human. A characteristic microstructural feature of AWM in rodent (Figure 4.1, *A* and Figure 4.4, *A*), neonatal ovine (Figure 4.2, *A* and Figure 4.4, *C*), and human (Figure 4.2, *C*) is the regularly striated arrangement of the extracellular space. This arrangement is a hallmark of the underlying oriented arrangement of myocytes. In contrast, nodal tissue images from rodent (Figure 4.2, *C* and Figure 4.4, *B*), neonatal ovine (Figure 4.2, *B* and Figure 4.4, *D*) and human (Figure 4.2, *D*) were characterized by an irregular, reticular arrangement. We showed previously that an irregular, reticular arrangement is a characteristic microstructural feature of nodal tissue.[19] Our findings in this study support that the microstructural arrangement of AWM and nodal tissue are similar across rodent, human, and neonatal ovine. We

suggest based on these findings that neonatal ovine is an appropriate animal model for investigating the ability of FCM to delineate the conduction system, in particular for applications in pediatric open heart surgery.

There are certain limitations associated with FCM such as penetration depth and spatial resolution. Current FCM systems can image to a depth of approximately 100 μm at submicrometer resolution. We have shown that up to 50 μm in depth, microstructural features of cardiac tissue types can be discerned to allow for their discrimination, particularly in fetal and infant human hearts (see [19], and Figure 4.2, *C* and *D*). Therefore, we expect that the penetration depth and resolution is sufficient for clinical application of FCM for cardiac tissue discrimination, specifically for pediatric open heart surgery. In addition, recently developed *in vivo* fluorescence imaging systems work at near-infrared wavelengths. These wavelengths will allow higher penetration depth than current imaging systems using wavelengths of visible light.[30]

A further limitation is associated with the use of FCM images acquired from isolated rodent hearts in the evaluation of human and automated tissue discrimination. We expect, based on the analysis of the microstructural features in rodent and human performed previously[19] and in this study, that a similarly high sensitivity and specificity of tissue discrimination can be achieved in the neonatal and infant human heart *in situ*.

In conclusion, we demonstrated that human and automated classification systems can achieve high sensitivity and specificity in discriminating images of AWM and nodal tissue acquired using FCM and extracellular fluorophores. We

believe that the results of this study would facilitate clinical translation of FCM as an intraoperative imaging modality to reduce the incidence of conduction disturbances during surgical correction of congenital heart disease

4.5 References

1. Go AS, Mozaffarian D, Roger VL, Benjamin EJ, Berry JD, Blaha MJ, et al. Heart disease and stroke statistics--2014 update: a report from the American Heart Association. *Circulation.* 2014;129:e28-e292.

2. Lillehei CW, Sellers RD, Bonnabeau RC, Eliot RS. Chronic Postsurgical Complete Heart Block. With Particular Reference to Prognosis, Management, and a New P-Wave Pacemaker. *J Thorac Cardiovasc Surg.* 1963;46:436-56.

3. Bonatti V, Agnetti A, Squarcia U. Early and late postoperative complete heart block in pediatric patients submitted to open-heart surgery for congenital heart disease. *Pediatr Med Chir.* 1998;20:181-6.

4. Weindling SN, Saul JP, Gamble WJ, MayerJr JE, Wessel D, Walsh EP. Duration of complete atrioventricular block after congenital heart disease surgery. *Am J Cardiol.* 1998;82:525-7.

5. Bogers AJ, Head SJ, de Jong PL, Witsenburg M, Kappetein AP. Long term follow up after surgery in congenitally corrected transposition of the great arteries with a right ventricle in the systemic circulation. *J Cardiothorac Surg.* 2010;5:74.

6. Graham TP, Jr., Bernard YD, Mellen BG, Celermajer D, Baumgartner H, Cetta F, et al. Long-term outcome in congenitally corrected transposition of the great arteries: a multi-institutional study. *J Am Coll Cardiol.* 2000;36:255-61.

7. Connelly MS, Liu PP, Williams WG, Webb GD, Robertson P, McLaughlin PR. Congenitally corrected transposition of the great arteries in the adult: functional status and complications. *J Am Coll Cardiol.* 1996;27:1238-43.

8. Anderson RH, Ho SY, Becker AE. The surgical anatomy of the conduction tissues. *Thorax.* 1983;38:408-20.

9. Dick M, 2nd, Norwood WI, Chipman C, Castaneda AR. Intraoperative recording of specialized atrioventricular conduction tissue electrograms in 47 patients. *Circulation.* 1979;59:150-60.

10. Walsh EP. Interventional electrophysiology in patients with congenital heart disease. *Circulation.* 2007;115:3224-34.

11. Archer JM, Yeager SB, Kenny MJ, Soll RF, Horbar JD. Distribution of and mortality from serious congenital heart disease in very low birth weight infants. *Pediatrics.* 2011;127:293-9.

12. Marelli AJ, Mackie AS, Ionescu-Ittu R, Rahme E, Pilote L. Congenital heart disease in the general population: changing prevalence and age distribution. *Circulation.* 2007;115:163-72.

13. Lincoln C, Butler P, Logan-Sinclair R, Anderson RH. A cardiac conduction monitor and probe for intraoperative identification of conduction tissue. *Br Heart J.* 1979;42:339-44.

14. Kaiser GA, Waldo AL, Beach PM, Bowman FO, Jr., Hoffman BF, Malm JR. Specialized cardiac conduction system. Improved electrophysiologic identification technique at surgery. *Arch Surg.* 1970;101:673-6.

15. Sharma P, Meining AR, Coron E, Lightdale CJ, Wolfsen HC, Bansal A, et al. Real-time increased detection of neoplastic tissue in Barrett's esophagus with probe-based confocal laser endomicroscopy: final results of an international multicenter, prospective, randomized, controlled trial. *Gastrointest Endosc.* 2011;74:465-72.

16. Salaun M, Roussel F, Bourg-Heckly G, Vever-Bizet C, Dominique S, Genevois A, et al. In vivo probe-based confocal laser endomicroscopy in amiodarone-related pneumonia. *Eur Respir J.* 2013;42:1646-58.

17. Thiberville L, Salaun M, Lachkar S, Dominique S, Moreno-Swirc S, Vever-Bizet C, et al. Human in vivo fluorescence microimaging of the alveolar ducts and sacs during bronchoscopy. *Eur Respir J.* 2009;33:974-85.

18. Wu K, Liu JJ, Adams W, Sonn GA, Mach KE, Pan Y, et al. Dynamic real-time microscopy of the urinary tract using confocal laser endomicroscopy. *Urology.* 2011;78:225-31.

19. Huang C, Kaza AK, Hitchcock RW, Sachse FB. Identification of nodal tissue in the living heart using rapid scanning fiber-optics confocal microscopy and extracellular fluorophores. *Circ Cardiovasc Imaging.* 2013;6:739-46.

20. Huang C, Kaza AK, Hitchcock RW, Sachse FB. Local delivery of fluorescent dye for fiber-optics confocal microscopy of the living heart. *Front Physiol.* 2014;5.

21. Langendorff O. Untersuchungen am überlebenden Säugetierherzen. *Pflügers Arch.* 1895;61:291-332.

22. Rehan VK, Fong J, Lee R, Sakurai R, Wang ZM, Dahl MJ, et al. Mechanism of reduced lung injury by high-frequency nasal ventilation in a preterm lamb model of neonatal chronic lung disease. *Pediatr Res.* 2011;70:462-6.

23. Lackey DP, Carruth ED, Lasher RA, Boenisch J, Sachse FB, Hitchcock RW. Three-dimensional modeling and quantitative analysis of gap junction distributions in cardiac tissue. *Ann Biomed Eng.* 2011;39:2683-94.

24. Bhavanandan VP, Katlic AW. The interaction of wheat germ agglutinin with sialoglycoproteins. The role of sialic acid. *J Biol Chem.* 1979;254:4000-8.

25. Soderstrom KO. Lectin binding to collagen strands in histologic tissue sections. *Histochemistry.* 1987;87:557-60.

26. Chandler NJ, Greener ID, Tellez JO, Inada S, Musa H, Molenaar P, et al. Molecular architecture of the human sinus node: insights into the function of the cardiac pacemaker. *Circulation.* 2009;119:1562-75.

27. Yoo S, Dobrzynski H, Fedorov VV, Xu SZ, Yamanushi TT, Jones SA, et al. Localization of Na+ channel isoforms at the atrioventricular junction and atrioventricular node in the rat. *Circulation.* 2006;114:1360-71.

28. Yamamoto M, Dobrzynski H, Tellez J, Niwa R, Billeter R, Honjo H, et al. Extended atrial conduction system characterised by the expression of the HCN4 channel and connexin45. *Cardiovasc Res.* 2006;72:271-81.

29. Brioschi C, Micheloni S, Tellez JO, Pisoni G, Longhi R, Moroni P, et al. Distribution of the pacemaker HCN4 channel mRNA and protein in the rabbit sinoatrial node. *J Mol Cell Cardiol.* 2009;47:221-7.

30. Hong G, Lee JC, Robinson JT, Raaz U, Xie L, Huang NF, et al. Multifunctional in vivo vascular imaging using near-infrared II fluorescence. *Nat Med.* 2012;18:1841-6.

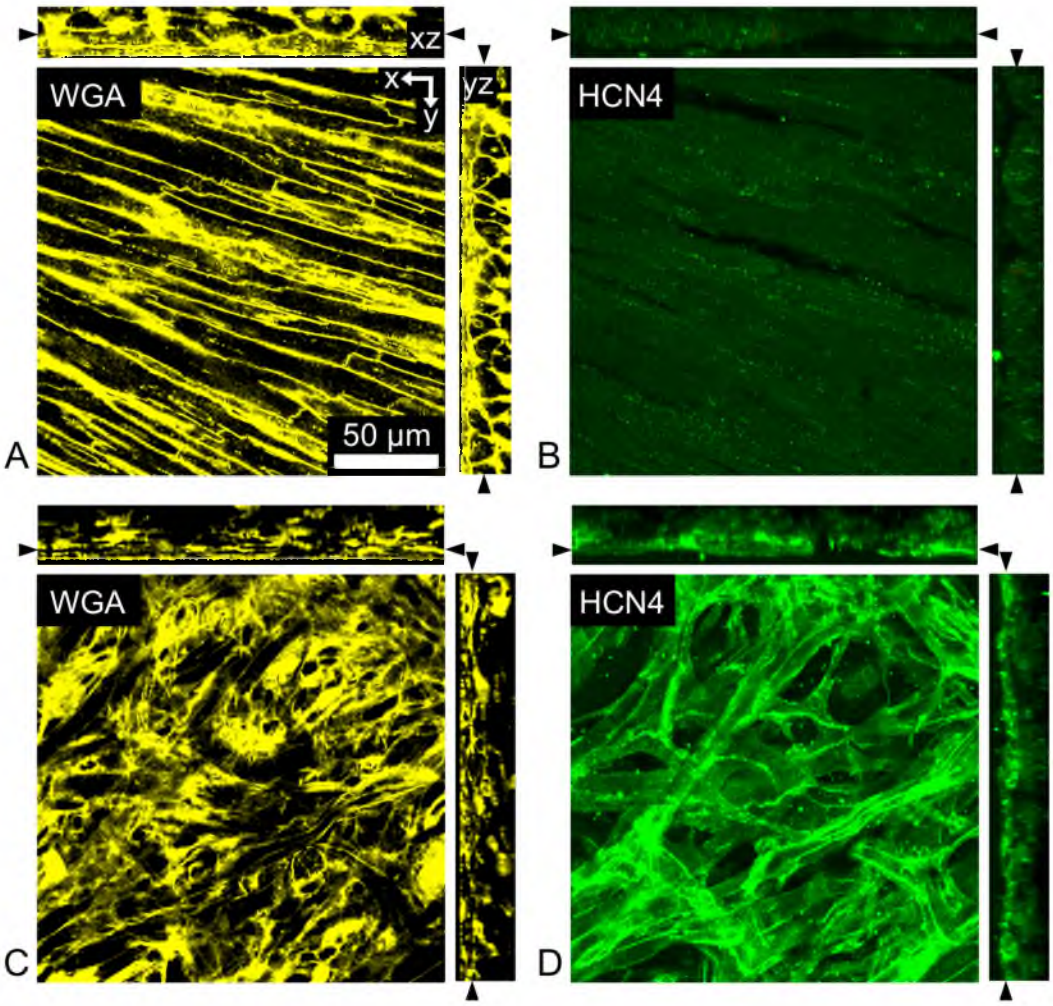

Figure 4.1 Three-dimensional confocal images of rodent tissue. Cross-section through image stacks acquired using laser-scanning confocal microscopy of (A,B) atrial working myocardium and (C,D) sinoatrial node tissue from fixed rodent tissue preparations. Preparations were fluorescently labeled with (A,C) wheat germ agglutinin to visualize constituents of the extracellular space, the outer membrane of cells, and the tissue microstructure. Preparations were also immunofluorescently labeled with (B,D) anti-hyperpolarization-activated cyclic nucleotide-gated potassium channel 4 to detect cells of the conduction system.

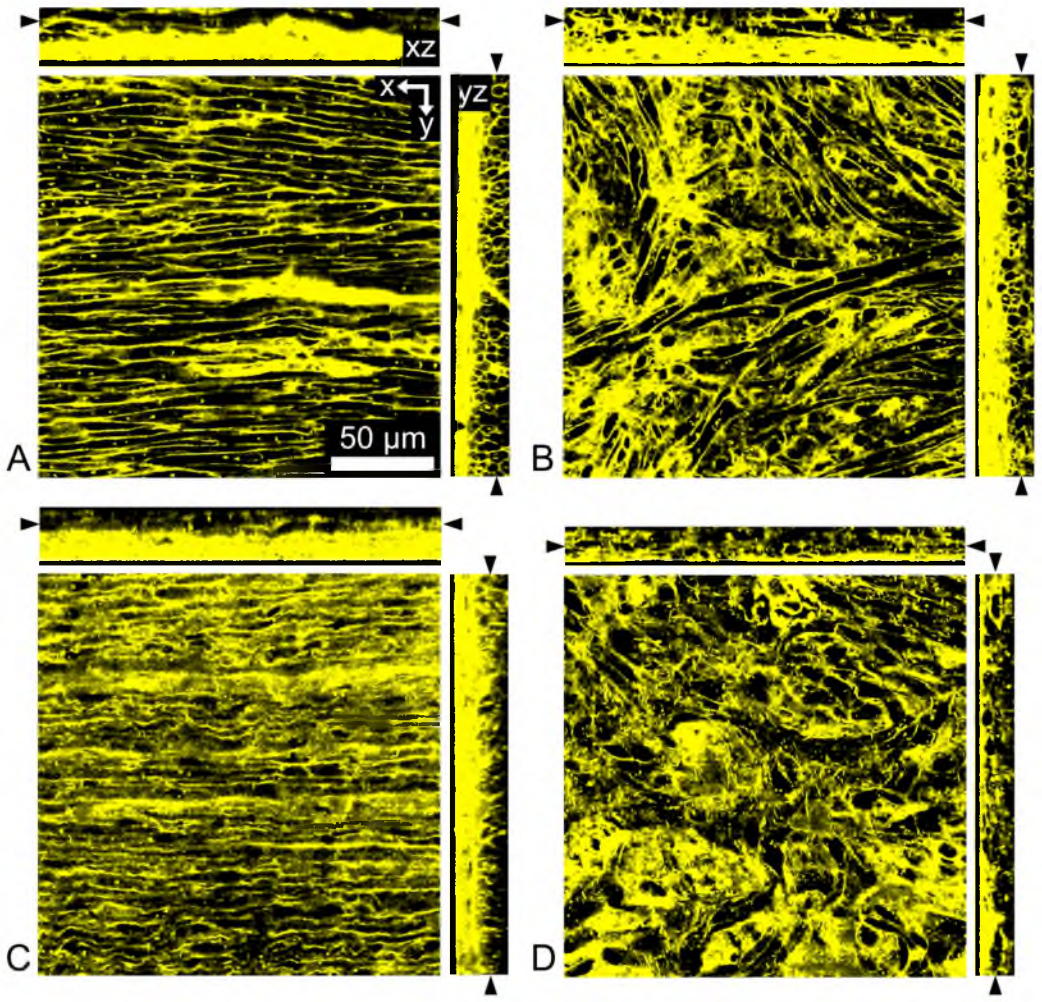

Figure 4.2 Three-dimensional confocal images of neonatal ovine and human tissue. Cross-section through image stacks of fixed (A,B) neonatal ovine and (C,D) human tissue preparations labeled with wheat germ agglutinin. (A,C) Image stacks acquired from the epicardial surface into the subepicardial atrial working myocardium. (B,D) Image stacks acquired from the endocardial surface into the subendocardial atrioventricular node tissue.

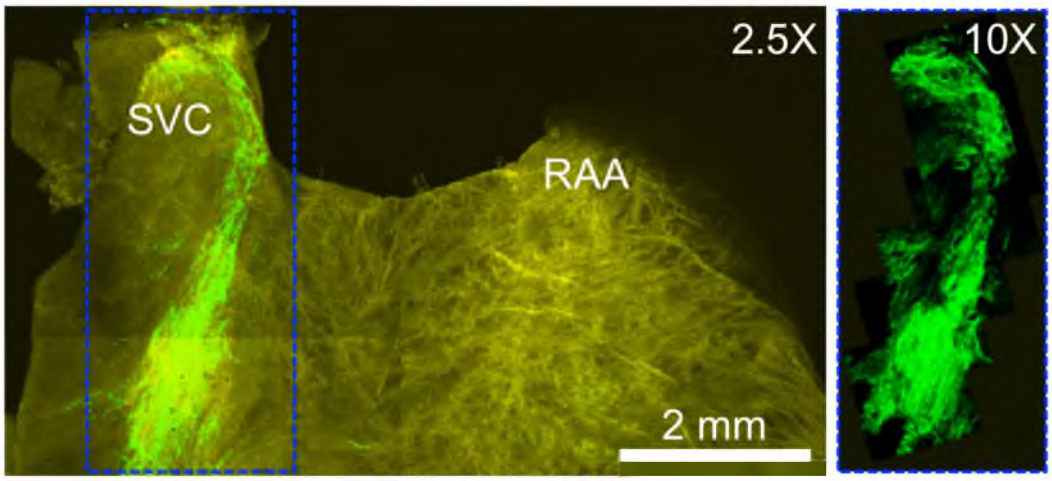

Figure 4.3 Anatomical overview of the right atrium from fixed rodent heart. The right atrium was labeled with wheat germ agglutinin (yellow) and antihyperpolarization-activated cyclic nucleotide-gated potassium channel 4 (green) to visualize the extracellular space and nodal cells, respectively. Zoom in of outlined region (blue line) acquired using a 10x objective. SVC, superior vena cava; RAA, right atrial appendage

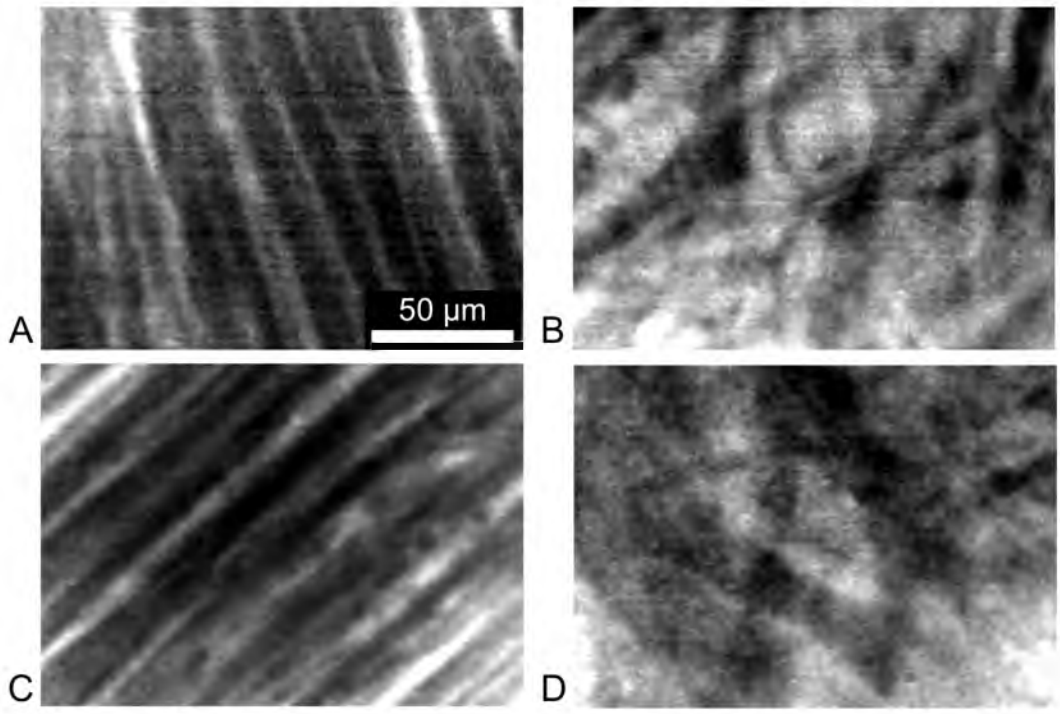

Figure 4.4 Fiber-optics confocal microscopy of the living heart. Example fiber-optics confocal microscopy images acquired from the living arrested heart of (A,B) rodent and (C,D) neonatal ovine. Images were acquired using a UltraMiniO imaging microprobe after topical administration of dextran-Alexa Fluor 488 via pipette to a region of (A,C) atrial working myocardium and (B,D) sinoatrial node.

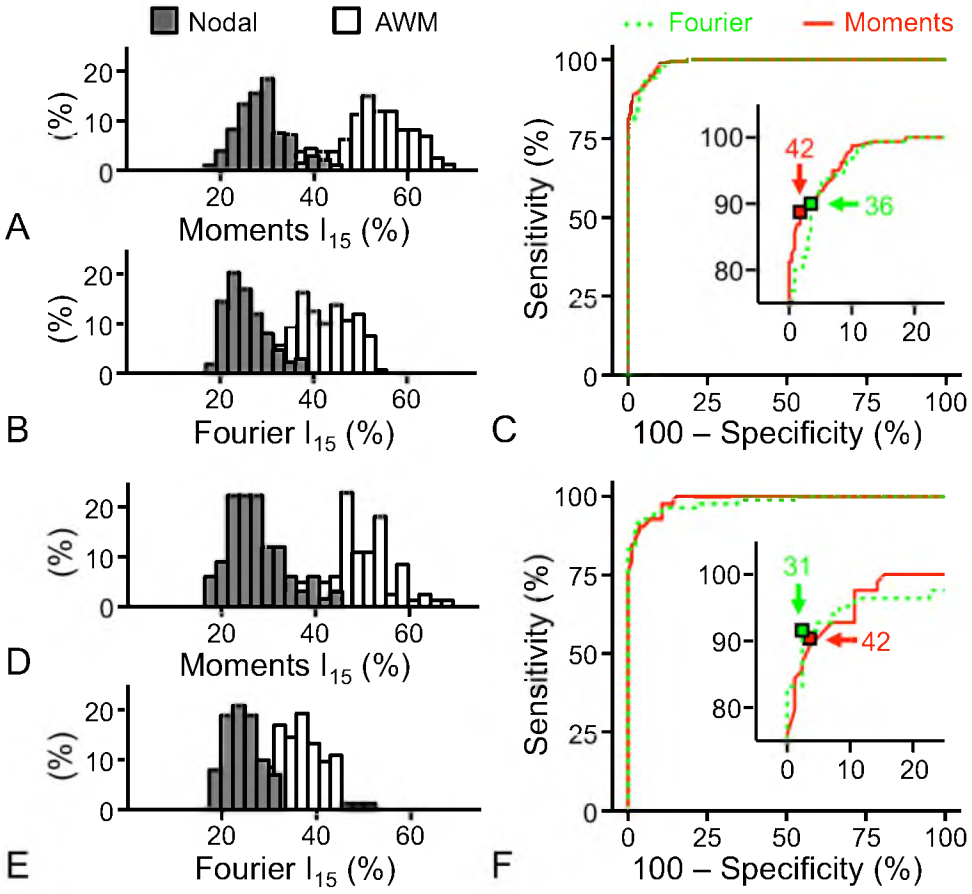

Figure 4.5 Receiver operating characteristic analysis of indexed image sets. Histograms and receiver operating characteristic curves of I_{15} for (A-C) CCM, (D-F) $FCM_{topical}$, and (G-I) $FCM_{carrier}$ images based on Fourier (green dotted line) and image moment (red solid line) texture analysis. A bimodal I_{15} distribution was observed with indexed nodal (filled histogram) and atrial working myocardium (AWM, unfilled histogram) images grouped around lower and higher maxima, respectively. Inset within ROC curves show a magnified view of the curve closest to the region of perfect classification (upper left corner). Optimal cut-off values from Fourier (green square) and image moment (red square) texture analysis of the (C) CCM, (F) $FCM_{topical}$, and (I) $FCM_{carrier}$ images are shown in the insets.

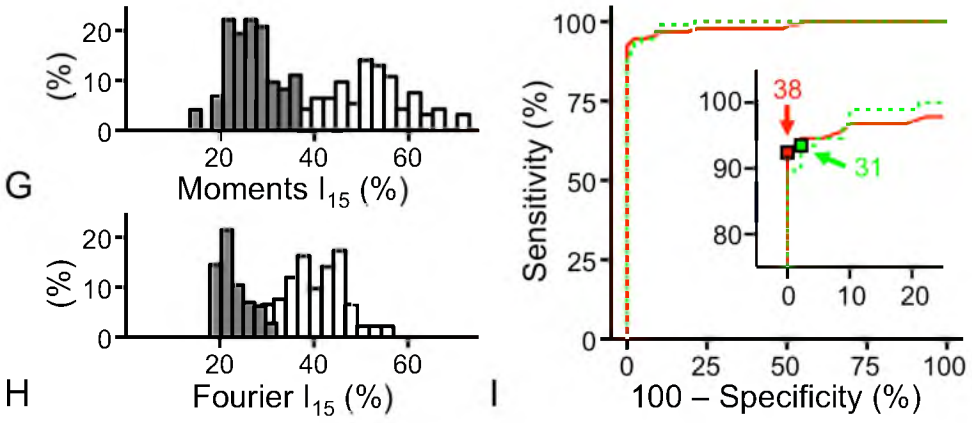

Figure 4.5 Continued

Table 4.1 Parameters for receiver operating characteristic analysis

Images	Animals / Images		Moments			Fourier		
	AWM	Nodal	Cutoff	Sensitivity %	Specificity %	Cutoff	Sensitivity %	Specificity %
CCM	6 / 160	7 / 230	42.3	88.8	98.3	35.7	90.0	96.5
$FCM_{topical}$	5 / 83	6 / 84	42.1	90.4	96.4	30.8	91.6	97.6
$FCM_{carrier}$	10 / 92	10 / 90	37.9	92.4	100.0	30.5	93.5	97.8

AWM, atrial working myocardium; CCM, conventional confocal microscopy; FCM, fiber-optics confocal microscopy;

Table 4.2 Summary of human and automated classification of confocal images

	Examiner (n = 8)		Fourier		Moments	
	Sensitivity	Specificity	Sensitivity	Specificity	Sensitivity	Specificity
Images	% ± SE		%	%	%	%
CCM	100.0 ± 0.0	87.5 ± 3.3	100.0	95.1	100.0	88.9
$FCM_{topical}$	99.2 ± 0.3	94.0 ± 2.4	98.8	91.4	98.8	91.4
$FCM_{carrier}$	99.2 ± 0.3	98.0 ± 0.7	97.5	95.1	100.0	92.6

CCM, conventional confocal microscopy; FCM, fiber-optics confocal microscopy; SE, standard error;

Table 4.3 Comprehensive summary of human and automated tissue classification

	CCM		$FCM_{topical}$		$FCM_{carrier}$	
	Sensitivity %	Specificity %	Sensitivity %	Specificity %	Sensitivity %	Specificity %
Examiner1	100.0	85.2	100.0	100.0	98.8	100.0
Examiner2	100.0	90.1	100.0	96.3	97.5	96.3
Examiner3	100.0	85.2	100.0	79.0	98.8	98.8
Examiner4	100.0	86.4	100.0	88.9	100.0	98.8
Examiner5	100.0	86.4	98.8	96.3	100.0	98.8
Examiner6	100.0	100.0	98.8	96.3	98.8	100.0
Examiner7	100.0	97.5	98.8	96.3	100.0	95.1
Examiner8	100.0	69.1	97.5	98.8	100.0	96.3
Fourier	100.0	95.1	98.8	91.4	97.5	95.1
Moments	100.0	88.9	98.8	91.4	100.0	92.6

CCM, conventional confocal microscopy; FCM, fiber-optics confocal microscopy;

CHAPTER 4

SUMMARY AND PERSPECTIVES

Surgically-induced conduction disturbances such as sinus node dysfunction and atrioventricular block remain a serious complication that can result following surgical repair of CHD. The incidence of these conduction disturbances and lifelong dependence on pacing therapy was described in Chapter 1. In Chapter 1, we also looked at surgical techniques used to repair CHD. It is not surprising that the techniques which scrupulously avoided the CCS presented the lowest incidence of postoperative conduction disturbances. The established method for avoiding the CCS is based on approximating its location using anatomical landmarks since the CCS resides below the epi/endocardial layer of the heart. However, this imprecise method is not acceptable for surgical repair of CHD in which the the course of the CCS is variable or unknown or when the repair necessitates placement of sutures or incision lines in close proximity to the CCS. A method for direct visualization of the CCS during pediatric heart surgery is needed.

In Chapter 2, we demonstrated feasibility of identifying nodal tissue in living heart using an approach based on extracellular fluorophores and FCM. We

suggested that this approach had the potential to be used to visualize the CCS and reduce the incidence of conduction disturbances during pediatric heart surgery. This study was the first of its kind to visualize and reconstruct at submicrometer resolution the tissue microstructure found within the CCS, specifically the specialized tissue of the SAN and AVN. In addition, we introduced methods based on image texture analysis that allowed for quantitative characterization of tissue microstructure. The results of this study suggested that visualization of the CCS during pediatric heart surgery was possible; however, the result of this study brought to light certain challenges in clinical translation of FCM for pediatric heart surgery. Some of these challenges included the reliance on systemic injections of fluorescent dyes in clinical applications of FCM as well as the sensitivity and specificity of the developed approach for cardiac tissue discrimination. These challenges were investigated in Chapters 3 and 4, respectively.

A major challenge in applying FCM for pediatric heart surgery was the reliance of this imaging approach on systemic delivery of fluorescent dyes. We needed to address concerns in regards to high dye consumption and adverse reactions using this dye delivery method, particularly in a pediatric population. In Chapter 3, we investigated local and systemic dye delivery approaches for FCM in the living heart. We found that a local dye delivery approach using a foam-agarose dye carrier comprised of porous foam and agarose hydrogel delivered fluorescent dye in sufficient concentration for FCM. In addition, this local dye delivery approach constituted an important alternative to established systemic

dye delivery methods. Differences in image quality, as measured by signal-to-noise ratio, in FCM images acquired following either local or systemic dye delivery approaches were not statistically significant. Furthermore, we found that the local dye delivery approach required significantly less dye than systemic delivery for FCM. The results of this study suggested that the local dye delivery approach is particularly suitable for FCM during pediatric heart surgery.

We had shown in Chapter 2 that FCM images of nodal tissue could be identified based on the microstructural arrangement of the extracellular space. However, there remained questions in regards to the performance of FCM for cardiac tissue discrimination, in particular for pediatric heart surgery. In Chapter 4, we investigated the sensitivity and specificity of human and automated systems in discriminating FCM images of AWM and nodal tissue. Using FCM with methods of local dye delivery previously described in Chapters 2 and 3, we acquired images from AWM and nodal tissue of living rat hearts. These images were subsequently indexed based on anatomical origin. A panel of human examiners were asked to classify a random set of these indexed images as AWM or nodal tissue. In addition, the image set was classified using automated classification systems based on texture and receiver operating characteristic analysis. Both human and automated classification systems achieved similarly high sensitivity and specificity. Furthermore, high sensitivity and specificity was attained in discriminating images of tissue acquired using FCM and the local dye delivery approach described in Chapter 3. The results of this study constitute an important step in clinical translation of FCM for pediatric heart surgery. We

suggest that intraoperative cardiac tissue discrimination with high sensitivity and specificity can be achieved using FCM and local dye delivery. Furthermore, real-time automated methods for discriminating AWM and nodal tissue could help guide surgeons in the placement of incisions and sutures during surgical repair of CHD.

This body of work encompasses the preclinical studies necessary to show the safety and effectiveness of FCM for cardiac tissue discrimination with specific application in pediatric heart surgery. The potential application of FCM in the cardiovascular field should not be taken lightly. For that matter, FCM is a perfect candidate for assimilation in any field in which cell and tissue physiology and pathophysiology would provide invaluable insights for diagnosis or therapy.